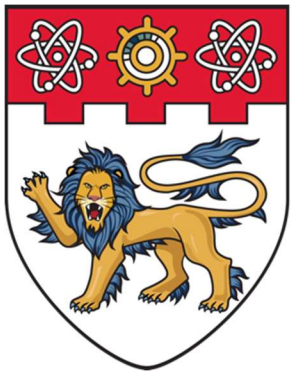

NANYANG TECHNOLOGICAL UNIVERSITY
SINGAPORE

BAND ENGINEERING IN RARE EARTH NICKELATES: PHYSICS AND APPLICATIONS

CHANG LEI

SCHOOL OF MATERIALS SCIENCE AND ENGINEERING

2018

BAND ENGINEERING IN RARE EARTH NICKELATES: PHYSICS AND APPLICATIONS

CHANG LEI

SCHOOL OF MATERIALS SCIENCE AND ENGINEERING

A thesis submitted to the Nanyang Technological University
in partial fulfilment of the requirement for the degree of
Doctor of Philosophy

2018

Statement of Originality

I hereby certify that the work embodied in this thesis is the result of original research and has not been submitted for a higher degree to any other University or Institution.

Input Date Here	Input Signature Here
Aug 21, 2018	Chang Lei
Date	Input Name Here

Supervisor Declaration Statement

I have reviewed the content and presentation style of this thesis and declare it is free of plagiarism and of sufficient grammatical clarity to be examined. To the best of my knowledge, the research and writing are those of the candidate except as acknowledged in the Author Attribution Statement. I confirm that the investigations were conducted in accord with the ethics policies and integrity standards of Nanyang Technological University and that the research data are presented honestly and without prejudice.

Input Date Here

Aug 21, 2018

Date

Input Supervisor Signature Here

Wang Junling

Input Supervisor Name Here

Authorship Attribution Statement

This thesis contains materials from papers published in the following peer-reviewed journals where I was the first author or co-first author.

Chapter 5 is published as L. Chang, L. Wang, L. You, Y. Zhou, L. Fang, S. W. Wang and J. L. Wang. Band gap tuning of nickelates for photovoltaic applications. *Journal of Physics D: Applied Physics* **49**, 44 (2016). DOI: 10.1088/0022-3727/49/44/44LT02.

The contributions of the co-authors are as follows:

- Prof. J. L. Wang and Prof. L. Fang provided the initial project direction and edited the manuscript drafts.
- I prepared the manuscript drafts. The manuscript was revised by Dr. L. Wang.
- I co-designed the study with Dr. L. Wang and performed all the laboratory work. I analyzed the data.
- Dr. L. You and Dr. Y. Zhou assisted in the structure measurement. Dr. S. W. Wang assisted in the electrical property measurement.

Chapter 6 is published as L. Wang, L. Chang, X. M. Yin, L. You, J. L. Zhao, H. Z. Guo, K. J. Jin, K. Ibrahim, J. Wang, A. Rusydi and J. L. Wang, Self-powered sensitive and stable UV-visible photodetector based on $GdNiO_3$/Nb-doped $SrTiO_3$ heterojunctions. *Applied Physics Letters* **110**(4), (2017). DOI: 10.1063/1.4974144.

The contributions of the co-authors are as follows:

- Prof. J. L. Wang suggested the research idea and edited the manuscript drafts.
- I drafted the initial manuscript and performed all the electrical property measurements together with Dr. L. Wang.
- Dr. X. M. Yin performed the ellipsometry test. The results were analyzed by Prof. A. Rusydi.

- Dr. J. L. Zhao, Dr. H. Z. Guo and Dr. J. Wang conducted X-ray absorption spectroscopy measurements. The corresponding data was analyzed by Prof. K. Ibrahim and Prof. K. J. Jin.

Input Date Here	Input Signature Here
Aug 21, 2018	Chang Lei
Date	Input Name Here

Abstract

Transition metal oxides have been the focus of solid state physics research for decades. The Coulomb repulsion energy, orbital bandwidth and Hund's exchange energy often become comparable in these materials, leading to strong interplay between lattice, electron orbitals and spin, which in turn produces unusual properties such as metal-insulator transition, giant magnetoresistance, and superconductivity etc. Rare earth nickelates with a chemical formula of $RNiO_3$, where R represents a rare earth element, is a family of transition metal oxides. Much attention has been paid to the metal-insulator transition in this system and the nature of the insulating phase.

Oxygen vacancies are intrinsic to $RNiO_3$. Acting as electron donors, they are expected to affect the valance states of Ni ions, thus changing the band structures and transport behaviors of $RNiO_3$, which forms the basis of this study.

Both post-deposition vacuum annealing and adjusting oxygen pressure during deposition are used to introduce oxygen vacancies into $RNiO_3$ thin films. This is followed by detailed structural and electrical characterizations. Resistance change of as large as $\sim 10^6$ has been observed after introducing oxygen vacancies, and insulating phases with tunable bandgaps are obtained. It is proposed that narrowing of the 3d bands opens a gap between Ni 3d and O 2p bands. The process is reversible and continuously tunable.

With their tunable bandgaps, it is expected that the oxygen vacancy engineered $RNiO_3$ thin films may find applications in various optoelectronic devices. As a demonstration, $RNiO_3$/Nb-$SrTiO_3$ heterojunctions are thus produced and their performances as photovoltaic cells are investigated. By varying the oxygen vacancy content, rare earth element and device structure, a power conversion efficiency of 1.1% has been achieved. The same heterostructures can also be used as self-powered ultra-sensitive photodetectors. Such photodetectors show high sensitivity toward a broad spectrum of light with very good long-term stability.

Last but not least, the fact that oxygen vacancies can be introduced into $RNiO_3$ thin films via post-deposition vacuum annealing implies relatively weak Ni-O bonds. It is thus possible to dynamically control the amount and distribution of oxygen vacancies in $RNiO_3$ thin films using an electric field. This is particularly interesting because oxygen vacancies affect the electronic phase of $RNiO_3$, so the transport property can be dynamically controlled. Indeed, large resistive switching is observed in various $RNiO_3$/Nb-$SrTiO_3$ heterojunctions. Detailed transmission electron microscopy analysis reveals that oxygen vacancy migration indeed occurs and modulates the interface energy barrier, leading to the observed phenomena. Further studies show excellent retention and fatigue performance of these devices and demonstrate their potential as non-volatile memories.

This work improves our understanding on $RNiO_3$ and opens new possibilities for their applications in various optoelectronic devices.

Lay Summary

In this study, thin films of rare earth nickelates, $RNiO_3$, are fabricated and their electrical and optical properties investigated. By adjusting the oxygen vacancies in the thin films, the electronic phase of $RNiO_3$ can be modulated, leading to the opening of a bandgap. This causes dramatic changes in their electrical conductivity and light absorbing property. A model is proposed to explain the changes observed. Various devices, including photovoltaic cells, photodetectors and non-volatile memories, based on the oxygen vacancy engineered $RNiO_3$ thin films are proposed and demonstrated. This work promotes the development of $RNiO_3$-based multifunctional optoelectronic devices.

Acknowledgements

Firstly, I would like to express my deep and sincere gratitude to my supervisor Prof. Junling Wang for his support for my Ph.D study. His patience, inspiration, and guidance benefit me a lot during the whole research for the last four years.

I deeply appreciate the kind guidance from my seniors, Dr. Lu You and Dr. Le Wang. Their immense knowledge on solid state physics and thin films technology provide much convenience for my research.

I want to thank all the other group members for their discussion on my research: Dr. Yang Zhou, Dr. Rui Guo, Dr. Peng Ren, Mr. Amr Ahmed Korany Abdelsamie, Dr. Shiwei Wang, Prof. Liang Fang and Prof. Guoliang Yuan.

I would like to thank all the technicians of laboratories and FACTS lab from my school.

I would like to thank my family and girlfriend for their support on my daily life.

I would like to show my appreciation to Singapore government and Ministry of Education, Singapore for their financial support for the last 4 years.

Table of Contents

Table Captions

Figure Captions

vacuum annealing temperature. R_H is the slope of the plot in (a) and follows the formula $R_H = (\rho_{(7T)} - \rho_{(0T)})/7T$, where T (tesla) is the unit of magnetic field.

Figure 4.7 (a) Ni 2p XPS spectra of as-grown and vacuum annealed 40 nm-thick $NdNiO_3$ films. The inset shows an enlargement for Ni 2p XPS of as-grown sample and that of sample vacuum annealed under 300℃, which indicates an increase in Ni^{2+} fraction after vacuum annealing process. Valence band maximum (VBM) (b) and work function (W_F) (c) determined from the secondary electron onset in UPS measurements. (d) Schematic phase diagram of $NdNiO_3$ film undergoing a room temperature metal-insulator transition due to oxygen vacancy. Schematic energy band diagrams for three different states are shown below the phase diagram. Here, Δ denotes the charge transfer energy, U is d-d Coulomb repulsion energy, E_F is the Fermi level and Eg is the bandgap.

Figure 4.8 Topography images of 45 nm $NdNiO_3$ thin films prepared under different oxygen pressure on (001)-oriented $SrTiO_3$ substrates. All samples show smooth surface with sub-nm level roughness.

Figure 4.9 HR-XRD theta-2theta scans of 45 nm $NdNiO_3$ films prepared under different $P(O_2)$. The zoom in pattern around $SrTiO_3$ (002) shows the (002) peak shift due to oxygen vacancies introduced.

Figure 4.10 (a) Temperature dependence of R_{sheet} of $NdNiO_3$ films deposited under different oxygen pressure (The R_{sheet} of $NdNiO_3$ films grown under 0.02 mTorr exceeds the range of the PPMS). (b) *c*-axis lattice constant and R_{sheet} of $NdNiO_3$ films as a function of $P(O_2)$ at 300 K. All the films are 45 nm thick.

Figure 5.1 (a) UV-Vis absorption spectra of 45 nm-thick $NdNiO_3$ films grown under different $P(O_2)$. (b) Tauc plots derived from optical absorption spectra. The inset shows the pictures of these $NdNiO_3$ films grown on double-polished transparent substrates.

Figure 5.2 (a) *J-V* curves of Au/$NdNiO_3$/Nb-$SrTiO_3$ heterojunctions measured in dark. The inset shows the schematic device structure. (b) Plots of $1/C^2$ versus voltage of these heterojunctions. The dashed lines are the linear fittings of the plots, whose intercept with x-axis indicates the values of V_{bi}. (c) *J-V* curves of the same heterojunctions measured under illumination. (d) $P(O_2)$ dependence of J_{SC}, V_{OC} and power conversion efficiency (PCE). PCE is defined as PCE = $V_{OC} \times J_{SC} \times FF/P_{in}$, where FF is the filling factor, P_{in} is the input power density of a Xeon lamp. (150 mW/cm^{-2})

Figure 5.3 (a) Thickness dependence of the photovoltaic performance of Au/$NdNiO_3$/Nb-$SrTiO_3$ heterojunctions. $P(O_2)$ is fixed at 0.5 mTorr. (b) Schematic energy diagram across the interface in the $NdNiO_3$/Nb-$SrTiO_3$ heterojunctions.

Figure 5.4 (a) Schematic device structure of the Au/$RNiO_3$/Nb-$SrTiO_3$ heterojunctions. (b) Plots of $1/C^2$ versus voltage of the $RNiO_3$/Nb-$SrTiO_3$ heterojunctions, where the 30 nm $RNiO_3$ layer is prepared under 300 mTorr $P(O_2)$. (c)-(f) *J-V* curves of $NdNiO_3$, $SmNiO_3$, $GdNiO_3$ and $LuNiO_3$ heterojunctions measured with light on and off. NNO, SNO, GNO and LNO denote $NdNiO_3$, $SmNiO_3$, $GdNiO_3$ and $LuNiO_3$.

Figure 5.5 Oxygen pressure dependence of (a) V_{OC} and (b) J_{SC} for different $RNiO_3$/Nb-$SrTiO_3$ heterojunctions. (c) The calculated PCEs of different $RNiO_3$/Nb-$SrTiO_3$ heterojunctions with $RNiO_3$ of the same thickness (30 nm) prepared under different pressures.

Figure 5.6 (a) *J-V* characteristics of $SmNiO_3$ (30 nm)/Nb-$SrTiO_3$ and $SmNiO_3$/$SrTiO_3$ (5 nm)/Nb-$SrTiO_3$ heterojunctions with $RNiO_3$ layer prepared under 20 mTorr when light is off. (b) *J-V* curves of $SmNiO_3$ (30 nm)/Nb-$SrTiO_3$ and $SmNiO_3$/$SrTiO_3$ (5 nm)/Nb-$SrTiO_3$ heterojunctions measured in dark and under illumination. SNO, STO, NSTO denote $SmNiO_3$, $SrTiO_3$ and Nb-$SrTiO_3$.

Figure 6.1 Room-temperature HR-XRD patterns of $GdNiO_3$ thin films grown on (001) oriented $SrTiO_3$ substrates. 'S' denotes the diffraction peaks of the substrates. 'F' denotes the diffraction peaks of $GdNiO_3$ films. D1 to D5 denote $GdNiO_3$ thin films deposited under 300, 100, 20, 2, and 0.2 mTorr, respectively. The (002) diffraction peak of the $GdNiO_3$ film shifts towards smaller diffraction angles with decreasing $P(O_2)$.

Figure 6.2 (a) Absorption coefficient of $GdNiO_3$ thin films extracted from spectroscopic ellipsometry measurements. D1 to D5 denote $GdNiO_3$ thin films deposited under 300, 100, 20, 2, and 0.2 mTorr respectively. (b) Tauc plots calculated from (a) and linear fittings of the absorption spectra. The interceptions of linear fittings with the x-axis reveal the optical bandgaps. As the $P(O_2)$ decreases, bandgap increases.

Figure 6.3 Ni L_{32} edge (a) and O *K* edge (b) spectra of three representative samples extracted from XAS measurements. To clearly show the peak splitting and the gradual intensity change, only the results of samples prepared under 100 (D2), 20 (D3), 0.2 (D5) mTorr are plotted. A and B in the L_3 portion of the spectra label the peak around 853 eV and a broad satellite peak near 854 eV, respectively. The intensity ratio between L_3 and L_2 peaks increases when $P(O_2)$ decreases. The red arrow in (b) labels the pre-peak near 529 eV of O *K* edge spectra, which measures covalency between Ni and O. The intensity of the pre-peak decreases when $P(O_2)$ decreases, indicating reduced hybridization.

Figure 6.4 Energy levels and work functions across the Au/$GdNiO_3$/Nb-$SrTiO_3$ heterojunctions. The dashed lines denote the E_F. The top of valence band (E_V) is extracted from UPS results. The bottom of conduction band (E_C) is calculated by using the bandgap values and E_V.

Figure 6.5 (a) Schematic diagram of the PDs based on Au/$GdNiO_3$/Nb-$SrTiO_3$ heterojunctions. (b) Responses of the Au/$GdNiO_3$/Nb-$SrTiO_3$ PDs with light on and off. The illumination is supplied by a 365 nm-UV light with power density of 0.6 mW/cm^2. (c) photo-dark ratio and responsivity versus $P(O_2)$ extracted from (b). D1 to D5 denote

$GdNiO_3$ thin films deposited under 300, 100, 20, 2, and 0.2 mTorr respectively. All devices have Au top electrodes with area of 400×400 μm^2.

Figure 6.6 (a) Photo-response of $GdNiO_3$/Nb-$SrTiO_3$ heterojunctions with $GdNiO_3$ layer prepared under 20 mTorr. The light power density is fixed at 10 mW/cm^2 except for 365 nm UV light because of the equipment limitation (light intensity of 0.6 mW/cm^2). (b) The responsivity as a function of wavelength and the corresponding Tauc plots. The Tauc plots are extracted from the absorption spectra as presented in Figure 6.2. Here, R denotes responsivity.

Figure 6.7 (a) Photo-response of the Au/$GdNiO_3$(20 mTorr)/Nb-$SrTiO_3$ heterojunction as a function of time. The illumination is supplied by a 365 nm-UV light source. The 'I' represent I_{ON}. (b) I_{PH} and responsivity calculated from (a), where $I_{PH} = I_{ON} - I_{OFF}$. (c) Device stability in air at room temperature. The illumination is supplied by a 365 nm-UV light source at 50 μW/cm^2. (d) Device reproducibility under illumination of 365 nm-UV light at 50 μW/cm^2.

Figure 7.1 (a) AFM images of $GdNiO_3$ films prepared under 100 (D1), 20 (D2), 2 (D3), 0.2 (D4) mTorr oxygen pressure $P(O_2)$. (b) Room-temperature HR-XRD patterns around the (002) peaks. S and F represent peaks form substrates and $GdNiO_3$ films, respectively. (c) *c*-axis lattice constant as a function of $P(O_2)$ calculated from the HR-XRD patterns.

Figure 7.2 (a) *I-V* curves of Pt/$RNiO_3$/Nb-$SrTiO_3$ heterostructures (D1-D4) plotted on log scales. (b) Resistance of the corresponding samples (D1-D4) as a function of the applied voltage pulse. D1 to D4 denote samples prepared under 100, 20, 2 and 0.2 mTorr $P(O_2)$ respectively.

Figure 7.3 (a) Resistance (*R*) and capacitance changes of sample Pt/$GdNiO_3$(0.2 mTorr)/Nb-$SrTiO_3$ (D4, 0.2 mTorr) under voltage sweeping. The *C-V* curve is extracted from impedance measurements with a 10 mV, 25 kHz AC signal imposed on a continuous

DC bias. (b) The distribution of ON/OFF ratio among randomly selected devices. (c) Pulse width dependence of the resistive switching during the 'set' process. (d) Pulse width dependence of the resistive switching during the 'reset' process. Voltage pulses are 5 V. (e) Retention characteristic of the HRS and LRS recorded at -0.2 V after a forward and reverse bias sweep, respectively. (f) Fatigue performance of the device.

Figure 7.4 (a) Linear scale *I-V* curves of Pt/$GdNiO_3$(0.2 mTorr)/Nb-$SrTiO_3$ (D4) with voltage sweeping between -5 V to +5 V. (b) Fittings of the nonlinear *I-V* curves of the $GdNiO_3$/Nb-$SrTiO_3$ heterojunctions using difference models. (c) Migration of oxygen vacancies in $GdNiO_3$/Nb-$SrTiO_3$ heterojunctions under electric field. V_O`` denotes oxygen vacancy. (d) Time-dependence of the small-signal current of LRS. The blue dashed line is the power law fitting.

Figure 7.5 HAADF TEM images of Pt/$GdNiO_3$(0.2 mTorr)/Nb-$SrTiO_3$ (D4) at (a) LRS and (b) HRS. (c, d) O *K* edge and Ni *L* edge EELS spectra along the scanning paths labeled with color arrows in (a) and (b). (e) Comparison between the O *K* edge and Ni *L* edge EELS spectra at HRS and LRS. The pre-peak of O *K* edge is indicated by a blue arrow. (f) Ni L_3/L_2 area ratio for HRS and LRS after the Ni *L* edge normalization. The error bars are based on the multiple peak area calculations and the line is to assist visualization. The color arrow in the figure indicates the scanning direction.

Figure 7.6 (a) T_{MI} as a function of the Ni-O-Ni bond angle. The inset shows the schematic diagram of change bond angles. (b) *I–V* curves of the Pt/$RNiO_3$/Nb-$SrTiO_3$ devices. All $RNiO_3$ films were prepared under 100 mTorr. (c) Dependence of the ON/OFF ratios on $P(O_2)$ and rare-earth elements for Pt/$RNiO_3$/Nb-$SrTiO_3$ heterostructures.

Figure 8.1 Oxygen vacancy migration in $RNiO_3$/Nb-$SrTiO_3$ heterojunctions.

Figure 8.2 Schematic illustration of the operation mechanism of $SmNiO_3$-based solid oxide fuel cells. Reprinted with permission.[16] Copyright 2017, Nature Publishing Group.

Abbreviations

AC	Alternating Current
AFM	Atomic Force microscopy
DC	Direct Current
EELS	Electron Energy Loss Spectroscopy
E_V	top of valence band
FF	Filling Factor
GNO	Gadolinium Nickelate Oxide
HAADF	High Angle Angular Dark-Field
HR-XRD	High Resolution X-ray Diffraction
HRS	High Resistance State
HCS	High Capacitance State
J_{SC}	Short-Circuit Current Density
LCS	Low Capacitance State
LED	Light Emission Diode
LNO	Lutetium Nickelate Oxide
LRS	Low Resistant State
MIT	Metal-Insulator Transition
NNO	Neodymium Nickelate Oxide
PCE	Power Conversion Efficiency
PD	Photodetector
$P(O_2)$	Oxygen Pressure
PLD	Pulsed Laser Deposition
PPMS	Physical Property Measurement System
PV	Photovoltaic
RNO	Rare Earth Nickelates
SCLC	Space Charge Limited Conduction
SNO	Samarium Nickelate Oxide
STO	Strontium Titanite Oxide
TEM	Transmission Electron Microscopy

T_{MI}	Temperature of Metal-Insulator Transition
UPS	Ultraviolet Photoelectron Spectroscopy
UV-Vis	Ultraviolet-Visible
V_{OC}	Open-Circuit Voltage
VBM	Valence Band Maximum
W_F	Work Function
XAS	X-ray Absorption Microscopy
XPS	X-ray Photoelectron Spectroscopy
XRD	X-ray Diffraction

Chapter 1

Introduction

This chapter covers the hypothesis and related objectives of this work. Oxygen vacancies are introduced into $RNiO_3$ films by means of post-deposition vacuum annealing or adjusting oxygen pressure during film growth. The oxygen vacancy goes into or out of the $RNiO_3$ films, which is reversible and tunable. Thus, the band structure and electrical properties of $RNiO_3$ should also be reversibly and continuously tuned. Depending on the bandgaps, such films may find applications in various devices such as photovoltaic cells, photodetectors and resistive switching memories. This chapter provides an overview of the whole thesis. It summarizes the content and discoveries in each chapter and emphasizes the originality of the content in this thesis.

1.1 Hypothesis

Transition metal oxides have been studied extensively due to their exotic physical properties. The strong interplay between lattice, orbital and spin in such compounds leads to comparable magnitudes of the Coulomb repulsion, orbital bandwidth and Hund's exchange energy.[1] Consequently, their physical properties are very sensitive to perturbations in temperature, strain, dimensionality and so on. Rare earth nickelates ($RNiO_3$, where R represents rare-earth elements) is one family of transition metal oxides. Previous studies have demonstrated tuning of their band structures by means of chemical doping, electrical field effect, or strain engineering. For example, hole-doping is achieved by chemical substitution of Ca^{2+} or Sr^{2+} for Nd^{3+} in $NdNiO_3$, which suppresses the temperature-driven metal-insulator transition.[2] Electric field can be used to control the carrier density in ultrathin nickelate thin films reversibly.[3]

Oxygen vacancy is well known to play an import role in perovskite oxides.[4-10] Acting as double electron donors, they can affect the valance states of transitional metals in transition metal oxides. The question of how oxygen vacancy affects the hybridization between O and Ni orbitals, the energy band structures and physical properties of nickelates is still not well understood. In this work, we aim to clarify such effects by introducing oxygen vacancies into $RNiO_3$ films by means of post-deposition vacuum annealing or adjusting oxygen pressure during film growth. The oxygen vacancy goes into or out of the $RNiO_3$ films, which is expected to be reversible and tunable. Thus, the band structure and electrical properties of $RNiO_3$ should also be reversibly and continuously tuned. Depending on the bandgaps, such films may find applications in various devices such as photovoltaic cells, photodetectors and resistive switching memories.

1.2 Objectives and Scope

Based on the hypothesis, the objectives and scope are listed as following.

Firstly, epitaxial thin films of $RNiO_3$ will be deposited by pulsed laser deposition (PLD) on (001) oriented $SrTiO_3$ substrates under oxygen pressure of 40 Pa. Some of these samples will undergo the vacuum annealing process to introduce oxygen vacancies. The crystal structure and surface roughness of these samples will be checked by high resolution X-ray diffraction (HR-XRD) and atomic force microscopy (AFM) to make sure that vacuum annealing will not damage the quality of as-grown samples. The electrical transport properties will be tested using physical property measurement system (PPMS) to investigate the difference of in their metal-insulator transitions (MITs), if any. X-ray photoelectron spectroscopy (XPS) and ultraviolet photoelectron spectroscopy (UPS) will be measured to extract the changes in energy band structures. A model will be established based on the experimental results to explain the effects of oxygen vacancy on the electronic structures of $RNiO_3$.

Secondly, epitaxial thin films of $RNiO_3$ will be deposited by PLD under different oxygen pressures. Oxygen vacancies will be introduced into thin films during deposition. Compared with the vacuum annealing process, oxygen pressure controlling during thin film growth should be more direct and effective to adjust the oxygen vacancies in thin films. The microstructures and surface information will again be tested using HR-XRD and AFM, as well as the electric transport properties by using PPMS. Ultraviolet-Visual (UV-Vis) spectroscopy will be used to get the bandgap values. By combining with conductive n-type substrates, the heterojunctions should have diode characteristics, which will be verified by *I-V* testing. Because the modulation of electronic band structures is expected to be continuous, the bandgap could be adjusted to suitable values to meet the requirements for photovoltaics. The photovoltaic performance will thus be systematically optimized by varying oxygen pressure during deposition, film thickness and the rare-earth elements. The relationship between photovoltaic performance and the oxygen pressure as well as the band structure of rare-earth nickelates will be established.

Thirdly, because oxygen vacancy can tune the bandgap, we will explore photodetectors based on $RNiO_3$, which may be suitable to detect a wide range of light wavelength. The performance of the photodetectors will be investigated by using different light sources at

different power density.

Finally, since the transport behavior of $RNiO_3$ is greatly related to their band structures and the MIT is likely affected by oxygen vacancies, $RNiO_3$/Nb-$SrTiO_3$ heterojunctions will be tested as non-volatile memories. Due to the relatively weak bond between O and Ni in $RNiO_3$, it is expected that an external electric field can drive the oxygen vacancies to migrate across the interface of $RNiO_3$/Nb-$SrTiO_3$. Such migration may modulate the electronic phase of $RNiO_3$ and the interface band bending, thus tuning the transport behavior of the junction. A resistive switching behavior is expected to happen, which could be used for non-volatile memory. Detailed mechanisms of the resistive switching will be investigated. Transmission electron microscopy (TEM) will be used to probe the oxygen vacancies and provide evidence for the hypothesis.

1.3 Dissertation Overview

This thesis is about the effects of oxygen vacancies on the energy band structures and transport behaviors of epitaxial $RNiO_3$ thin films. The electronic phases of $RNiO_3$ thin films are systematically tuned to suit different applications. The physics of the band structure engineering is discussed, and several possible applications based on oxygen vacancy engineered $RNiO_3$ are investigated.

Chapter 1 provides the rationale for the research topic and the corresponding objectives.

Chapter 2 introduces the basic properties of $RNiO_3$, including the crystal structure, electrical properties and previous studies. Also, difference models for metal-insulator transitions are discussed.

Chapter 3 introduces the fabrication and characterization techniques used in this thesis.

Chapter 4 covers the band engineering of $RNiO_3$ thin films by vacuum annealing, which introduces oxygen vacancies into $RNiO_3$ thin films, resulting in the bandgap opening. Various characterizations are performed to understand the transport behaviors and a

model is proposed to explain the effect of oxygen vacancy on the energy band structure.

Chapter 5 discusses the photovoltaic devices based on $RNiO_3$/Nb-$SrTiO_3$ heterojunctions. Changing the oxygen pressure during thin films deposition directly affect the oxygen vacancies in the films, and a suitable bandgap can be achieved for solar energy harvesting. The photovoltaic performance of the device is optimized by adjusting oxygen pressure during deposition, film thickness and changing the rare-earth element.

Chapter 6 discusses the design and performance of photodetectors based on $RNiO_3$/Nb-$SrTiO_3$ heterojunctions. No external bias is needed for such devices to work, and they could be applied for a wide range of wavelength.

Chapter 7 investigates the giant resistive switching behavior of $RNiO_3$/Nb-$SrTiO_3$ heterojunctions. The correlation between oxygen vacancy migration, interface band diagram tuning and resistive switching behavior is established. Various performance indicators of the device as a non-volatile memory are investigated.

Chapter 8 summarizes the findings of this project and propose possible future works based on the studies that have been done.

1.4 Findings and Outcomes/Originality

This study leads to the following discoveries:

1. It is confirmed that both post-deposition vacuum annealing and deposition under low oxygen partial pressure can introduce oxygen vacancies into $RNiO_3$ films. Oxygen vacancies can effectively tune the electronic structures of the $RNiO_3$ films, even stabilizing an insulating phase at room temperature. A model is proposed to explain the effect of oxygen vacancies on this family of materials.

2. Since the amount of oxygen vacancies in $RNiO_3$ can be tuned continuously and reversibly, leading to continuous and reversible modulation of their electronic structures,

it is thus expected that one can engineer the energy bands of $RNiO_3$ films for various applications specifically. Following this concept, I have designed and tested prototype devices for solar energy harvesting, photo-detection and non-volatile memory. The performances of these devices are investigated and working principles clarified.

This work improves our understanding on the unique properties of $RNiO_3$ and opens new possibilities for their practical applications in optoelectronics.

References

[1] J. M. Rondinelli and N. A. Spaldin. *Adv. Mater.* **2011**, 23, 3363-3381.

[2] J. García-Muñoz, M. Suaaidi, M. Martínez-Lope, and J. Alonso. *Phys. Rev. B* **1995**, 52, 13563.

[3] R. Scherwitzl, P. Zubko, I. G. Lezama, S. Ono, A. F. Morpurgo, G. Catalan, and J. M. Triscone. *Adv. Mater.* **2010**, 22, 5517-5520.

[4] H. Y. Hwang. *Nat. Mater.* **2005**, 4, 803.

[5] Y.-M. Kim, J. He, M. D. Biegalski, H. Ambaye, V. Lauter, H. M. Christen, S. T. Pantelides, S. J. Pennycook, S. V. Kalinin, and A. Y. Borisevich. *Nat. Mater.* **2012**, 11, 888.

[6] J. Jeong, N. Aetukuri, T. Graf, T. D. Schladt, M. G. Samant, and S. S. Parkin. *Science* **2013**, 339, 1402-1405.

[7] B. Wang, L. You, P. Ren, X. Yin, Y. Peng, B. Xia, L. Wang, X. Yu, S. M. Poh, and P. Yang. *Nat. Commun.* **2013**, 4, 2778.

[8] Z. T. Xu, K. J. Jin, L. Gu, Y. l. Jin, C. Ge, C. Wang, H. Z. Guo, H. B. Lu, R. Q. Zhao, and G. Z. Yang. *Small* **2012**, 8, 1279-1284.

[9] W. Li, R. Zhao, L. Wang, R. Tang, Y. Zhu, J. H. Lee, H. Cao, T. Cai, H. Guo, and C. Wang. *Sci. Rep.* **2013**, 3, 2618.

[10] R. Zhao, K. Jin, Z. Xu, H. Guo, L. Wang, C. Ge, H. Lu, and G. Yang. *Appl. Phys. Lett.* **2013**, 102, 122402.

Chapter 2

Literature Review

This chapter covers the basic properties of $RNiO_3$ and previous studies. The crystal structures and electrical properties of $RNiO_3$ are introduced. Different models to explain the origin of metal-insulator transition in transition metal oxides are introduced and compared. Tuning the metal-insulator transitions in $RNiO_3$ by various strategies are discussed. Based on previous studies, a few questions are proposed. The contributions of the author of this thesis are summarized.

2.1 Overview

2.1.1 Rare earth nickelates

Rare earth nickelates with a chemical formula of $RNiO_3$, where R represents rare-earth elements, is a family of transition metal oxides. The first synthesis of $RNiO_3$ was conducted by Demazeau et al.[1] in 1971. However, the group of materials did not gain much attention at the very beginning and few publications can be found at that time. In the late 1970s, studies on $LaNiO_3$[2] and $LaNi_{1-x}Mn_xO$, $LaNi_{1-x}Co_xO$[3, 4] started to appear but still no significant discoveries were reported. In the following 20 years, $RNiO_3$ were totally abandoned by researchers. This is likely because synthesis of $RNiO_3$ requires extreme conditions. Ni^{2+} oxides are usually obtained under oxygen environment (61 bar) and high temperatures (800-1000 □) but these conditions are not enough to form Ni^{3+}, which is necessary for the synthesis of $RNiO_3$. In the 1990s, high temperature superconductivity[5] and giant magnetoresistive effect[6] were reported in other perovskite-based oxides. Inspired by these discoveries, much effort was devoted to find novel materials with such exotic properties. Eventually, breakthroughs were achieved in cuprates and manganites firstly, which motivated more researchers to turn their attention towards nickelates because cuprates, manganites and nickelates were all rare oxides showing metallic behavior. Bulk $LaNiO_3$ is the first reported nickelates and also the only bulk $RNiO_3$ showing metallic phase within the whole temperature range. Other bulk $RNiO_3$ all undergo metal-insulator transition (MIT) at a certain temperature (T_{MI}).[7] Note that this statement is only valid for bulk $RNiO_3$, when it comes to thin films, recent studies have shown that $LaNiO_3$ thin films also undergoes MIT.[8]

Bulk $RNiO_3$ crystals are mostly orthorhombic perovskites (except for bulk $LaNiO_3$, which has a rhombohedral structure). The structure is shown in Figure 2.1a. Each rare-earth atom is surrounded by eight NiO_6 octahedrons. The NiO_6 octahedrons are distorted and tilted due to the small size of rare earth atoms.[9] However, if the rare-earth atom is large enough, such as La, the crystal system will change from orthorhombic to rhombohedral.

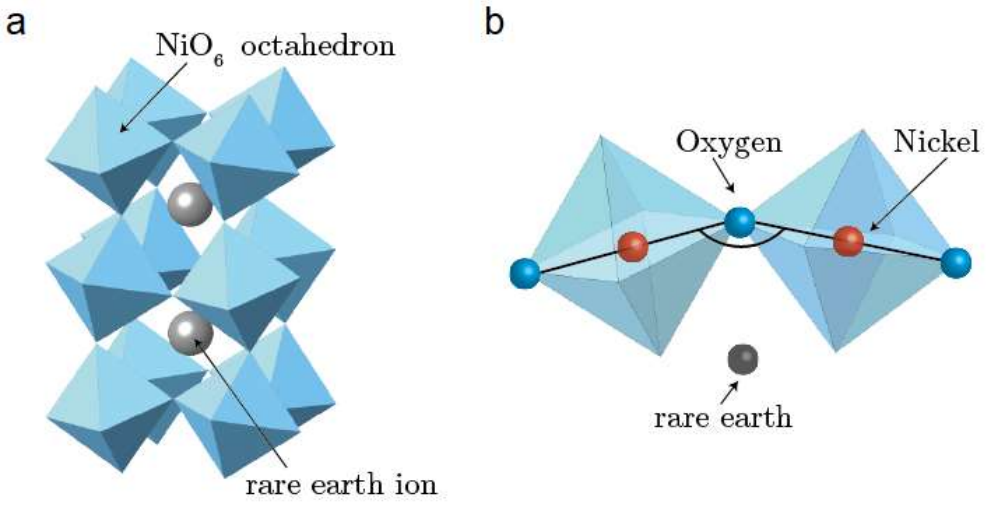

Figure 2.1 Schematic drawings of (a) crystal structure of $RNiO_3$, and (b) Ni-O-Ni bond. Reprinted with permission.[9] Copyright 2012, University of Fribourg.

Crystal tolerance factor (t) is often used to probe the degree of deviation from idea cubic perovskite structure. For nickelates, it is defined by the following equation:

$$t = \frac{d_{R-O}}{\sqrt{2}d_{Ni-O}}$$

where $d_{R\text{-}O}$ and $d_{Ni\text{-}O}$ represent the R-O and Ni-O bond length, respectively. For $RNiO_3$, t decreases from ~0.986 for $LaNiO_3$ to ~0.935 for $LuNiO_3$[10] as the size of rare-earth ion decreases. Figure 2.1b shows that the Ni-O-Ni bond angle is also affected by the size of rare earth elements. Previous work shows that when the size of rare earth atoms increases from Ho to Sm, Pr, and La, the Ni-O-Ni bond angle increases from 151.7 º to 152.6 º, 158.7 º, and 165.2 º.[11]

2.1.2 Ni 3d orbitals in perovskite structure

For $RNiO_3$, the rich electronic phase diagram derives mainly from the Ni 3d orbitals. Figure 2.2 shows the five distinct wave functions formed by 3d orbitals. In the perovskite structure of $RNiO_3$, the six oxygen anions surrounding the Ni cation create an octahedral crystal field. When the field interacts with d orbitals, two cases will happen. For $d_{x2\text{-}y2}$

and d_{z2}, because they point to the oxygen sites, the wave functions will be increased in energy. (e_g) While for the other three, they point away from the oxygen sites and have lower energies. So, there is an energy splitting between e_g and t_{2g} orbitals, as shown in Figure 2.2b.

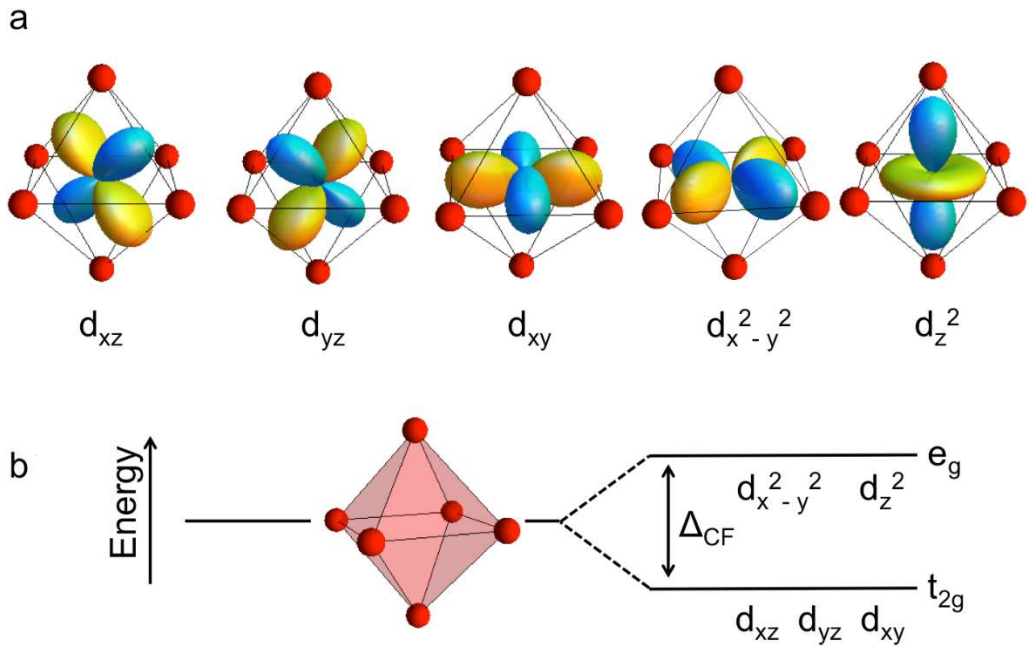

Figure 2.2 (a) Schematic illustration of the 3d wave functions, with respect to the ligand oxygen positions. (b) Octahedral crystal field splitting of the 3d orbitals. Reprinted with permission.[12] Copyright 2018, IOP publishing, Ltd.

2.1.3 Metal-insulator transition in transition metal oxides

Metal-insulator transition (MIT), as the name indicates, describes the phase evolution from metallic behavior to insulating behavior. It is characteristic of many transition metal oxides, although they have partially filled d shell.[13] This is contradictory to the conventional theory that partially filled shells result in metallic behavior. In this case, MIT is usually due to the strong electronic interactions associated with the 3d wave functions, such as the Coulomb repulsion and Hund's coupling. Detailed mechanisms of MIT in transition metal oxides is still an interesting topic of research.

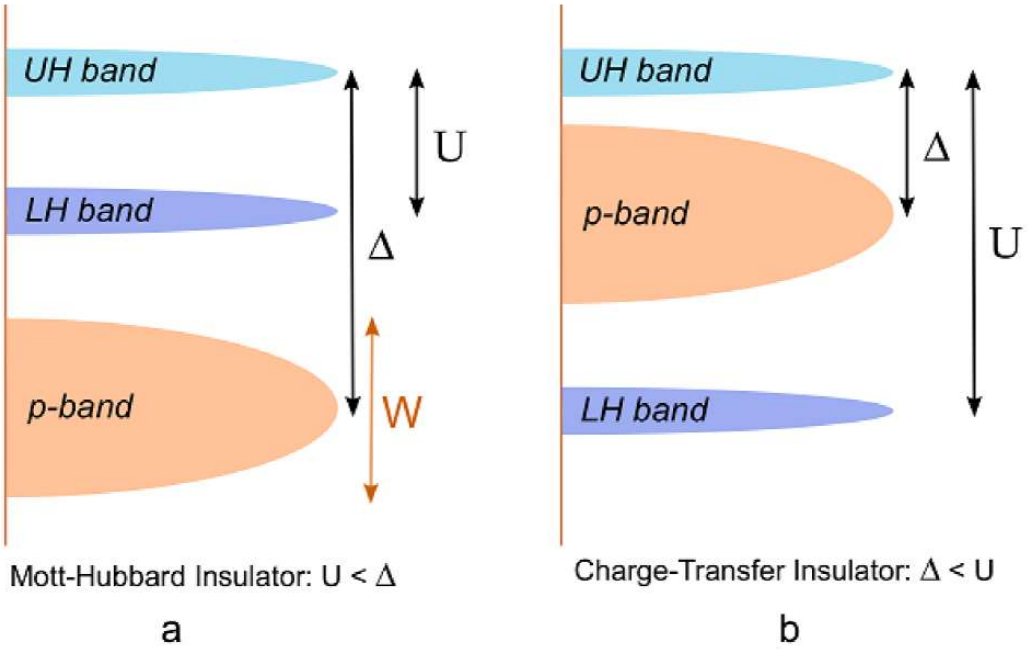

Figure 2.3 Schematic band structures of (a) a Mott–Hubbard insulator and (b) a charge-transfer insulator. Reprinted with permission.[12] Copyright 2018, IOP publishing, Ltd.

The MIT in transition metal oxides was originally explained by Mott and Hubbard in the so-called Hubbard model.[14, 15] In this model, when electrons are travelling in a lattice, a single energy level is considered at each site, and they form a single electronic band. Hopping of electrons between neighboring sites will result in a doubly occupied site, which causes a finite energy increase due to the charge repulsion between the electrons. This is defined as the Coulomb repulsion energy (U). If U is comparable to the kinetic energy, a transition to insulating state can occur even with a partially filled band because U prevents the hopping of electrons. Due to the existing of U, the original single band splits into two bands: the lower Hubbard (LH) and upper Hubbard (UH) bands. And a bandgap is opened between LH and UH, as shown in Figure 2.3a.

Note that in this case, the O p-band is assumed to be far away from the d band. The Hubbard model can be extended to describe complex systems by adding the contributions from other electronic interactions and multi-orbital occupancy. It successfully describes the insulating phases of several oxides such as titanates and vanadates, and such

compounds are classified as Mott-Hubbard insulators. Since the insulating phase is stabilized by the Coulomb repulsion (*U*), the electron transfer can be described as

$$d_i^n + d_j^n \rightarrow d_i^{n+1} + d_j^{n-1},$$

where i and j represent different sites and n represents the number of electrons.

However, many transition metal oxides, such as nickelates or cuperates, display insulating behaviors that cannot be fully described by the Hubbard model. This is because the O 2p band in these compounds is very close to transition metal d band, leading to strong hybridization between them. The p band may locate between UH and LH band, in which case, the lowest energy that electrons need to be excited is the gap between the p band and UH band, as shown in Figure 2.3b. An electron excited from p band to UH band will leave one ligand hole L in the oxygen band n, as shown in the following equation:

$$d^n \rightarrow d^{n+1}L.$$

The energy required for this excitation is the so-called charge transfer gap (*Δ*), which is the energy difference between the centers of oxygen p band and the transition metal UH band. Compounds that fit this model are classified as charge-transfer insulators.

To summarize, the electronic structure of a transition metal oxide can be described by *U*, *Δ* and the bandwidth (*W*), as shown in Figure 2.3. For Mott-Hubbard insulators, *Δ* is larger than *U*, so the gap is determined by *U*. For charge-transfer insulators, *U* is larger than *Δ*, so the gap is determined by *Δ*. This is the ZSA model introduced by Zaanen, Sawatzky and Allen.[16] It successfully describes the electrical behavior of many transition oxide compounds based on the ratio of *U* and *Δ*. In the case that *U* and *Δ* are both small, metallic behavior is expected.

However, there are special cases that were not included in the original ZSA model. It has been shown that *Δ* decreases as the valence number of the transition metal ion increases.[17] Transition metal oxides compounds that contain Cu^{3+}, Ni^{3+} and Fe^{4+} are thus expected to have very low *Δ* and show metallic behavior by ZSA model. However, bulk $NaCuO_2$, $LiNiO_2$, $CaFeO_3$ and $RNiO_3$ except $LaNiO_3$, are insulators at low temperatures.[18] Detailed investigations indicated that that *Δ* of these compounds is

close to or less than zero. For them, the lowest electron excitation is described by the following equation:

$$(d^{n+1}L)_i + (d^{n+1}L)_j \rightarrow (d^{n+1}L^2)_i + (d^{n+1})_j \quad ,$$

where L represents one ligand hole. The electron will be transferred between p bands as reflected from the above equation. Consequently, the ZSA model can be extended to include the negative Δ insulators, identified by a very small or negative Δ value.

The MITs of bulk $RNiO_3$ are summarized in Figure 2.4. The phase diagram is plotted as functions of temperature and tolerance factor (t). All bulk $RNiO_3$ except $LaNiO_3$ undergo a sharp MIT as a function of temperature. With decreasing size of rare-earth element, the T_{MI} increases. The size of rare-earth element is directly related to t, as discussed in the previous section. The decrease of t reduces the Ni-O-Ni bond angle, resulting in a weaker interaction between Ni 3d and O 2p orbitals.

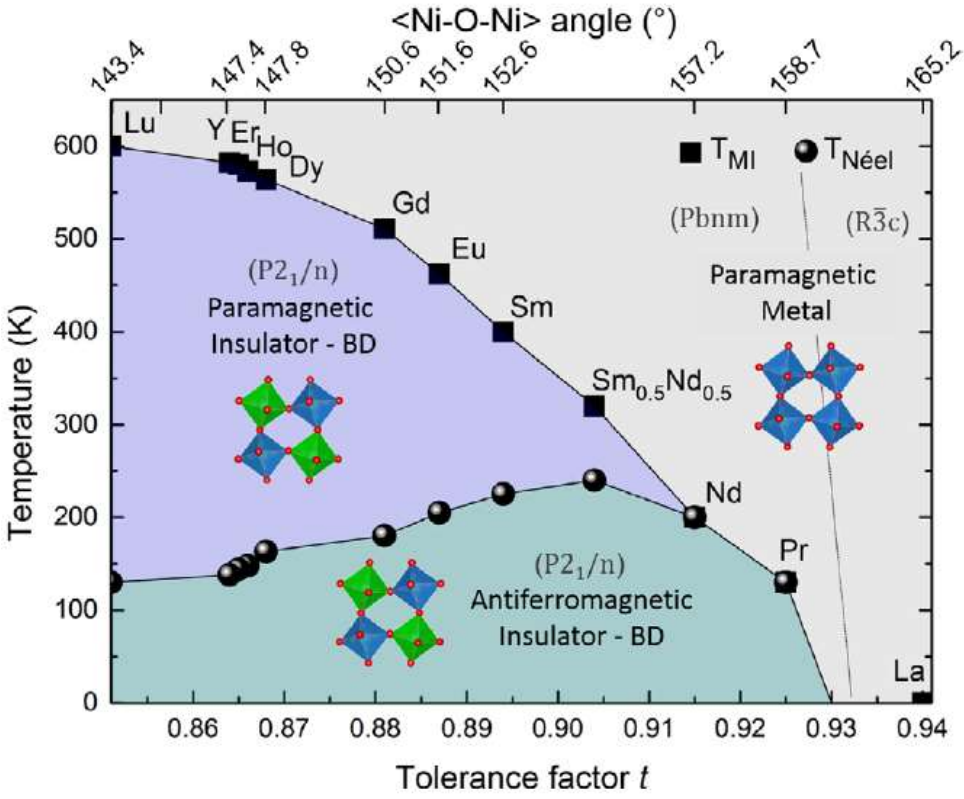

Figure 2.4 Phase diagram of $RNiO_3$ as functions of tolerance factor, bond angle and temperature.[12] BD indicates the bond length disproportionation. The metal-insulator transition is associated with a symmetry reduction to a monoclinic structure, accompanied by a breathing

distortion of the NiO_6 octahedra, creating two inequivalent Ni sites in the insulating phase. Such a breathing distortion leads to a bond-disproportionate state with long and short Ni-O bonds and lowers the symmetry. Notice that the scale of the Ni-O-Ni angle is non-linear. The t values are calculated from experimental measurements of the R-O and Ni-O distances and therefore differ from the theoretical ones, which assume a purely ionic bonding. Reprinted with permission.[12]

From the phase diagram in Figure 2.4, it can be concluded that T_{MI} is related to the degree of orthorhombic distortion. As the distortion increases, which means smaller Ni-O-Ni bond angle, overlapping between Ni 3d and O 2p orbitals is decreased, leading to the decrease of the bandwidth (W) of the system. So T_{MI} increases up to 600 K for $LuNiO_3$.[19]

2.1.4 Tuning the electronic phase of $RNiO_3$ thin films

The development of thin film deposition techniques enables the fabrication of high quality $RNiO_3$ thin films. Such thin films can be controlled at atomic scale to investigate effects of various factors on their electronic properties, such as strain, carrier concentration, and dimensionality etc., as presented in Figure 2.5.

For epitaxial thin films, strain due to the different lattice constants of the film and substrate is inevitable. The out-of-plane lattice parameter of the film will expand (under compressive strain from substrate) or contract (under tensile strain from substrate), leading to distortions of octahedrons in the thin film. For $RNiO_3$, the NiO_6 units mainly have two ways to accommodate the strain. It can adopt a Jahn–Teller distortion, for which the Ni-O-Ni bond angle will not change but only the bond length changes. Alternatively, Ni-O-Ni bond angles will change to accommodate the strain.

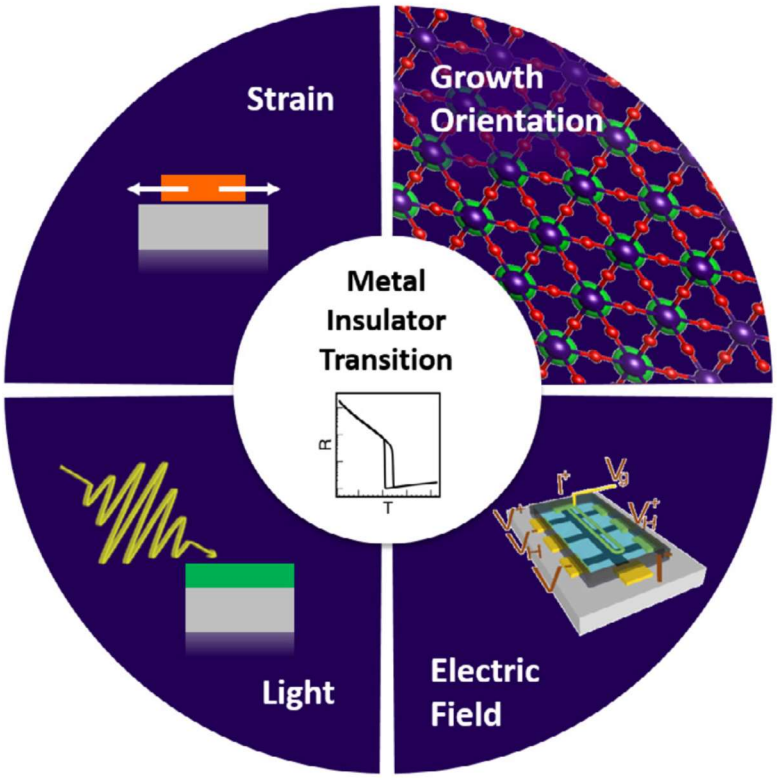

Figure 2.5 Different methods can be used to tune the metal-insulator transition in $RNiO_3$ thin films such as strain, growth orientation, light and electric field. Reprinted with permission.[12] Copyright 2018, IOP publishing, Ltd.

Strain effect in $RNiO_3$ thin films has been heavily investigated and proven to be an effective tool to modulate the MIT.[20-24] For example, as shown in Figure 2.6, for $NdNiO_3$, when the strain changes from tensile to compressive, T_{MI} gradually decreases and eventually metallic phase is stabilized under high compressive strain. Not only for $NdNiO_3$ films, other $RNiO_3$ thin films also show similar behavior, indicating that strain induced electronic phase evolution is universal in $RNiO_3$ thin films.[22]

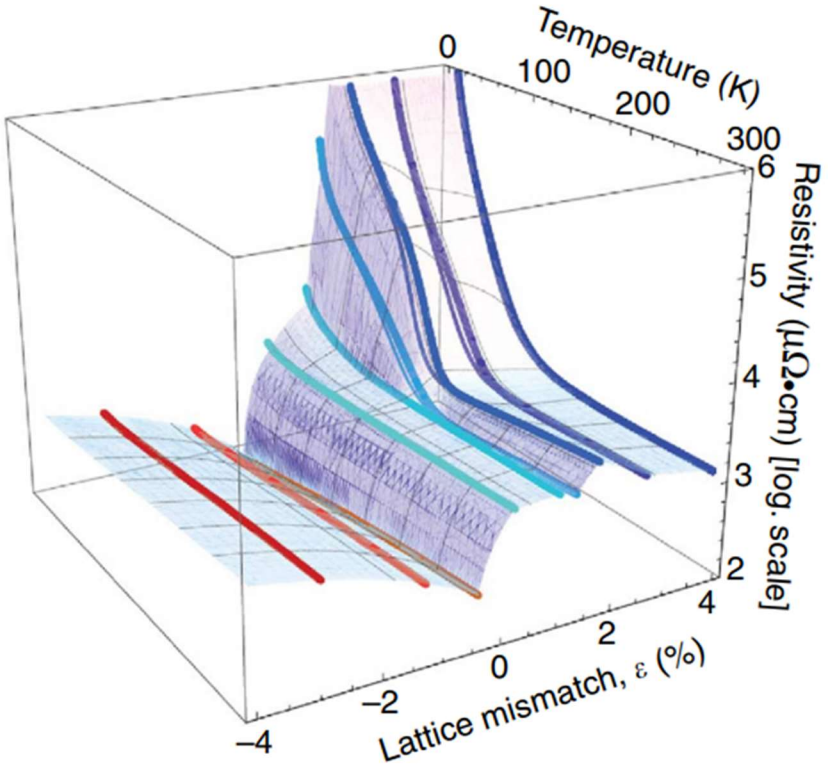

Figure 2.6 (a) Lattice mismatch dependence of MIT in $NdNiO_3$ epitaxy thin films. Reprinted with permission.[22] Copyright 2013, Nature Publishing Group.

Effect of electron or hole doping on the MIT of $RNiO_3$ have been studied by using chemical substitutions. For example, polycrystalline $NdNiO_3$ samples were doped with Th^{4+}, Ce^{4+}, Sr^{2+} and Ca^{2+} cations, among which Th^{4+} and Ce^{4+} are electron donors while Sr^{2+} and Ca^{2+} are hole donors. It was observed that by varying the dopant concentration between 1% and 10%, the MIT was progressively suppressed independent of the dopant type. Such suppression of MIT was attributed to the lattice distortion induced by steric effects and the change in the electron concentration.[25] However, the effect of electron concentration sometimes dominates over the steric effects in some systems and controls T_{MI}. For example, doping with Ce^{4+} and Th^{4+}, which is expected to stabilize the insulating phase by distortion, in fact results in the weakening of the MIT. Similar studies were conducted on polycrystalline $SmNiO_3$ and $NdNiO_3$, where oxygen vacancies were introduced to achieve electron doping.[26] The results show that as doping concentration increases, the MIT is suppressed. Note that these studies were conducted on

polycrystalline ceramic samples of $RNiO_3$. For epitaxial thin films, the situation may change due to lattice strain and reduced dimensionality.

Field effect provides another strategy to tune the electric properties of $RNiO_3$. Such experiments have been conducted on devices based on $LaNiO_3$,[27] $NdNiO_3$[28] and $SmNiO_3$[29] thin films. For $LaNiO_3/SrTiO_3$ heterostructures, the carrier density was modulated by ~10% using field effect. Films with thickness smaller than 8 unit cell (u.c.) started to show a MIT, as shown in Figure 2.7a. Note that bulk $LaNiO_3$ is metallic and does not show MIT. The inset shows a back-gate geometry, in which the dielectric layer is $SrTiO_3$ substrate itself. Figure 2.7b shows sheet resistance (R_{sheet}) measurements for a 6 u.c. thick film when gate voltages varying between -300 and 300 V. The inset shows the R_{sheet} versus applied gate voltage at 4.2 K. A change in R_{sheet} of ~10% from -300 to 300 V is observed.

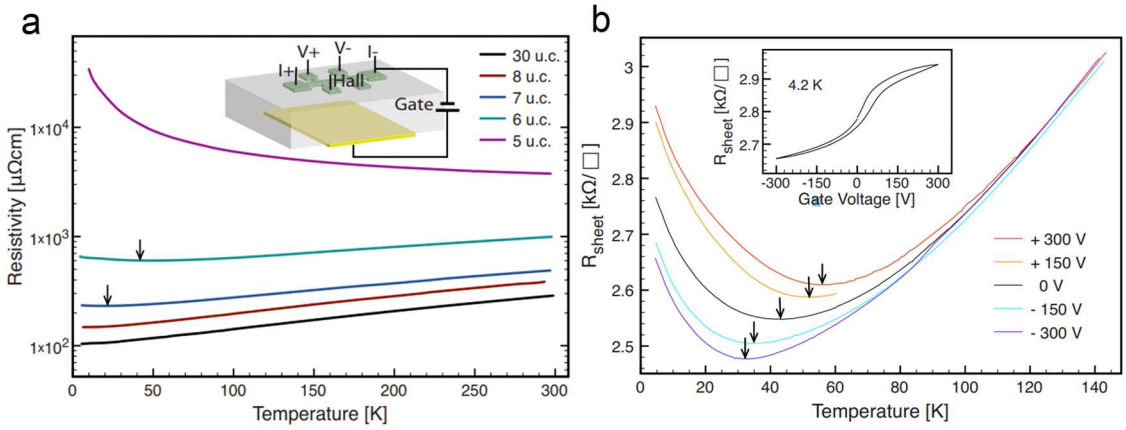

Figure 2.7 (a) Temperature dependence of the resistivity for a series of $LaNiO_3$ films with thickness ranging from 5 to 30 u.c. (b) R_{sheet} vs temperature for a 6 u.c. film and for different applied gate voltages. The inset shows the R_{sheet} vs applied voltage at 4.2 K. Reprinted with permission.[27] Copyright 2009, American Institute of Physics.

Similar measurements were performed on $NdNiO_3/LaAlO_3$ films.[30] As shown in Figure 2.8, very large shifts of T_{MI} (up to 50 K) and giant conductivity modulations were achieved with electric field applied to the gate, which was attributed to pure electrostatic effects, excluding any influence from structural or chemical changes in the material.

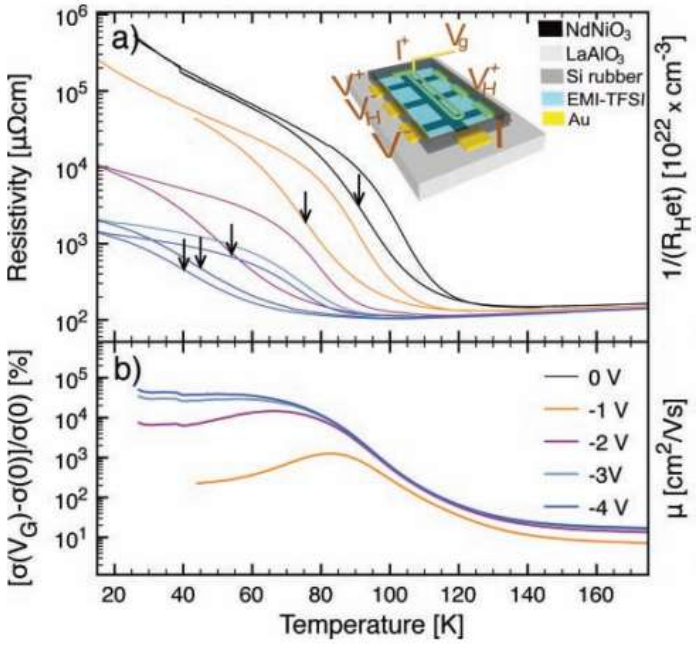

Figure 2.8 Resistivity as function of temperature of an 8 u.c. $NdNiO_3$ film under different gate voltages. The arrows indicate T_{MI} and the inset shows a sketch of the device. Reprinted with permission.[30] Copyright 2010, Wiley-VCH.

These studies took advantage of the electric double layer in ionic liquid, which enables very large modulation of carrier density on the order of ~ 10^{14}-10^{15} cm^{-2}. Inspired by these results, $RNiO_3$ based modulation-doped Mott field effect transistor (MMFET) was proposed, in which MIT is activated or deactivated by the gate voltage.[28] Apart from gate voltage controlling, ferroelectric field effect device was also designed, in which the resistivity of $LaNiO_3$ conducting channel was modulated by a ferroelectric $Pb(Zr,Ti)O_3$ gate.[31] Similar devices were also introduced in $Sm_{0.5}Nd_{0.5}NiO_3$ films.[31, 32] Finally, $SmNiO_3$ based field effect transistors, which mimics the behavior of neural synapses, were developed.[33]

2.2 Questions to be clarified based on literature review

Based on the literature review, it is clear that significant advances have been achieved in understanding the electronic properties of $RNiO_3$. The mechanisms of MIT have been widely investigated and several models have been proposed. Different strategies have

been used to tune the electronic phase of $RNiO_3$ and related applications based on $RNiO_3$ have been developed. However, there are still questions to be answered and improvements to be made.

Firstly, it has been shown that oxygen vacancy, intrinsic defect in $RNiO_3$, suppresses the MIT of polycrystalline bulk ceramic samples. This effect was explained by the extra electronic states introduced within bandgap. However, polycrystalline samples contain randomly oriented grains with many grain boundaries and non-uniform local strains, as well as various defects, making it difficult to pinpoint the origin of the observed effects. Epitaxial thin films, on the other hand, contain much less defects and well-controlled strains. They are ideal for fundamental physics study. It is thus valuable to investigate the effect of oxygen vacancy on the transport behavior, especially the MIT, in $RNiO_3$ epitaxial films and elucidate the underlying mechanism.

Secondly, thin films are required for certain applications such as photovoltaic cells and photo-detection. If the oxygen vacancy content in $RNiO_3$ can be controlled, one would expect that the band structure could be tuned as well. It would thus be interesting to find out how the light absorption property of $RNiO_3$ films could be affected by introducing oxygen vacancies into them. Subsequently, can we design heterostructures using the band engineered $RNiO_3$ films for solar energy harvesting and photo-detection?

Lastly, since oxygen vacancies can be charged (by losing the electrons) and the Ni-O bond is relatively weak as compared to other transition metal-oxygen bonds, would it be possible to move the oxygen vacancies and control their distribution in a heterostructure? If possible, how would the transport behavior of the heterostructures be affected, and could they be used for resistive-switching based non-volatile memory?

2.3 PhD in Context of Literature

In this project, I try to clarify the questions arising from literature review. My contributions to the field are as following:

Firstly, high quality epitaxial $RNiO_3$ thin films were successfully fabricated using PLD. Both post-deposition vacuum annealing and controlling the oxygen pressure during deposition have been used to introduce oxygen vacancies into the films. An insulating phase can be stabilized at room temperature by the oxygen vacancies, and the process is reversible. By combining structural characterization, transport measurements and energy band analysis, I propose a model to explain the bandgap opening in $RNiO_3$ thin films by oxygen vacancies. Furthermore, compared with the post-deposition vacuum annealing method, directly controlling the oxygen pressure during thin film growth is proven to be more effective. These results improve our understanding of MIT in $RNiO_3$ thin films and suggest potential applications of them in various optoelectronic devices.

Secondly, I have explored applications of the band engineered $RNiO_3$ films for solar energy harvesting and photo-detection. By combining the $RNiO_3$ epitaxial thin films with conductive n-type substrates to for heterostructures, photovoltaic cells have been developed and their performances optimized systematically. The highest energy conversion efficiency achieved is 1.1%. Also, photodetectors based on $RNiO_3$ heterojunctions were also tested. They are self-powered and very sensitive to a wide spectrum of light.

Thirdly, electric-field controlled oxygen vacancy migration was achieved in $RNiO_3$ thin films. This leads to giant resistive switching in $RNiO_3$-based heterostructures, which can be used for non-volatile memory. The evidences of oxygen migration were obtained and a clear correlation between oxygen vacancies and interface barrier tuning was established. Such devices show excellent data retention and fatigue performances and they are physically and chemically stable in air. The resistive switching behavior was confirmed to be universal to $RNiO_3$.

These results open new possibilities for the development of multifunctional electronic devices based on nickelates.

References

[1] G. Demazeau, A. Marbeuf, M. Pouchard, and P. Hagenmuller. *J. Solid State Chem.* **1971**, 3, 582-589.

[2] Y. Matsumoto, H. Yoneyama, and H. Tamura. *Bull. Chem. Soc. Jpn*. **1978**, 51, 1927-1930.

[3] C. Rao, O. Parkash, and P. Ganguly. *J. Solid State Chem.* **1975**, 15, 186-192.

[4] K. Asai, H. Sekizawa, K. Mizushima, and S. Iida. *J. Phys. Soc. Jpn.* **1977**, 43, 1093-1094.

[5] J. G. Bednorz and K. A. Müller. *Rev. Mod. Phys.* **1988**, 60, 585.

[6] S. Jin, T. H. Tiefel, M. McCormack, R. Fastnacht, R. Ramesh, and L. Chen. *Science* **1994**, 264, 413-415.

[7] G. Catalan. *Phase Transitions* **2008**, 81, 729-749.

[8] L. Wang, S. Ju, L. You, Y. Qi, Y. W. Guo, P. Ren, Y. Zhou, and J. L. Wang. *Sci. Rep.* **2015**, 5, 18707.

[9] *MIT in Nickelates*, University of Fribourg **2012**, physics.unifr.ch/en/page/547/.

[10] J. B. Goodenough and J.-S. Zhou. *J. Mate. Chem.* **2007**, 17, 2394-2405.

[11] J. Torrance, P. Lacorre, A. Nazzal, E. Ansaldo, and C. Niedermayer. *Phys. Rev. B* **1992**, 45, 8209.

[12] S. Catalano, M. Gibert, J. Fowlie, J. Íñiguez, J.-M. Triscone, and J. Kreisel. *Rep. Prog. Phys.* **2018**, 81, 046501.

[13] D. Khomskii, *Transition metal compounds*. **2014**, Cambridge University Press.

[14] N. Mott. *Proc. Phys. Soc. London, Sect. A* **1949**, 62, 416.

[15] N. Mott, *Rev. Mod. Phys.* **1968**, 40, 677.

[16] J. Zaanen, G. Sawatzky, and J. Allen. *Phys. Rev. Lett.* **1985**, 55, 418.

[17] A. Bocquet, T. Mizokawa, T. Saitoh, H. Namatame, and A. Fujimori. *Phys. Rev. B* **1992**, 46, 3771.

[18] T. Mizokawa, A. Fujimori, H. Namatame, K. Akeyama, and N. Kosugi. *Phys. Rev. B* **1994**, 49, 7193.

[19] S. Barman, A. Chainani, and D. Sarma. *Phys. Rev. B* **1994**, 49, 8475.

[20] G. Catalan, R. Bowman, and J. Gregg. *Phys. Rev. B* **2000**, 62, 7892.

[21] F. Conchon, A. Boulle, R. Guinebretière, E. Dooryhee, J.-L. Hodeau, C. Girardot, S. Pignard, J. Kreisel, and F. Weiss. *J. Phys. Condens. Matter* **2008**, 20, 145216.

[22] J. Liu, M. Kargarian, M. Kareev, B. Gray, P. J. Ryan, A. Cruz, N. Tahir, Y.-D. Chuang, J. Guo, and J. M. Rondinelli. *Nat. Commun.* **2013**, 4, 2714.

[23] F. Bruno, K. Rushchanskii, S. Valencia, Y. Dumont, C. Carrétéro, E. Jacquet, R. Abrudan, S. Blügel, M. Ležaić, and M. Bibes. *Phys. Rev. B* **2013**, 88, 195108.

[24] P.-H. Xiang, N. Zhong, C.-G. Duan, X. Tang, Z. Hu, P. Yang, Z. Zhu, and J. Chu. *J. Appl. Phys.* **2013**, 114, 243713.

[25] J. García-Muñoz, M. Suaaidi, M. Martínez-Lope, and J. Alonso. *Phys. Rev. B* **1995**, 52, 13563.

[26] I. Nikulin, M. Novojilov, A. Kaul, S. Mudretsova, and S. Kondrashov. *Mater. Res. Bull.* **2004**, 39, 775-791.

[27] R. Scherwitzl, P. Zubko, C. Lichtensteiger, and J.-M. Triscone. *Appl. Phys. Lett.* **2009**, 95, 222114.

[28] J. Son, S. Rajan, S. Stemmer, and S. James Allen. *J. Appl. Phys.* **2011**, 110, 084503.

[29] S. Hyeon Lee, M. Kim, S. D. Ha, J.-W. Lee, S. Ramanathan, and S. Tiwari. *Appl. Phys. Lett.* **2013**, 102, 072102.

[30] R. Scherwitzl, P. Zubko, I. G. Lezama, S. Ono, A. F. Morpurgo, G. Catalan, and J. M. Triscone. *Adv. Mater.* **2010**, 22, 5517-5520.

[31] M. Marshall, M. Marshall, A. Malashevich, A. S. Disa, M.-G. Han, H. Chen, Y. Zhu, S. Ismail-Beigi, F. J. Walker, and C. H. Ahn. *Phys. Rev. Appl.* **2014**, 2, 051001.

[32] L. Zhang, X. Chen, H. J. Gardner, M. A. Koten, J. E. Shield, and X. Hong. *Appl. Phys. Lett*. **2015**, 107, 152906.

[33] J. Shi, Y. Zhou, and S. Ramanathan. *Nat. Commun.* **2014**, 5, 4860.

Chapter 3

Experimental Methodology

This chapter introduces the main techniques used in samples synthesis and characterizations. To ensure the high quality of epitaxial thin films, all samples are prepared by pulsed laser deposition (PLD), which is widely used to fabricate functional oxide thin films. Physical properties measurements system (PPMS), atomic force microscopy (AFM), x-ray diffraction (XRD) and other relevant techniques are introduced in this chapter. They are used to obtain the electrical transportation properties, surface morphology, crystal structure and other information of the samples to elucidate the electronic structure of the films. The reasons for choosing these techniques are explained in this chapter as well.

3.1 Rationale for choosing the materials and characterization techniques

Transition metal oxide thin films have attracted increasing attention during the past few decades owing to their exotic electronic and magnetic properties. For normal metals and semiconductors, their physical properties are usually determined by a certain dominating factor. For example, normal metals conduct electricity because of the weak interaction between electrons and lattice. Positive ions are simply packed together by metallic bonds with delocalized electrons, which makes normal metals always conductive and lack of diversity. While for transition metal oxides, resulting from the high electronic polarizability and strong electronic correlation, the energy scales of Coulomb repulsion, orbital band-widths and Hund's exchange become similar.[1] The competition among these interactions leads to the strong interplay between lattice, electrons and orbitals, resulting in unusual properties such as metal-insulator transition (MIT), giant magnetoresistance, and superconductivity etc. Such complexity of transition metal oxides makes it possible to tune their physical properties by various external perturbations, which is ideal for physics study and potential applications. As a key member of transition metal oxides family, rare earth nickelates ($RNiO_3$) are interesting. The hybridization between O 2p orbitals and Ni 3d orbitals in $RNiO_3$ is very sensitive to strain and oxygen content, which enables the manipulating of their electronic structures by simply adjusting the deposition parameters during thin film growth. Tuning the electronic phase of $RNiO_3$ thin films into suitable states may find applications in photovoltaic cells, photodetectors and non-volatile memories. This forms the reason of choosing $RNiO_3$ films as the subject of study in this thesis.

To prepare high quality $RNiO_3$ thin films for our study, pulsed laser deposition (PLD) is used. PLD has been used for the deposition of high-quality functional oxide epitaxial thin films since 1980s and is one of the most popular thin film technologies currently. More details and advantages of the technique will be presented in Section 3.2

X-ray diffraction (XRD) is a common technique used to obtain information about the crystal structure. Here, high-resolution X-ray diffraction (HR-XRD) is useful in

confirming the phase purity and epitaxial characteristic of the thin films, which is very helpful in excluding effects of secondary phases. Also, lattice constant can be calculated, which is very important to clarify the origin of changes in transport properties.

Atomic force microscopy (AFM) is chosen to study the morphologies of $RNiO_3$ films. Samples with perfect epitaxial characteristics maintain very low surface roughness, usually less than 1 nm, which can be obtained from the AFM images. Although HR-XRD can confirm the epitaxial characteristic of the films, surface defects are usually invisible to X-rays and affect the performance of devices. AFM makes sure that all the $RNiO_3$ thin films, some of which are used to prepare various electronic devices, have smooth surface without cracks or pinholes. Furthermore, AFM can be used to obtain the film thickness, which is used to calculate the growth rate of $RNiO_3$ thin films under different PLD parameters.

Transmission electron microscopy (TEM) is used to probe the interface between $RNiO_3$ thin films and substrates. This is particularly important because all the devices investigated in this thesis rely on diode behavior from the junction formed by $RNiO_3$ and the substrate. With clear images of the interface and other information obtained using TEM related techniques such as electron energy loss spectroscopy (EELS), oxygen vacancy migration or changing of Ni valence state can be investigated, which provide direct evidences for the corresponding hypothesis.

Physical property measurement system (PPMS) is used to measure the temperature dependence of electrical transport properties of $RNiO_3$ thin films. Equipped with a liquid Helium cooling system, PPMS helps to obtain the resistance versus temperature plots down to a temperature as low as a few Kelvin, which reveals the MIT in the $RNiO_3$ thin films, if any.

Ultraviolet-visible spectroscopy (UV-Vis) is used to obtain the transparency or light absorption spectrum of $RNiO_3$ thin films, from which bandgaps of the films can be

derived. Such information is essential for the potential applications of $RNiO_3$ thin films in various optoelectronic devices.

Ellipsometry is the technique used to get the absorption coefficient of the $RNiO_3$ thin films. Ellipsometry is very sensitive to the states of samples and the results complement that obtained using UV-Vis.

X-ray photoelectron and X-ray absorption spectroscopy (XPS and XAS) are used to probe the valence state of Ni ions in $RNiO_3$. The results help to establish the ratio between Ni^{2+} and Ni^{3+}, which is directly related to oxygen vacancies in the films

Ultraviolet photoelectron spectroscopy (UPS) is the technique used to test the work function of $RNiO_3$. Combined with information obtained from other techniques, we can establish the band structure of the films and band diagrams across the heterostructures, which are critical in analyzing the performance of various devices.

3.2 Sample synthesis

3.2.1 Preparation of materials

Strontium titanate ($SrTiO_3$) (001) single crystal substrates and niobium-doped strontium titanate (Nb-$SrTiO_3$) substrates were purchased from Hefei Kejing Materials Technology CO., Ltd. Single-side polished $SrTiO_3$ substrates were used to prepare films for XRD and electrical properties tests while double-side polished $SrTiO_3$ substrates with high transparency were used to prepare films for UV-Vis tests. 5 weight percent (5 wt. %) Nb-$SrTiO_3$ substrates were used as conductive n-type semiconductors. All substrates were cleaned in ethanol (95%) and acetone (95%) at room temperature for 15 mins respectively in an ultrasonic cleaner. Such a cleaning process was repeated at least twice until no microparticles appeared in beaker. The substrates were then cleaned with nitrogen (N_2) gas to remove the left solution and kept in a dry box for future use. Polycrystalline $RNiO_3$ targets were purchased from Nanjing Piailu Electronic Tech. Co., Ltd.

3.2.2 Pulsed Laser Deposition

Pulsed laser deposition is one of the most versatile physical vapor deposition (PVD) techniques commonly used for research. The principle of PLD is that focused laser pulses with high energy heat the target material into a plasma plume inside a vacuum chamber. Then the evaporated materials are deposited onto the substrate forming thin films. This process happens either inside high vacuum or specific gas environment such as oxygen (O_2) and argon (Ar). The simplified diagram of a PLD system is shown in Figure 3.1.

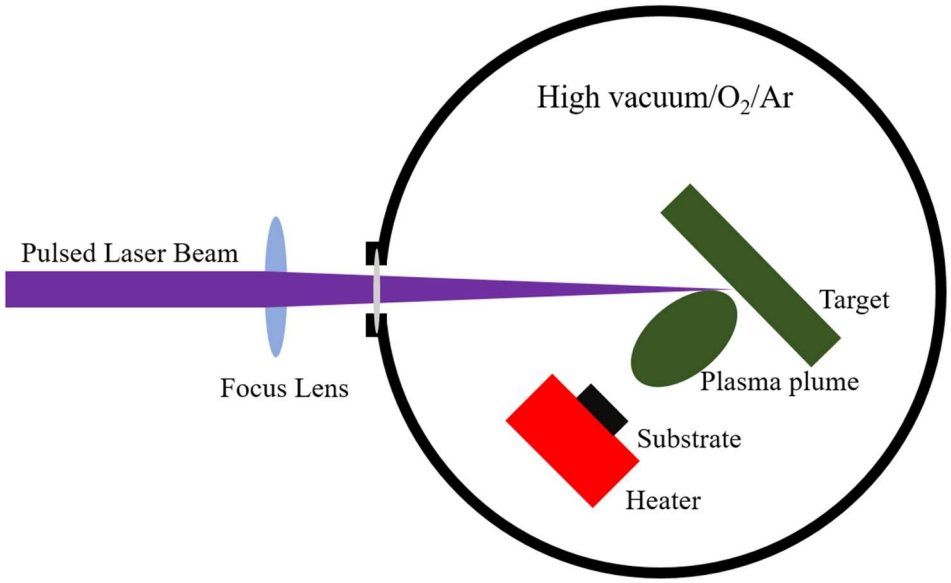

Figure 3.1 Schematic illustration of a PLD system.

Although the setup of PLD is simple, the detailed film growth process is quite complex. Generally, the thin film quality is affected by four parameters: laser pulse energy, distance between the target and substrate, substrate temperature and background gas pressure in the chamber.

Firstly, creation of plasma plume has requirements on laser wavelength, pulse duration, power density and repetition rate. For excimer lasers, the output laser wavelength is tunable by changing the operating gas. By using different gas combinations such as XeF,

XeCl, KrF, KrCl and ArF, the corresponding output laser wavelengths are 351, 308, 248, 222, 193 nm, respectively. Laser with lower wavelength has higher photon energy, which increases the evaporation and ionization rate of target materials because the interactions between photons and lattice are enhanced. Excimer laser used in PLD usually have a pulse duration of ~10 ns, which provide enough time for the heat transfer into bulk material causing melting and evaporation. When photons interact with a solid material, the photon energy is absorbed by the lattice and electronic relaxation happens.[2] The electronic relaxation processes are very fast within typically 10^{-14}-10^{-13} s and release heat at the same time. The interaction between photons and lattice happens within 10^{-13} s, then the thermal diffusion from surface to bulk occurs during the left time of laser pulse duration. Power density of laser pulses affects the number of photons delivered to the surface of target in a unit area. Together with repetition rate and the distance between the target and substrate, they will determine the degree of supersaturation of the evaporated material on the surface of substrate, which directly influences the thin film growth.

Substrate materials play important roles in thin film growth by PLD. In the case for epitaxial growth of transition metal oxide thin films, substrates must be single crystal with lattice constant equal or similar to that of the target materials. Usually, heteroepitaxy can tolerate a lattice mismatch of less than ~5 % and larger lattice mismatch may induce more defects and even failure of the epitaxy.

Background gas pressure is another factor that affect the thin film growth by PLD. During deposition, the chamber will be under high vacuum or low pressure of certain gas. In the case of high vacuum (~ 10^{-6} pa), The plasma plume expands freely in vacuum without energy loss. Species from the plume arrive at the surface of the substrate with ultra-high kinetic energy, resulting in the fast growth of films. High particle densities are formed at the surface. In the case of low vacuum (10-100pa), background gas blocks the expansion of plasma plume and reduces the mean free path of the plume species. Number of interactions between plume and gas is increased to form more atomic and diatomic species. Eventually the plasma plume will be confined within a short distance. Such

phenomenon is presented in Figure 3.2 that as the oxygen pressure increases from 0.4 to 40 Pa, obvious plasma plume confinement is observed.

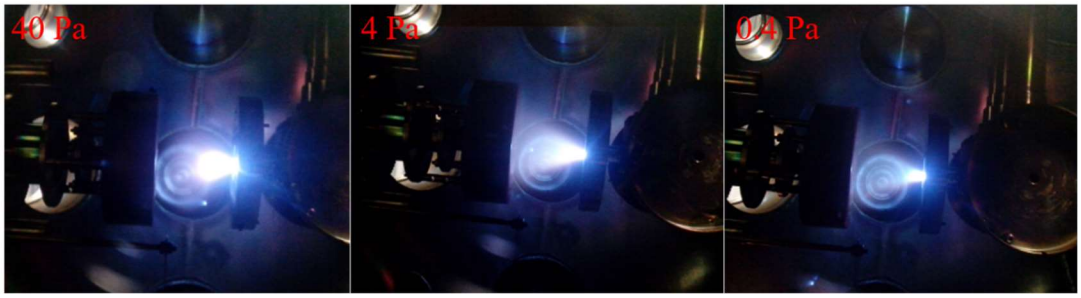

Figure 3.2 Optical images of plasma plume formed during $RNiO_3$ thin film deposition. The oxygen pressure changes from 40 to 0.4 Pa and the plasms plume expands.

When species of the plume arrive at the substrate surface, smaller clusters firstly nucleate randomly. These clusters tend to dissociate into mobile species that will nucleate new clusters of a different size during the time between two pulses. The next laser pulse will repeat the same process. The only difference is that previously formed clusters will meet with new clusters and atoms. To enable the clusters and atoms with enough surface mobility, the substrate temperature needs to be maintained at around 500-700 ℃ usually for epitaxial growth of oxide thin films. As the laser pulses continue to ablate target materials onto the substrates, there are different growth modes: layer-by-layer growth, island growth mode and a layer-by-layer growth followed by an island growth mode.[3, 4] Layer-by-layer mode requires good lattice match. It also needs a high surface mobility of the arriving atoms and ions, which can be provided by their kinetic energy and high temperature of the substrate. Island growth happens when atoms are more strongly bound to each other than to the substrate thereby forming clusters. An intermediate state may lead to the third mode of film growth. It usually occurs in the case that lattice mismatch between substrate and film is relatively large.

The PLD system (PLD-450) used in this study was purchased from SKY Technology Development Co., Ltd, as shown in Figure 3.3. The chamber is equipped with mechanical pump and turbo pump with ultimate background pressure reaching 10^{-6} pa. The target

holder is compatible with a target diameter up to 60 mm. Four different targets can be loaded into chamber at the same time to support multilayer deposition. The self-rotation of the target is controllable and reaches a maximum speed of 60 rpm. The excimer laser (COMPex 205) was purchase from Coherent Inc. The wavelength of laser is 248 nm and the pulse duration is 20 ns. The laser beam dimension is 24 by 10 mm before being focused. The maximum repetition rate of the laser pulses reaches 50 Hz and maximum energy output is 750 mJ.

Figure 3.3 The PLD-450 deposition system used in this study.

For the experiments in this study, all substrates were cleaned as introduced in Section 3.2.1. The substrates were then fixed in the center of substrate holder with silver paste and heated at 160 ℃ for 15 mins to dry the silver paste. After the targets and substrates were loaded into the chamber, mechanical pump was started to decrease the background pressure to less than 10 pa followed by turbo pump to decrease the background pressure to less than 10^{-4} pa. A temperature controlling program was used to increase the temperature to the setting point. (heating rate was fixed at 12℃/min) When the real-time temperature reached at 400 ℃, pure O_2 gas was introduced with a flow meter to adjust

the pressure inside chamber. When the substrate temperature was stabilized at the setting point and oxygen pressure reached the desired value, the self-rotation of target and substrate holder were initiated with a speed of 30 rpm. Laser pulses were focused by lens to a spot size of 4 mm^2. A pre-sputtering process was conducted to clean the surface of the target. During deposition, the energy of laser pulse arriving at the target surface was maintained at 40 mJ, which was verified by an energy meter before the experiment. The repetition rate of the laser pulses was set to 5 Hz. After the deposition, self-rotation of target and substrate holder was stopped. The temperature was kept for another 10 mins to undergo annealing. Then the temperature was decreased to 300 ℃ at a rate of 12℃/min to room temperature.

3.3 Characterization

3.3.1 High Resolution X-ray Diffraction

X-ray diffraction is a technique used to identify the crystal structure of materials. The incident X-rays are diffracted by the crystal planes following the well-known Bragg's Law. As shown in Figure 3.4, when incident x-rays are diffracted from a crystal lattice plane, the angle of incidence equals to angle of diffraction. The wavelength of the X-rays, the distance between the crystal planes and the incident angle fulfill the following equation:

$$2d\sin\theta = n\lambda,$$

where n is any integer, d is the lattice constant. By measuring the angles and intensities of the diffracted x-rays, a diffraction pattern can be obtained to identify the phase of a sample.

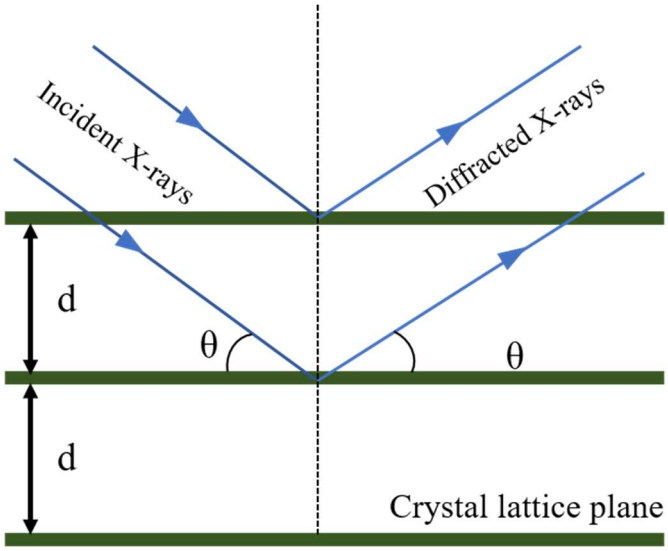

Figure 3.4 Schematic demonstration of Bragg's law.

There are two commonly used scan modes for conducting XRD measurements. One is the "θ - 2θ" scan which is usually used for powder diffractions, in which the detector is rotated twice as fast as the sample following the same axis. The second one is ω-scan, in which the detector is fixed in position and the sample is rotated. It is usually conducted on single crystal samples. By Ewald sphere construction,[5] it is clear that the scan direction is transversal in reciprocal space.[6] Thus, the so-called 'rocking curve' is obtained, which reveals the epitaxial quality of thin films.

For epitaxial thin films, one often needs to measure variations ($\Delta d/d$, where d is the lattice constant) in lattice constant of between 10^{-2} and 10^{-4}. The corresponding angular change ($\Delta\theta$, where θ is the incident angle of X-ray) can be calculated from the differentiation of Bragg's law:

$$\frac{\Delta d}{d} = \frac{\Delta \lambda}{\lambda} - \frac{\Delta \theta}{tan\,\theta}.$$

Detection of such small signal leads to strict requirements on the X-ray generators. X-rays are usually generated by X-ray tubes, inside which the accelerated electrons from cathode to anode undergo an energy loss resulting in the generation of X-ray. The source should provide strong energy so that the diffracted X-ray wave has larger energy than a threshold value to be detected. Also, to maintain the high resolution, the line width of the

incident X-ray should be as narrow as possible. To achieve this, monochromators are used in the system. Monochromators can separate light with different wavelength and direct the desired chromatic light to the exit slit. They use either the optical dispersion in a prism, or a diffraction grating to spatially separate light with different wavelength. Successfully implemented monochromator can produce X-ray beam with only 5% of the original bandwidth and the wavelength spread ($\Delta\lambda/\lambda$) can reach the scale of 10^{-5}. Except for very strong monochromic X-ray incident beam, a good X-ray detector is also necessary to achieve high-resolution XRD patterns.

High resolution XRD (HR-XRD) patterns help researchers to obtain information on sample composition, phase, thickness, and strain state. It is one of the most popular non-destructive characterization techniques for materials study. In this project, the HR-XRD system used (Figure 3.5, SmartLab) was purchased from Rigaku Co.

Figure 3.5 Picture of the sample stage of the HR-XRD used in this thesis.

3.3.2 Atomic Force Microscopy

Atomic force microscopy (AFM) is a technique used to probe the sample surface[7, 8] Unlike optical microscopes, which use visible light and lens system to magnify small subjects, AFM uses a sharp tip to touch or feel the surface so that the topography can be obtained. The schematic diagram of an AFM system is show in Figure 3.6, which mainly contains four components, i.e. sample stage, cantilever, laser and photo detector besides the controlling unit.

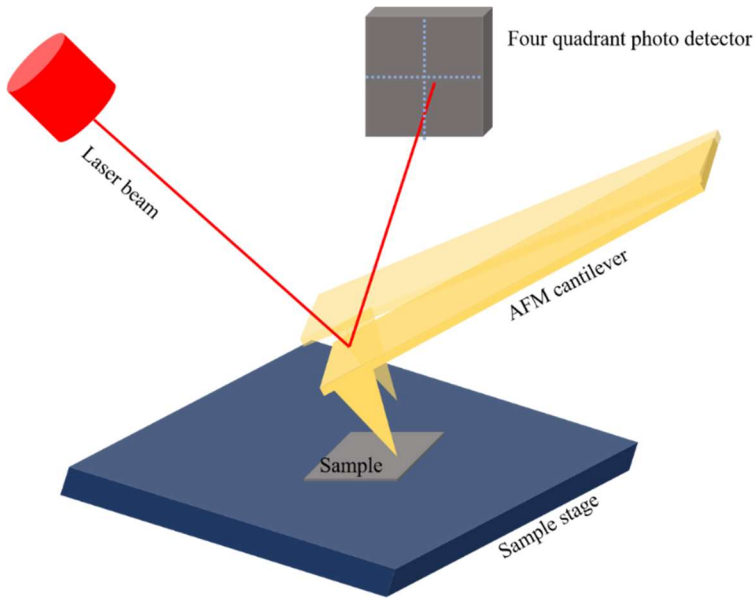

Figure 3.6 Schematic demonstration of the working principle of an atomic force microscopy.

As Figure 3.6 shows, an AFM measures the vertical movement of a cantilever through the displacement of reflected laser spot on a photodiode. Although the movement of cantilever itself may be quite small, the reflected laser beam magnifies the movement and leads to the very high sensitivity of AFM. The photodiode is divided into four quadrants and the position of the laser spot is determined by the difference in signals generated from the four quadrants.

There are two commonly used operating modes of AFM: contact and non-contact modes. In contact mode, a sharp tip at the end of the cantilever touches the sample surface directly and scans across a region to collect topography information. It is less used due to potential damage to the sample. In non-contact mode, the tip does not touch the surface constantly, which reduces the possibility of sample damage. Instead, the cantilever is driven by a piezo-actuator to vibrate at a certain frequency (close of away from the resonance frequency of the cantilever). When the cantilever scans along the sample surface, interaction between the sample and tip would reduce its vibration amplitude, and a feedback system will adjust the vertical position of the cantilever to maintain a constant vibration amplitude. The adjustment made during the scan is recorded. When there is

only mechanical interaction between the tip and sample, i.e. the tip taps the surface during the scan, topography image can be recorded. However, if there are other long-range forces between the tip and the sample such as magnetostatic and/or electrostatic forces, the technique also allows for mapping of magnetic domains and/or charge distributions. In these cases, a 'lift height' scan is conducted. During the first scan, the tip is lowered to be close to the surface, so topography information will be obtained during the scan. Afterward, the cantilever is lifted up by a preset distance from the surface, retrace the topography along the same path (maintaining a constant lift height), and any changes in the vibration amplitude would be due to the long-range force. These techniques are often called magnetic force microscopy (MFM) and electrostatic force microscopy (EFM).

The AFM system used in this work (Asylum MFP-3D) was purchased from Oxford Instruments. Samples are fixed onto the stage with double-sided tape and the stage is located on an air-driven stabilizer to minimize the environmental noise. The AFM Probes (NCH) were purchased from NanoWorld AG. These cantilevers have resonance frequency of ~320Hz and the force constant is ~42 N/m. The length, mean width and thickness of the cantilevers are 125 μm, 30 μm and 4 μm, respectively. The probes are made from monolithic silicon which is highly doped to dissipate static charges. The tip is shaped like a polygon-based pyramid with a typical height of 10-15 μm. A typical tip radius of curvature is less than 8 nm which gives rise to nanometer scale resolution of the AFM.

3.3.3 Transmission Electron Microscopy

Transmission electron microscopy (TEM) is a powerful tool for microstructure and interface characterizations. The general mechanism of a TEM is that an electron beam with high energy goes through a sample of 100 nm or less and the interactions between electrons and atoms provide clues for crystal structure and elements presented, which will be collected by detectors to be analyzed. A simplified diagram of TEM was show in Figure 3.7.

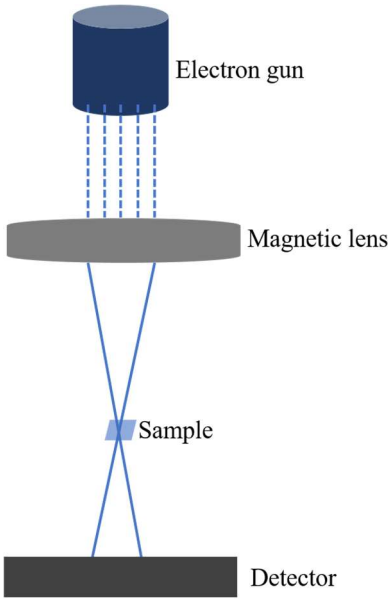

Figure 3.7 Illustration of the working principle of TEM.

The TEM shares the same basic principles as an optical microscope but uses electrons instead of photons. Because the wavelength of electrons can be much smaller than that of light, the resolution of TEM reaches picometer, which is orders of magnitudes better than that of optical microscope.

Apart from the high resolution, TEM is usually equipped with multiple detectors for other applications. For example, electron energy loss spectroscopy (EELS) is one common technique integrated inside a TEM to measure the elemental components by means of detecting the inelastic scattering of electrons. Some electrons from the incident beam may lose energy and randomly deflected. The amount of energy loss can be measured by an electron spectrometer, based on which, the reason causing the energy loss may be interpreted. When inelastic scattering happens, the lost energy of electrons is absorbed by atoms or ions leading to electron transition between shells in the atom. Each element possesses a unique arrangement of energy levels so the transitions between different levels require characteristic energy values. Thus, the energy loss during inelastic scattering can be used to distinguish the type of atoms or ions.

In this study, all TEM measurements were conducted using an ARM-200F (JEOL, Tokyo, Japan) scanning TEM operated at 200 kV with a CEOS Cs corrector (CEOS GmbH, Heidelberg, Germany) to cope with the probe-forming objective spherical aberration. All results were collected by our collaborators from Institute of Physics Chinese Academy of Sciences, Beijing, China.

3.3.4 Physical Property Measurement System

A physical property measurement system (PPMS) is used to measure various physical properties such as electrical transport properties, magnetoresistance, Hall coefficient. it is generally equipped with a helium cooling system which can decrease the temperature inside the PPMS chamber to as low as 5 k with controllable cooling rate. At the bottom of the sample chamber, a 12-pin connector is fixed and wired to the system electronics. The connector allows removable sample holder (so-called 'puck' in PPMS as shown in Figure 3.8) to be inserted and leads electrical signals from samples to the PPMS electronics, which provides the foundation for all PPMS measurements. To minimize the contact resistant, samples cannot be mechanically connected with 'puck' so wire-bonding is generally used to connect the electrodes on the sample surface to the electrodes of puck with metallic wires. Temperature controlling is achieved by means of pumping helium into the annular region where heaters warm the gas to the setting temperature. Multiple thermometers are applied to check the thermal gradients and actual temperature at the sample location.

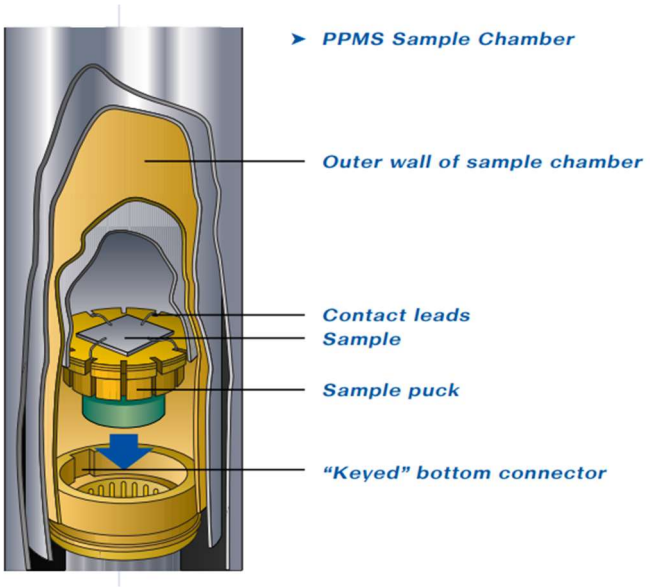

Figure 3.8 Schematic illustration of the inside structure of a typical PPMS.

For this study, the PPMS used was purchased from Quantum Design as shown in Figure 3.9. Linear four-point geometry with Pt top electrodes on the samples was used to test the electrical transport properties at temperatures ranging from 10 to 300 K at a cooling/warming rate of 3 K/min. Hall resistivity as functions of applied magnetic field was tested using hall bar structures at room temperature. An external perpendicular magnetic field was applied while an AC current was used to measure the Hall resistivity. The AC frequency was 10^3 Hz and the duration was 5 s.

Figure 3.9 Picture of the PPMS used in this study.

3.3.5 Ultraviolet-Visual Spectroscopy

Ultraviolet-visual spectroscopy (UV-Vis) is the technique used to measure the absorption of light by a sample. It collects the light passing through a sample and compares it with the incident light. The transmittance is defined as I/I_0, where I and I_0 represent the intensity of light before and after passing through the sample, respectively. It is usually denoted as T%. The absorbance (A) is defined based on the transmittance following:

$$A = -log\left(\frac{T}{100}\right).$$

Basically, an UV-Vis system comprises a light source, a sample holder, monochromators, and a detector. Different UV-Vis systems may be equipped with different radiation sources. Tungsten filament (300 - 2500 nm), Xenon lamp (160 - 2000 nm) or recently developed light emitting diodes (LED) are the most common ones. The detector is typically made from photodiodes which convert photons to electrons. Monochromators can filter the light so that only light of a single wavelength reaches the detector at one time. The scanning monochromator moves the diffraction grating to "step-through" each wavelength so that the intensity may be measured as a function of wavelength. The incident light of a UV-Vis is often split into two beams, one of which is used as the reference and the other one passes through the sample. The reference beam intensity is

considered as 100% transmission and the measurement displayed is the ratio of the two beam intensities. Samples are usually placed on the holder with holes on it. The incident light will go through the sample and the hole to arrive at the detector. Note that sample holders are specially prepared for solid samples. Liquid samples don't have holders, instead, transparent container called cuvettes are used.

The analysis of UV-Vis spectra is important to get correct information of the samples. Except for the direct absorbance or transmittance value that can be read from the UV-Vis spectra directly, bandgap of the samples can be derived. Tauc plot is a very useful analysis technique to determine the optical bandgap from UV-Vis spectra, which was introduced by Jan Tauc in the 1960s.[9, 10] He proposed that absorption coefficient (α) and photon energy following the following relationship :

$$\alpha h\nu \propto \left(h\nu - E_g\right)^n,$$

Where h, ν, and E_g represent Planck constant, photon frequency and optical bandgap respectively. The exponent n denotes the nature of transition and can be 1/2, 3/2, 2, and 3 for direct allowed, direct forbidden, indirect allowed and indirect forbidden transitions, respectively. The resulting plot has a linear region, so a simple extrapolation yields the optical bandgap of the material.

In this study, the UV-Vis system (Cary 5000) used was purchased from Agilent Technologies as shown in Figure 3.10. It provides a wavelength range from 175 to 3300 nm. During the experiments, a plain double-side polished (001)-oriented $SrTiO_3$ substrate was used as the reference sample. The sample holder with 2mm-hole was selected to fix the samples. The scan rate and optical slit size was set as 1 nm/min and 1 nm, respectively.

Figure 3.10 Picture of UV-Vis (Cary 5000) used in this thesis

3.3.6 Ellipsometry Measurements

Ellipsometry is an optical technique which measures the difference of light polarization before and after being reflected by a sample. By means of comparing the result with a model, composition, structure, thickness, optical constant and other materials properties can be obtained. The basic setup for an ellipsometry is shown in Figure 3.11.

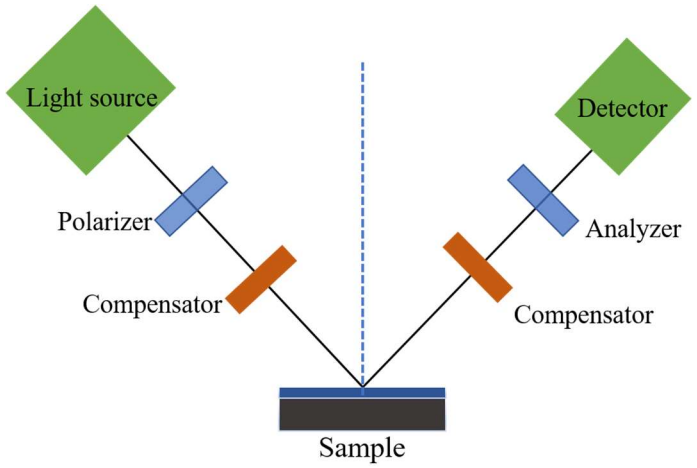

Figure 3.11 Schematic setup of an ellipsometry.

Light is emitted from the source and linearly polarized by the first polarizer. It passes through a compensator and strikes the sample. After being reflected, it passes through

another compensator, an analyzer (the second polarizer), then arrives at the detector. Ellipsometry is an indirect method because it measures the complex reflectance ratio instead of optical or structural information. Modeling must be performed to extract the desired information.[11]

In this study, spectroscopic ellipsometry measurements were performed using a commercially available rotating analyzer instrument with a compensator (V-VASE; J.A. Woollam Co., Inc.) within the spectral range of 0.6 to 6 eV at the Singapore Synchrotron Light Source. All measurements were performed by our collaborators at the Singapore Synchrotron Light Source, National University of Singapore, Singapore.

3.3.7 X-ray Absorption Spectroscopy

X-ray absorption spectroscopy (XAS) is the technique of using continuous x-rays to interact with the inner-shell electrons and generating the spectra reflecting the interaction changes as a function of photo energy. As the valence state of an element changes, the absorption edge position will shift accordingly. It thus allows us to monitor the valence state of Ni ions in $RNiO_3$ and deduce the content of oxygen vacancies. In this study, all XAS measurements were performed by our collaborators at the photoemission station at the Beijing Synchrotron Radiation Facility of Institute of High Energy Physics, Chinese Academy of Sciences.

3.3.8 X-ray Photoelectron Spectroscopy and Ultraviolet Photoelectron Spectroscopy

X-ray photoelectron spectroscopy (XPS) is a spectroscopic technique, which is widely used for the measurement of valence state reflected in binding energy. As each element has its own unique binding energy peaks, it is easy to identify the elemental composition by XPS. The high sensitivity of XPS is suitable for analyzing thin films. When a beam of X-ray irradiates the thin films, the binding energy and number of electrons are simultaneously measured, generating the XPS spectrum.

Compared with XPS, ultraviolet photoelectron spectroscopy (UPS) has smaller energies and is limited to energy levels of valence electrons, but measures with higher resolution.

XPS and UPS measurements were performed in a home-built UHV multi-chamber system with a base pressure better than 10^{-9} torr. The XPS source was monochromatic Al Kα with photon energy at 1486.7 eV. The UPS source was from a helium discharge lamp (21.2 eV). The photoelectrons were measured using an electron analyzer (Omicron EA125). All the measured spectra were adjusted with Shirley type background, shifted with respect to carbon (C-C) XPS peak position due to charging.

References

[1] J. M. Rondinelli and N. A. Spaldin. *Adv. Mater.* **2011**, 23, 3363-3381.

[2] C. W. Schneider and T. Lippert. *Laser Processing of Materials*. **2010**, Springer.

[3] R. Tung, D. Wolf, and S. Yip. *Atomic Level Properties of Interface Materials.* **1992**, Springer.

[4] J. Venables, G. Spiller, and M. Hanbucken. *Rep. Prog. Phys.* **1984**, 47, 399.

[5] P. Ewald. *Acta Crystallogr. A* **1969**, 25, 103-108.

[6] G. Bauer and W. Richter, *Optical characterization of epitaxial semiconductor layers*. **2012**, Springer Science & Business Media.

[7] T. R. Albrecht and C. Quate. *J. Appl. Phys.* **1987**, 62, 2599-2602.

[8] A. Gratz, S. Manne, and P. Hansma. *Science* **1991**, 251, 1343-1346.

[9] J. Tauc. *Mater. Res. Bull.* **1968**, 3, 37-46.

[10] J. Tauc, R. Grigorovici, and A. Vancu. *Phys. Status Solidi B* **1966**, 15, 627-637.

[11] H. G. Tompkins and W. A. McGahan. *Spectroscopic ellipsometry and reflectometry: a user's guide.* **1999**, Wiley.

Chapter 4

Oxygen Vacancy Induced Band Engineering in $RNiO_3$ films

In this chapter, the tuning of the electronic structures of $NdNiO_3$ films by introducing oxygen vacancies is presented using two methods: post-deposition vacuum annealing and adjusting oxygen pressure during deposition. Firstly, by introducing oxygen vacancies via vacuum annealing, an insulating phase of $NdNiO_3$ is stabilized at room temperature with a ~10^6 change in resistance when compared with the as-grown state. The Hall effect, X-ray Photoelectron Spectroscopy (XPS) and ultraviolet photoelectron spectroscopy (UPS) measurements reveal the changes in carrier density and band structure. The insulating phase is explained by the bandgap opening between Ni 3d and O 2p orbitals due to the bandwidth narrowing and Coulomb repulsion enhancement. Secondly, it is shown that adjusting the oxygen pressure during film growth is more effective to introduce oxygen vacancies into $NdNiO_3$ thin films. These results suggest new methods to tune the electronic states of $NdNiO_3$ (and $RNiO_3$ films in general) and improve our understanding of this family of materials.

4.1 Introduction

Although the phase diagram of bulk $RNiO_3$ (Figure 2.4) has been established some 20 years ago, understanding the nature of the insulating phase has been challenging. The strong interplay between orbital, lattice and spin degrees of freedom leads to complex energy landscape of the system, making it difficult to identify the origin of the insulating behavior. In general, there are two models describing an insulting phase: Mott-Hubbard insulators and charge-transfer insulators, which categorize a system depending on the competition among three parameters, i.e., Coulomb repulsion energy (U), charge-transfer energy (Δ) and bandwidth (W). Note that systems with 'negative Δ" are sometimes considered as the third category of insulating phase, but the underlining physics remains the same.

The basic methodology of investigating the origin of the insulating phase of $RNiO_3$ is to tune their electronic structure by various methods such as chemical doping, electrical field control, or strain, and the effects on the stability of the insulating phase provide clues for the underlining principles. For example, it has been observed that T_{MI} of $NdNiO_3$ decreases upon hole-doping by chemical substitution of Ca^{2+} or Sr^{2+} for Nd^{3+}, which can be explained by the closure of the charge-transfer gap between Ni 3d and O 2p bands.[1] Electric field has been used to reversibly control the T_{MI} of MIT in fully-strained ultrathin nickelate thin films. The maximum shift of T_{MI} reached 50 K, which was explained by pure electrostatic effect.[2] Strain was also used to tune the electronic phase of $NdNiO_3$ thin films and a bandwidth-controlled MIT was realized.[3, 4]

Oxygen vacancy plays an important role in the electronic and magnetic properties of strongly correlated systems.[5-11] It is usually treated as double electron donors, which can affect the valance states of transition metal cations in oxides. Oxygen vacancy is intrinsic to oxides and its concentration can be tuned simply by vacuum annealing or adjusting oxygen pressure during sample preparation. Furthermore, as compared to other transition metal oxides such as manganates and cuprates, Ni-O bond is relatively weak [12], making it much easier to generate oxygen vacancies in nickelates and possible to

dynamically control them with an electric field. Thus, the effect of oxygen vacancy on the MITs of $RNiO_3$ and their potential applications in various electronic devices are investigated in this study. For better comparison with previous results reported in the literature, $NdNiO_3$ is chosen as the representing $RNiO_3$. Two methods, post-deposition vacuum annealing and adjusting oxygen pressure during film deposition are used to control the oxygen vacancies in $NdNiO_3$ thin films. By introducing oxygen vacancies, an insulating phase is stabilized at room temperature with a resistance modulation of ~10^6. Similar results have been obtained with samples deposited under different oxygen pressure. Detailed characterizations on the carrier density and T_{MI} have been carried out, and a model is proposed to describe the oxygen vacancy induced insulating phase in $NdNiO_3$, which should be applicable to other $RNiO_3$ thin films as well.

4.2 Results and Discussion

4.2.1 Oxygen vacancies introduced by post-deposition vacuum annealing

4.2.1.1 Sample preparation and structural characterizations

$NdNiO_3$ thin films were deposited on (001)-oriented single-crystal $SrTiO_3$ and 0.5 wt% Nb-doped $SrTiO_3$ (Nb-$SrTiO_3$) substrates by PLD. The laser pulse (248 nm) energy density was ~2 J/cm^{-2} and the repetition rate was 5 Hz. During the deposition, the substrate temperature and chamber oxygen pressure were kept at 675 ºC and 40 Pa, respectively. After deposition, the oxygen pressure was increased to 10^4 Pa, and the sample was cooled to room temperature. For subsequent vacuum annealing study, the as-grown samples were placed in a chamber and the background pressure during vacuum annealing was 10^{-4} pa. The annealing temperature was varied from 180 ºC to 300 ºC to modulate the amount of oxygen vacancy introduced. The annealing time was fixed at 20 mins. To return the samples to the as-grown state, annealing under oxygen pressure of 10^4 Pa for 20 mins at 300 ºC was conducted.

Figure 4.1 shows the surface morphology of a set of $NdNiO_3$ films measured by AFM after annealing under vacuum. The vacuum annealing temperature is from 180 ºC to 300 ºC and the corresponding AFM pictures are all very smooth with small roughness (less than 0.5 nm), indicating that the vacuum annealing process doesn't damage the samples.

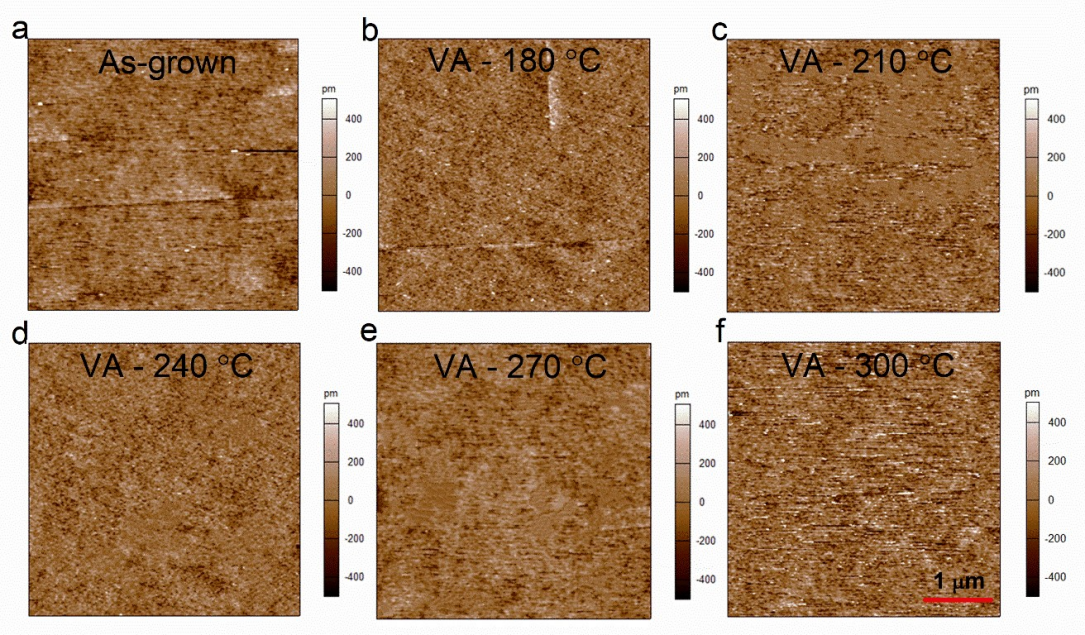

Figure 4.1 Topography images of $NdNiO_3$ thin films after being annealed under different temperatures show very smooth surface with pm roughness. VA denotes vacuum annealing.

HR-XRD measurements were carried before and after the vacuum annealing to investigate the structure of the samples. As shown in Figure 4.2, only $NdNiO_3$ (002) and $SrTiO_3$ (002) diffraction peaks are observed, suggesting epitaxial growth of the films. As the vacuum annealing temperature is increased from 180 to 300 ºC, an obvious shift of the $NdNiO_3$ (002) diffraction peak is observed, indicating a significant enlargement of the *c*-axis lattice constant. Following Bragg's law, the *c*-axis lattice constant is calculated to be 3.794 Å for as-grown samples and 3.808 Å for samples after vacuum annealing at 300 ºC, showing an increment of 0.37%. Interestingly, the *c*-axis lattice constant can be fully restored to the as-grown value if the samples are annealed under high oxygen pressure (10^4 Pa) at 300 ºC only, as indicated by the diffraction peak labeled as OA-300 ºC in Figure 4.2. This suggests that the introduction and annihilation of oxygen vacancies via vacuum/oxygen annealing are completely reversible.

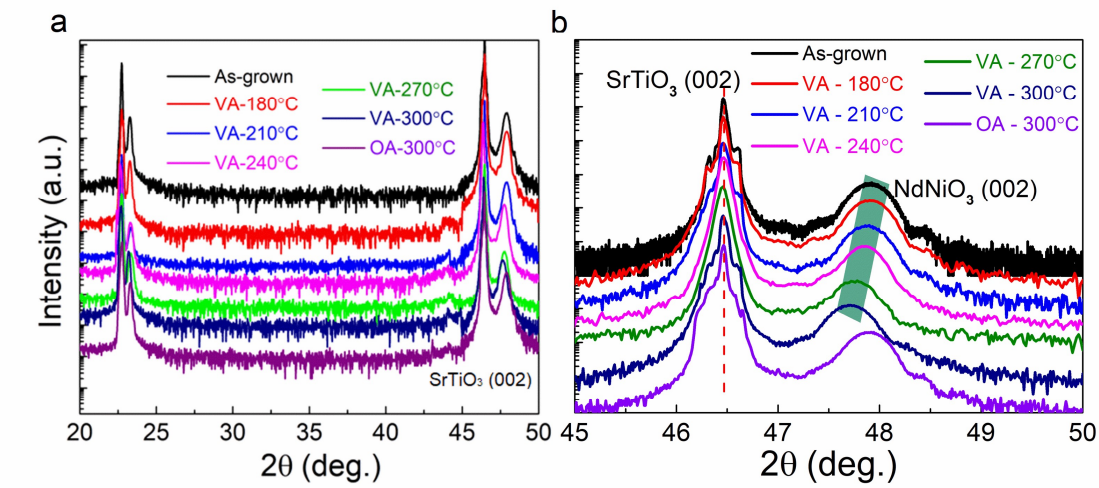

Figure 4.2 HR-XRD patterns around the $SrTiO_3$ (002) peaks of a 40 nm $NdNiO_3$ thin film before and after being annealed at different temperatures in vacuum and oxygen environment. VA and OV represent vacuum annealing and oxygen annealing, respectively.

4.2.1.2 Electrical properties of the vacuum annealed $NdNiO_3$ films

The electrical properties of $NdNiO_3$ thin films with thickness from 5 to 120 nm have been tested using PPMS. All samples undergo an MIT as shown in Figure 4.3. As thickness decreases, the phase transition temperature, T_{MI}, also decreases. However, it has been reported that there is a critical thickness (~8 nm) for $NdNiO_3$ films on $SrTiO_3$ substrates, below which the T_{MI} will increase with decreasing thickness due to the dimensional crossover, as demonstrated in Figure 4.3.[13]

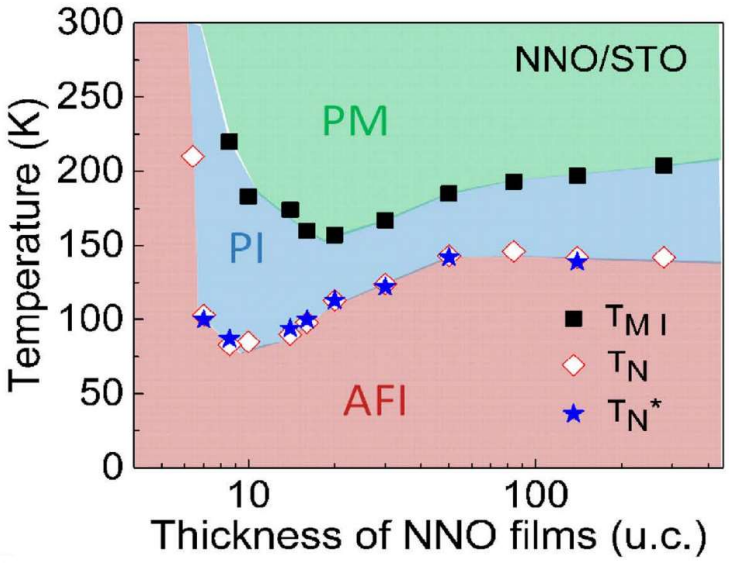

Figure 4.3 Phase evolution as a function of the film thickness for $NdNiO_3/SrTiO_3$ system. PM, PI, and AFI denote paramagnetic metal, paramagnetic insulator and antiferromagnetic insulator, respectively. T_N and T_N* denote magnetic phase transition temperatures, which are extracted from electrical resistivity and magnetoresistance measurements, respectively. The phase diagram can clearly be separated into two regions, below and above a critical thickness of ~20 u.c. Reprinted with permission.[13] Copyright 2018, Nature Publishing Group.

What happens is that, in $NdNiO_3$ films, both strain from substrate and lattice confinement (thickness) affect the transport behavior. Above the critical thickness, the T_{MI} is mainly controlled by strain through changing the Ni-O-Ni bond angle. Below the critical thickness, however, the reduced lattice dimensionality stabilizes the insulating phase and increases the T_{MI}. To avoid this region, we have chosen films of 40 nm for the subsequent analysis, though in most cases, films of 5 to 120 nm have been tested.

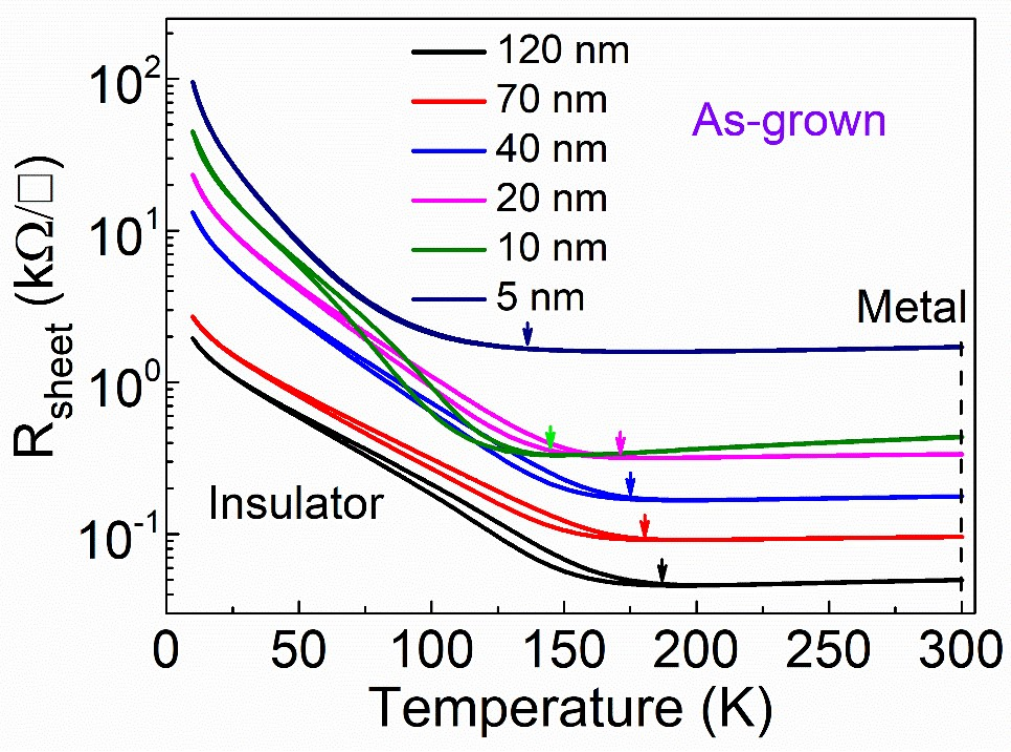

Figure 4.4 In-plane transport behaviors of as-grown $NdNiO_3$ thin films with thickness ranging from 5 to 120 nm. T_{MI} gradually decreases upon reducing film thickness until the critical thickness.

The overall sheet resistance (R_{sheet}) increases as thickness decreases, which is partly attributed to the definition of R_{sheet}. R_{sheet} equals to ρ/t, where ρ is electrical resistivity and t is film thickness. All as-grown $NdNiO_3$ films show metallic behavior at room temperature (300 K), which is consistent with the large carrier density (~10^{22} cm^{-3}). Upon vacuum annealing at 300 ℃, the R_{sheet} of a 40 nm-thick $NdNiO_3$ thin film is increased from ~0.1 kΩ/□ to ~10^5 kΩ/□, a six order of magnitude increase. The temperature dependent transport behavior also suggests insulating behavior after vacuum annealing. The inset of Figure 4.5a shows that the color of the sample changes from black to semi-transparent after annealing, confirming that an optical bandgap is opened by the vacuum annealing process. The detailed investigation of optical properties will be presented in Chapter 5. Samples with different thicknesses all share the similar resistance modulation behavior as shown in Figure 4.5b. For the thinnest $NdNiO_3$ films (~5 nm), the room temperature R_{sheet} increases by 10^6 times from an as-grown of only 180 ℃. Further

increase of the annealing temperature does not increase R_{sheet} further and it instead gradually saturates. For thicker samples, higher temperature is needed to reach the saturation of R_{sheet} and the ratio between the highest and lowest R_{sheet} values is also smaller than that of the thinner samples. After oxygen annealing at 300 °C, the sheet resistances of all $NdNiO_3$ films revert back to the as-grown metallic state values, as shown by the green dots in Figure 4.5b, which match the as grown results (black squares) perfectly.

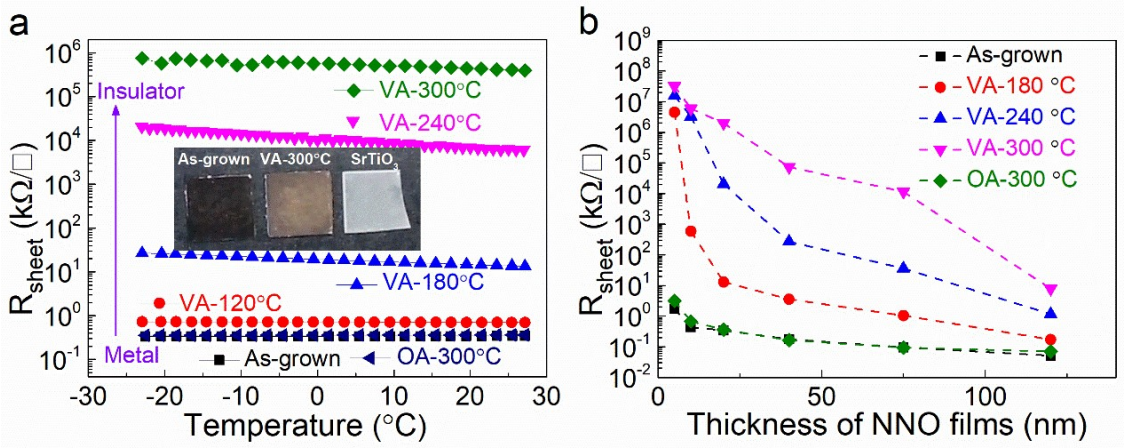

Figure 4.5 (a) Sheet resistance, R_{sheet}, of a 40 nm $NdNiO_3$ film as functions of temperature after vacuum and oxygen annealing treatments. The inset shows the pictures of the sample before and after annealing. (b) Summary of changes in R_{sheet} after vacuum and oxygen annealing for films with different thicknesses. VA and OA denote vacuum annealing and oxygen annealing respectively.

To quantify the effect of vacuum annealing on carrier density in $NdNiO_3$, we conducted Hall measurements and the representative results for a 40 nm film before and after vacuum annealing at 180 °C is shown in Figure 4.6. Inset of Figure 4.6a shows the measurement setup, in which the Hall bar structure is prepared by standard lithography and etching process. The length and width of the hall bar are 550 and 50 μm, respectively. The Hall coefficient (R_H), *c*-axis lattice constant, R_{sheet} and majority carrier concentrations of the same sample after being annealed in vacuum at different temperatures are summarized in Figure 4.5b. The Hall coefficient of the as-grown film is 1.75×10^{-4} cm^3/C, suggesting that as-grown $NdNiO_3$ films are *p*-type. Following

$$p^* = \frac{1}{eR_H},$$

where p^* and e represent hole concentration and the electron charge, respectively, effective p^* of 3.56×10^{22} cm^{-3} is obtained for the as-grown film, which is consistent with previous reports.[2, 14] By increasing the vacuum annealing temperature, R_H, R_{sheet} and c-axis lattice constant all increase while the carrier concentration decreases by three orders of magnitude from ~10^{22} to ~10^{19} cm^{-3}, which explains the large change in sample resistance as discussed in the previous section.

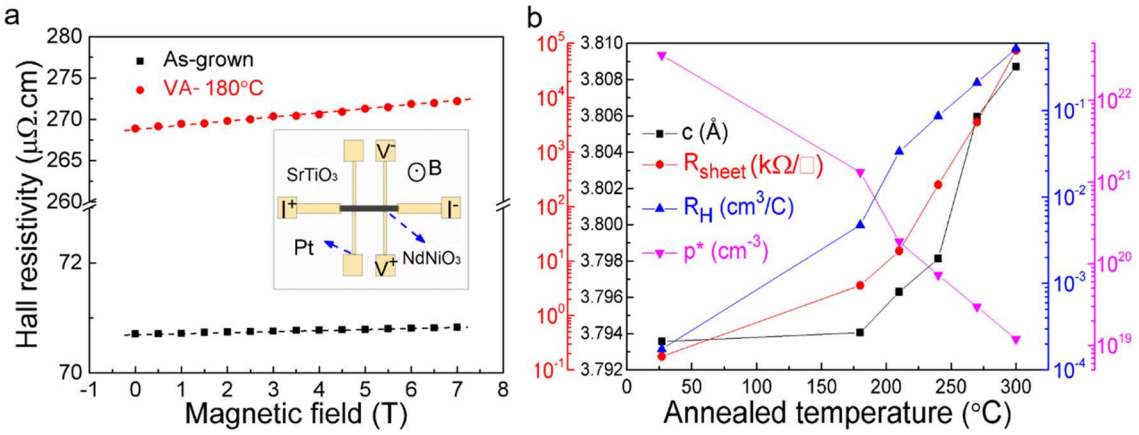

Figure 4.6 (a) Room temperature Hall resistivity (ρ) versus magnetic field for a 40 nm $NdNiO_3$ film. The inset shows the Hall bar architecture, where B represent the magnetic field. (b) Room temperature R_{sheet}, R_H, p^* and c-axis lattice constant as functions of vacuum annealing temperature. R_H is the slope of the plot in (a) and follows the formula $R_H = (\rho_{(7T)} - \rho_{(0T)})/7T$, where T (tesla) is the unit of magnetic field.

Change in carrier concentration induced by oxygen vacancies may account for the increased resistance of $NdNiO_3$ films after vacuum annealing. However, it doesn't explain the opening of a bandgap.

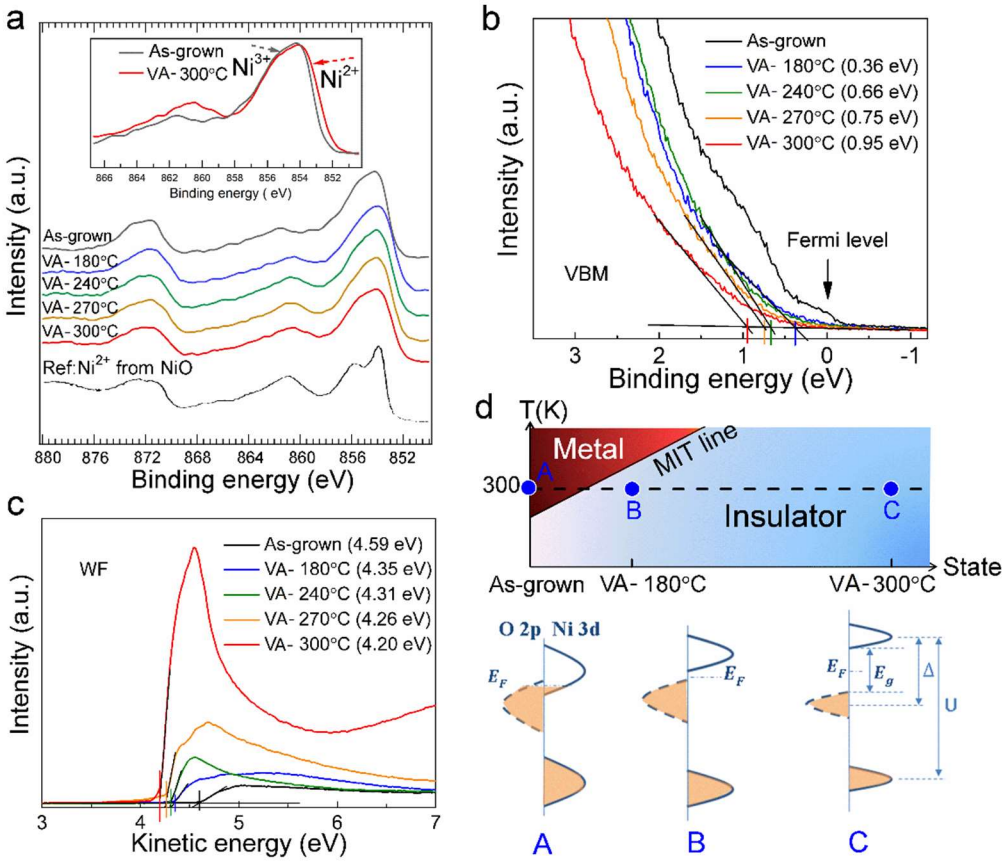

Figure 4.7 (a) Ni 2p XPS spectra of as-grown and vacuum annealed 40 nm-thick $NdNiO_3$ films. The inset shows an enlargement for Ni 2p XPS of as-grown sample and that of sample vacuum annealed under 300°C, which indicates an increase in Ni^{2+} fraction after vacuum annealing process. Valence band maximum (VBM) (b) and work function (W_F) (c) determined from the secondary electron onset in UPS measurements. (d) Schematic phase diagram of $NdNiO_3$ film undergoing a room temperature metal-insulator transition due to oxygen vacancy. Schematic energy band diagrams for three different states are shown below the phase diagram. Here, Δ denotes the charge transfer energy, U is d-d Coulomb repulsion energy, E_F is the Fermi level and Eg is the bandgap.

To better understand the effect of oxygen vacancies, XPS and UPS measurements were conducted. From Ni 2p XPS (Figure 4.7a), the spectral line shapes of vacuum annealed samples indicate the gradual $Ni^{3+} \rightarrow Ni^{2+}$ valence change.[15] The peak of Ni 2p3/2 at 853.9 eV reflects the dominance of Ni^{2+} in $NdNiO_3$ film vacuum annealed at 300 °C. (the

inset of Figure 4.7a).[16] Figure 4.7b shows the valance band spectra weight of the $NdNiO_3$ films obtained by UPS measurements. The valance band maximum (VBM) is determined by linear extrapolation of valance band onset.[17] For the vacuum annealed $NdNiO_3$ films, VBM shifts from ~0.36 eV to ~0.95 eV below E_F. Figure 4.7c also reveals that the work function (W_F) decreases with increasing vacuum annealing temperature, consistent with oxygen vacancies being donor dopants. Combining the transport measurements and XPS/UPS results, the phase evolution of $NdNiO_3$ films upon vacuum annealing is presented in Figure 4.7d. For the as-grown $NdNiO_3$ films, the room temperature metallic behavior arises from the overlap of occupied O 2p and unoccupied Ni 3d bands. Upon vacuum annealing, oxygen vacancies are introduced and the Ni^{2+}/Ni^{3+} ratio gradually increases. Both valence and conduction bandwidths will be reduced due to the larger Ni^{2+} ionic radius and Ni-O bond length (d_{Ni-O}).[18] The larger d_{Ni-O} can also lead to the smaller Ni-O-Ni bond angle because the tolerance factor is reduced, further reducing the bandwidths. The narrowed bandwidths further lead to stronger Coulomb repulsion between the electrons (the intra-atomic d-d Coulomb repulsion energy U increases) and induce a large Mott–Hubbard splitting.[19] Both effects contribute to bandgap opening and room temperature insulating phase is induced, as shown schematically in Figure 4.7d. This process is continuously tunable and reversible. Annealing the film in oxygen recovers the metallic behavior.

4.2.2 Adjusting oxygen pressure during film deposition

4.2.2.1 Sample preparation and structural characterizations

Besides annealing the as-grown films in vacuum, one can also adjust the oxygen partial pressure during film growth by PLD to introduce oxygen vacancies in oxide films. In this case, the $NdNiO_3$ thin films were deposited on (001)-oriented single-crystal $SrTiO_3$. The laser pulse (248 nm) energy density was ~2 J/cm^{-2} and the repetition rate was 5 Hz. The substrate temperature was kept at 675 ºC. The oxygen partial pressure during deposition was varied from 200 to 0.02 mTorr to introduce oxygen vacancies into the $NdNiO_3$ thin

films. After deposition, the oxygen pressure was kept unchanged while the film was cooled to room temperature.

The surface morphologies of $NdNiO_3$ thin films prepared under different oxygen pressures ($P(O_2)$) are shown in Figure 4.8. As $P(O_2)$ decreases from 200 to 0.02 mtorr, no obvious difference can be observed from the surface. The roughness increases slightly from 0.16 nm to 0.37 nm. But all samples show flat surface with roughness less than 0.50 nm, indicating good quality of these films.

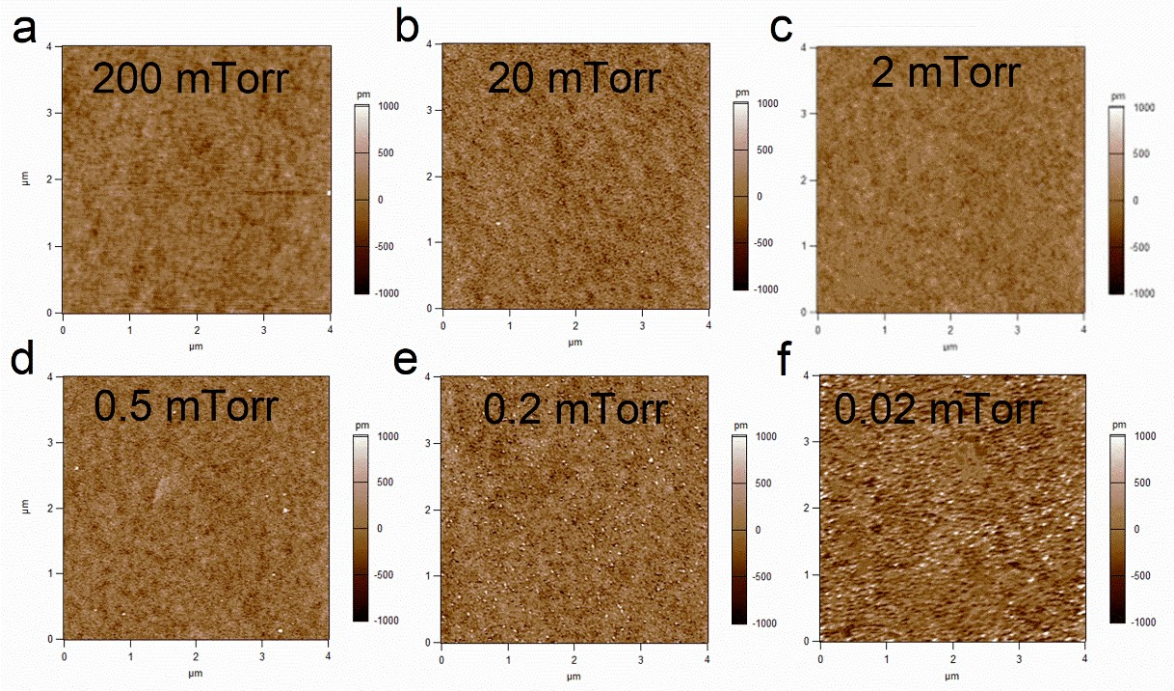

Figure 4.8 Topography images of 45 nm $NdNiO_3$ thin films prepared under different oxygen pressure on (001)-oriented $SrTiO_3$ substrates. All samples show smooth surface with sub-nm level roughness.

Figure 4.9 shows the HR-XRD patterns of these samples. The (002) diffraction peaks of $NdNiO_3$ shifts gradually to the left with decreasing $P(O_2)$, indicating the increase of *c*-axis lattice constant. This is consistent with the observation reported in Section 4.2.1 that vacuum annealing of $NdNiO_3$ films leads to the increase of *c*-axis lattice constant. Decreasing $P(O_2)$ or vacuum annealing both generate oxygen vacancies in the films.

However, decreasing $P(O_2)$ during film deposition seems much more effective. As shown in Figure 4.9, the (002) diffraction peak changes from ~48.0 to 45.2 degree (lattice constant changes from 3.79 to 3.96 Å) while vacuum annealing induced peak shift is much smaller. This difference can be understood since vacuum annealing was conducted at temperatures much lower than film deposition temperature, so the amount of oxygen vacancies introduced would be less. Furthermore, migration of oxygen ions during vacuum annealing also takes time. On the other hand, oxygen vacancies are readily introduced throughout the film during the deposition under low $P(O_2)$. For subsequent studies, we thus choose films deposited under low $P(O_2)$.

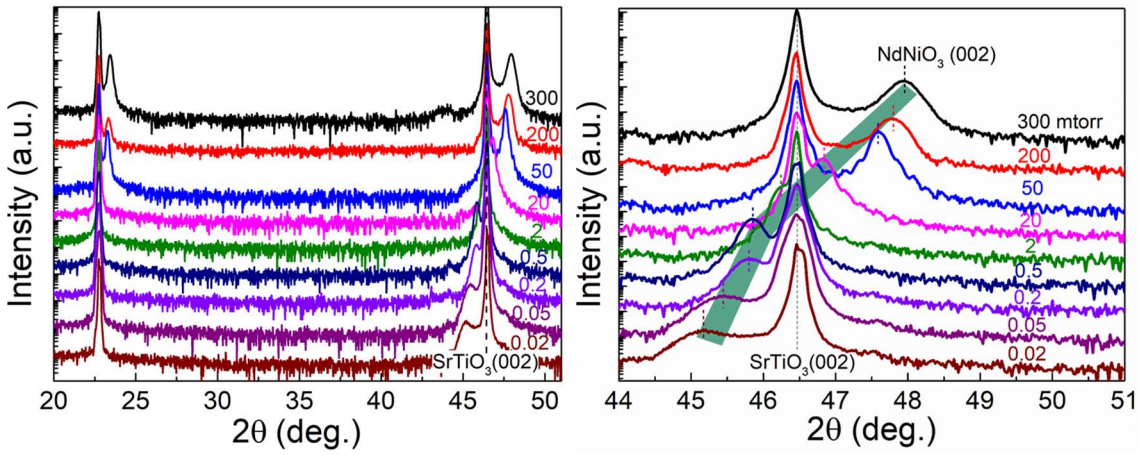

Figure 4.9 HR-XRD theta-2theta scans of 45 nm $NdNiO_3$ films prepared under different $P(O_2)$. The zoom in pattern around $SrTiO_3$ (002) shows the (002) peak shift due to oxygen vacancies introduced.

4.2.2.2 Electrical properties of $NdNiO_3$ films deposited under different oxygen pressures

To confirm that oxygen vacancies introduced during film deposition have similar effect on the electrical properties of the $NdNiO_3$, we measure the in-pane transport behaviors of the films prepared under different $P(O_2)$ and the results are shown in Figure 4.9a. A clear MIT is observed for the sample deposited under 300 mTorr $P(O_2)$, and the T_{MI} is ~ 205 K, which is close to the value of bulk $NdNiO_3$.[20] For all other films grown at lower $P(O_2)$,

insulating behavior dominates over the whole temperature range. R_{sheet} at room temperature gradually increases with decreasing $P(O_2)$ as shown in Figure 4.10b because oxygen vacancies donate electron to neutralize the holes in the p-type $NdNiO_3$ films. Furthermore, oxygen vacancies, which reduce Ni^{3+} to Ni^{2+}, also result in larger *c*-axis lattice constant. These observations are essentially the same as that described in Section 4.2.1.

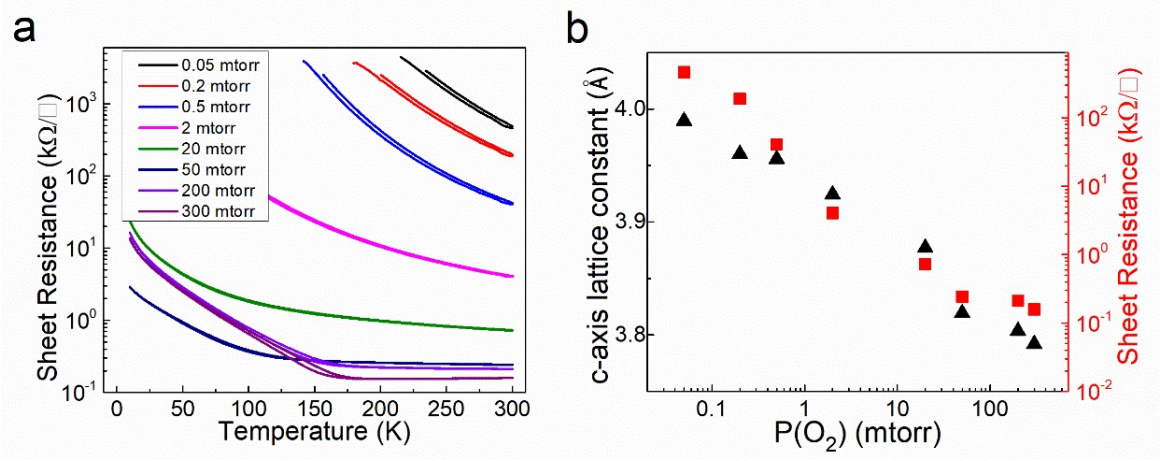

Figure 4.10 (a) Temperature dependence of R_{sheet} of $NdNiO_3$ films deposited under different oxygen pressure (The R_{sheet} of $NdNiO_3$ films grown under 0.02 mTorr exceeds the range of the PPMS). (b) *c*-axis lattice constant and R_{sheet} of $NdNiO_3$ films as a function of $P(O_2)$ at 300 K. All the films are 45 nm thick.

4.3 Conclusions

In summary, the band structure of $NdNiO_3$ thin films have been engineered by oxygen vacancies. By vacuum annealing process, a resistance modulation of ~10^6 has been achieved at room temperature. The Hall effect measurements provide evidence for the p-type nature of both as-grown and annealed $NdNiO_3$ thin films. With the aid of XPS, the fraction of Ni^{2+} has been proved to increase after annealing. The UPS results suggest a shifting up of E_F, which is consistent with the change of R_H. Oxygen vacancy, acting as electron donor, changes Ni^{3+} to Ni^{2+}. The enlarged Ni^{2+} ion radius increases the Ni-O bond length and narrows the bandwidth. Finally, a bandgap is opened between the Ni 3d and O 2p orbitals. The band engineering of the $RNiO_3$ is tunable and reversible. By

means of adjusting the oxygen pressure during thin film growth, the MIT is also proven to be effectively tuned. The band engineering of $RNiO_3$ thin films suggest potential applications such as photovoltaic cells, photodetectors and non-volatile memories, which will be discussed in details in the following chapters.

References

[1] J. García-Muñoz, M. Suaaidi, M. Martínez-Lope, and J. Alonso. *Phys. Rev. B* **1995**, 52, 13563.

[2] R. Scherwitzl, P. Zubko, I. G. Lezama, S. Ono, A. F. Morpurgo, G. Catalan, and J. M. Triscone. *Adv. Mater.* **2010**, 22, 5517-5520.

[3] J. Liu, M. Kargarian, M. Kareev, B. Gray, P. J. Ryan, A. Cruz, N. Tahir, Y.-D. Chuang, J. Guo, and J. M. Rondinelli. *Nat. Commun.* **2013**, 4, 2714.

[4] E. Breckenfeld, Z. Chen, A. R. Damodaran, and L. W. Martin, *ACS Appl. Mater. & Interfaces* **2014**, 6, 22436-22444.

[5] H. Y. Hwang. *Nat. Mater.* **2005**, 4, 803.

[6] Y.-M. Kim, J. He, M. D. Biegalski, H. Ambaye, V. Lauter, H. M. Christen, S. T. Pantelides, S. J. Pennycook, S. V. Kalinin, and A. Y. Borisevich. *Nat. Mater.* **2012**, 11, 888.

[7] J. Jeong, N. Aetukuri, T. Graf, T. D. Schladt, M. G. Samant, and S. S. Parkin. *Science* **2013**, 339, 1402-1405.

[8] B. Wang, L. You, P. Ren, X. Yin, Y. Peng, B. Xia, L. Wang, X. Yu, S. M. Poh, and P. Yang. *Nat. Commun.* **2013**, 4, 2778.

[9] Z. T. Xu, K. J. Jin, L. Gu, Y. L. Jin, C. Ge, C. Wang, H. Z. Guo, H. B. Lu, R. Q. Zhao, and G. Z. Yang. *Small* **2012**, 8, 1279-1284.

[10] W. Li, R. Zhao, L. Wang, R. Tang, Y. Zhu, J. H. Lee, H. Cao, T. Cai, H. Guo, and C. Wang. *Sci. Rep.* **2013**, 3, 2618.

[11] R. Zhao, K. Jin, Z. Xu, H. Guo, L. Wang, C. Ge, H. Lu, and G. Yang. *Appl. Phys. Lett.* **2013**, 102, 122402.

[12] L. Wang, T. Maxisch, and G. Ceder. *Phys. Rev. B* **2006**, 73, 195107.

[13] L. Wang, S. Ju, L. You, Y. Qi, Y.-w. Guo, P. Ren, Y. Zhou, and J. Wang, *Sci. Rep.* **2015**, 5, 18707.

[14] A. J. Hauser, E. Mikheev, N. E. Moreno, T. A. Cain, J. Hwang, J. Y. Zhang, and S. Stemmer. *Appl. Phys. Lett.* **2013**, 103, 182105.

[15] A. Carley, S. Jackson, J. O'shea, and M. Roberts. *Surf. Sci.* **1999**, 440, L868-L874.

[16] J. F. Moulder, W. F. Stickle, P. E. Sobol, and K. D. Bomben. *Phys. Electron.* **1995**, 261.

[17] S. Chen, T. W. Goh, D. Sabba, J. Chua, N. Mathews, C. H. A. Huan, and T. C. Sum. *APL Mater.* **2014**, 2, 081512.

[18] M. Medarde, P. Lacorre, K. Conder, F. Fauth, and A. Furrer. *Phys. Rev. Lett.* **1998**, 80, 2397.

[19] C. Schlenker, J. Dumas, M. Greenblatt, and S. van Smaalen, *Physics and Chemistry of Low-Dimensional Inorganic Conductors* **2012**, Springer Science & Business Media.

[20] J. Torrance, P. Lacorre, A. Nazzal, E. Ansaldo, and C. Niedermayer. *Phys. Rev. B* **1992**, 45, 8209.

Chapter 5

Optimizing the Nickelates Heterojunctions by Band Engineering for Photovoltaic Cells

In this chapter, a systematic investigation on the photovoltaic performances of $RNiO_3$/Nb-$SrTiO_3$ heterojunctions is conducted by rare-earth element substitution and oxygen vacancy controlling. The metal-insulator transition in $NdNiO_3$ thin film is successfully tuned by directly adjusting oxygen pressure during film growth. The optical bandgaps of these samples at room temperature increase as the oxygen pressure decreases. Photovoltaic performance has been optimized by oxygen pressure and thickness control. Based on the results from $RNiO_3$/Nb-$SrTiO_3$, different $RNiO_3$/Nb-$SrTiO_3$ heterojunctions are investigated. Rare earth element and oxygen pressure dependence of power conversion efficiency are obtained. Finally, a p-i-n structure is introduced to enlarge the depletion area, which results in an ultimate power conversion efficiency of 1.1 %.

5.1 Introduction

Perovskite nickelates ($RNiO_3$) undergo MIT and their band structures can be reversibly tuned by controlling oxygen vacancies in them. As discussed in Chapter 4, both post-deposition vacuum annealing and oxygen pressure control during deposition are effective in introducing oxygen vacancies into $NdNiO_3$ thin films. Since oxygen vacancies act as electron donors, the Fermi level will be increased. At the same time, oxygen vacancies also change the lattice constant and the Ni-O-Ni bond angle, which reduces the bandwidth, leading to the opening of a bandgap. Thus, an insulating phase can be stabilized at room temperature. However, vacuum annealing is time-consuming, and it leads to the drawback of thickness dependent for migration of oxygen vacancies. On the other hand, controlling the oxygen pressure during the film deposition introduces oxygen vacancies into the film much more effectively and uniformly. This is confirmed by the much larger changes in lattice constant as presented in Chapter 4. Thus, this method is adopted for subsequent studies. Furthermore, effects of oxygen vacancies on the electric properties are expected to be universal to all $RNiO_3$ films, which will be discussed in this chapter.

Photovoltaic (PV) is the process of converting photon energy into electricity.[1] The market for PV modules has grown exponentially in the past 20 years. However, despite the fast growth of the industry, the cost of producing electricity by PV process is still higher than that by conventional methods such as burning fossil fuels. Further reduction in cost is necessary, which requires novel and cheap light absorbing materials and low-cost deposition methods. One of the most interesting topics in the field recently is the hybrid perovskite light absorbers such as $CH_3NH_3PbI_3$.[2-6]. Hybrid perovskites-based solar cells has obtained an efficiency of more than 20% within only a few years. Anomalously long lifetime and diffusion length of photo-carriers have been observed in these materials, despite the high concentration of defects in them.[7-10] However, the stability and toxicity issues of hybrid perovskites cast shadows on their practical applications. By comparison, perovskite oxides are chemically and physically stable with tunable bandgaps to suit varieties of applications.[11]

Motivated by these facts, the idea of tuning the bandgaps of $RNiO_3$ thin films for PV application is established. In this chapter, heterojunctions of $RNiO_3$/Nb-$SrTiO_3$ have been fabricated to investigate the PV performance. The MIT of $RNiO_3$ thin films prepared under different oxygen pressures ($P(O_2)$) was investigated. The band structures of as-grown $RNiO_3$ thin films were continuously tuned not only by controlling the oxygen partial pressures but also by rare-earth element. With the aid of an ultrathin insulating layer between the $RNiO_3$/Nb-$SrTiO_3$ heterojunction, the ultimate power conversion efficiency (PCE) reaches 1.1%. This study may promote the applications of $RNiO_3$ in photovoltaics.

5.2 Results and Discussion

5.2.1 Sample preparation and structural characterizations

$NdNiO_3$, $SmNiO_3$, $GdNiO_3$ and $LuNiO_3$ thin films were deposited on (001) oriented single-crystal $SrTiO_3$ and 0.5 wt% Nb-$SrTiO_3$ substrates by PLD. The substrate temperature was kept at 675 ºC. The oxygen partial pressure during deposition was varied from 200 to 0.02 mTorr as needed. The laser pulse (248nm) energy density was ~2 J/cm^{-2} and the repetition rate was 5 Hz. After deposition, the oxygen pressure was kept unchanged. An array of Au electrodes was deposited by PLD onto the surface of $RNiO_3$ thin films to perform PV test. The thickness and size of Au electrodes are 10 nm and 400×400 μm^2. The light source during PV test is a Xeon lamp with power density of 150 mW/cm^2.

The structure and electrical transport information of such $NdNiO_3$ films have been presented in Section 4.2.2.

5.2.2 Optical absorption spectrum

The absorption spectra of $NdNiO_3$ films grown under different $P(O_2)$ is shown in Figure 5.1a. Figure 5.1b presents the Tauc plots derived from the spectra. The inset of 5.1b

shows the pictures of $NdNiO_3$ films deposited on double-side polished (001) oriented $SrTiO_3$ substrates. Linear fitting of the Tauc plots reveals the bandgap.[12] Although such fitting cannot be used to determine the precise value of the bandgap, the trend that it increases when $P(O_2)$ decreases is with certainty. This is consistent with the sample color change as shown in the inset of Figure 5.1b. As $P(O_2)$ decreases, the transparency of the samples increases, indicating the opening of an optical bandgap.

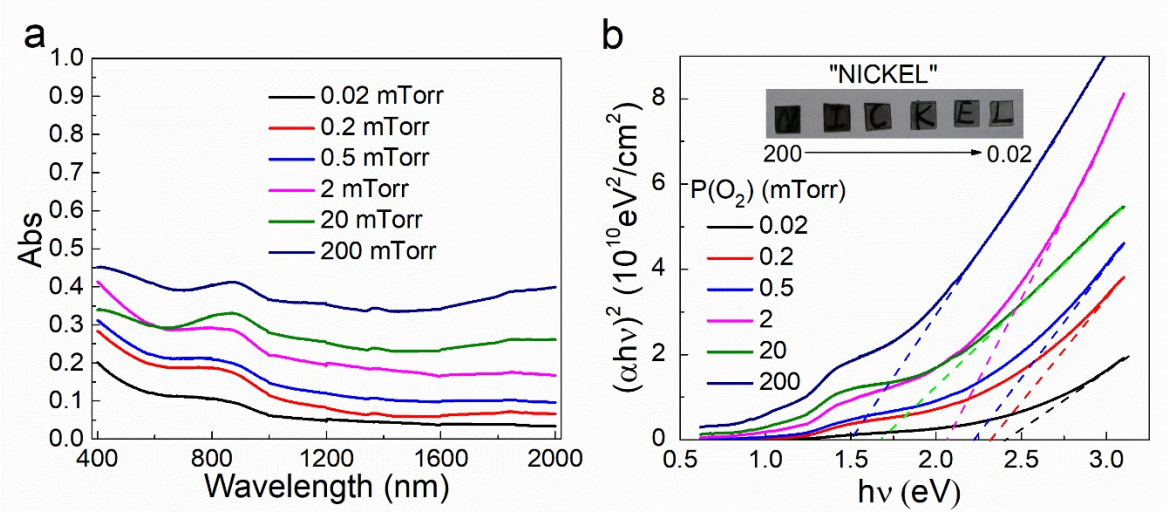

Figure 5.1 (a) UV–Vis absorption spectra of 45 nm-thick $NdNiO_3$ films grown under different $P(O_2)$. (b) Tauc plots derived from optical absorption spectra. The inset shows the pictures of these $NdNiO_3$ films grown on double-polished transparent substrates.

5.2.3 PV performance of $NdNiO_3$/Nb-$SrTiO_3$ heterostructures

PV measurements were performed on Au/$NdNiO_3$/Nb-$SrTiO_3$ heterojunctions. The current density (J) versus voltage (V) curves measured in dark are showed in Figure 5.2a. Because of the p-type nature of $NdNiO_3$ and n-type nature of Nb-$SrTiO_3$ substrates, the J-V curves show rectifying characteristics. Note that the contact between Au and $NdNiO_3$ films is ohmic. As $P(O_2)$ decreases from 200 to 0.02mTorr, diode behavior starts to appear when $P(O_2)$ reaches 2 mtorr. For an ideal abrupt pn junction, the capacitance (C) follows

$$\frac{1}{c^2} \propto V_{bi} + V,$$

where V_{bi} is the build-in voltage and V is the reverse bias voltage. [13] So, the V_{bi} can be easily derived from the C-V plots. As show in Figure 5.2b, the linear fitting of C-V plots intercept with x-axis, indicating the decrease of V_{bi} with decreasing P(O_2). This can be explained by the oxygen vacancies induced increase of E_F. V_{bi} plays an important role in the PV process as it is the driving force to separate the photon-generated carriers. However, large V_{bi} doesn't necessarily mean better PV performance since short circuit current is also important, as shown in Figure 5.2. J-V curves of the heterojunctions measured under illumination is presented in Figure 5.2c and the corresponding short circuit current density (J_{SC}) and open circuit voltage (V_{OC}) are summarized in Figure 5.2d. J_{SC} and V_{OC} show similar trends as P(O_2) change, leading to a maximum PCE at ~0.2%.

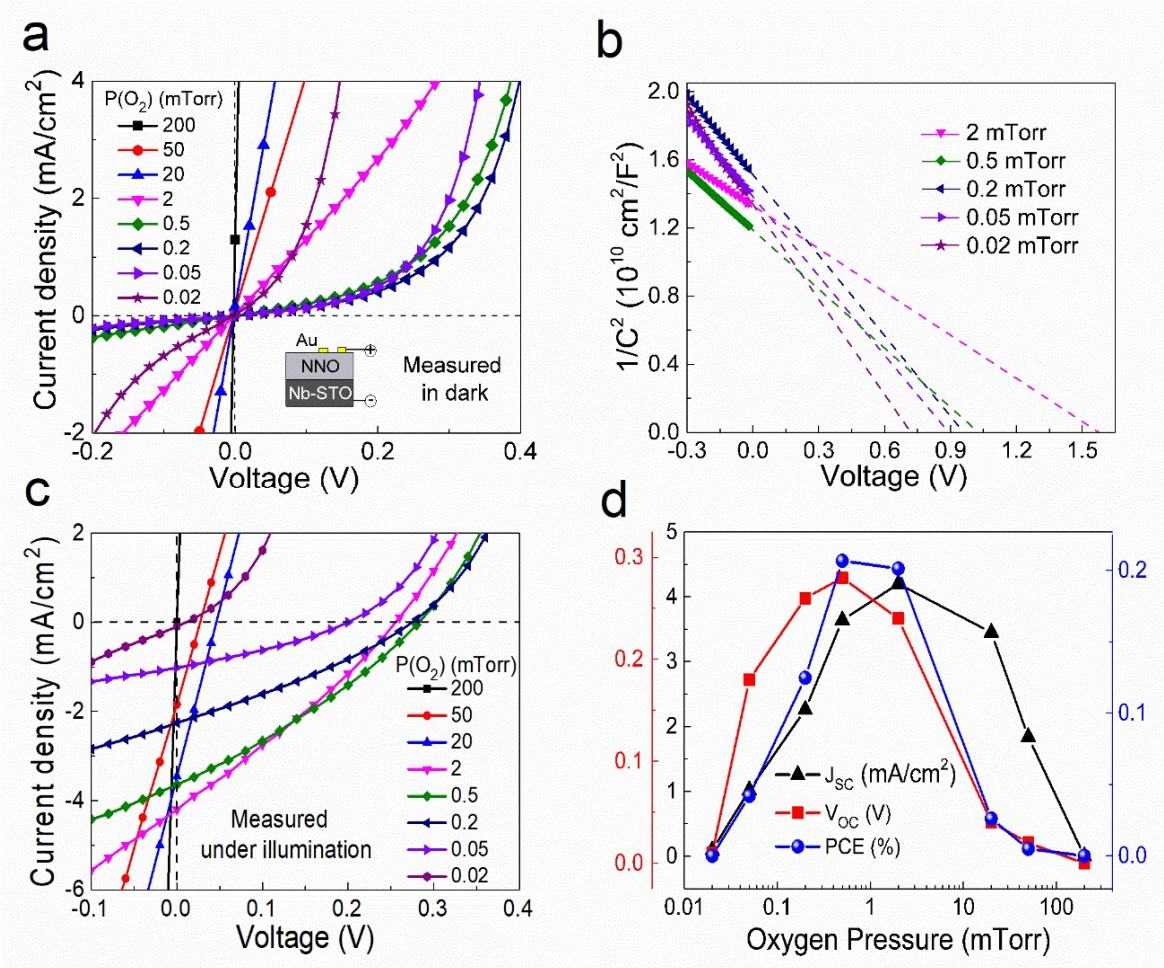

Figure 5.2 (a) J-V curves of Au/$NdNiO_3$/Nb-$SrTiO_3$ heterojunctions measured in dark. The inset shows the schematic device structure. (b) Plots of $1/C^2$ versus voltage of these heterojunctions. The dashed lines are the linear fittings of the plots, whose intercept with x-axis

indicates the values of V_{bi}. (c) *J-V* curves of the same heterojunctions measured under illumination. (d) $P(O_2)$ dependence of J_{SC}, V_{OC} and power conversion efficiency (PCE). PCE is defined as PCE = $V_{OC} \times J_{SC} \times FF/P_{in}$, where FF is the filling factor, P_{in} is the input power density of a Xeon lamp. (150 mW/cm^{-2})

The specific values of these PV parameters are listed in Table 5.1. Samples prepared under high $P(O_2)$ absorb more light because their bandgaps are relatively low. However, because of the small V_{bi}, which can hardly separate the photo-generated electrons and holes, the performance is not good. As $P(O_2)$ decreases (less than 50 mTorr), rectifying characteristic starts to be improved, which decreases the recombination of photo-generated carriers, leading to higher J_{SC} and V_{OC}. But the bandgap will dominate the performance as $P(O_2)$ continue to decrease because it is too large for light absorption. This results in the drop of J_{SC} and V_{OC}.

Table 5.1 Photovoltaic performance of different Au/$NdNiO_3$/Nb-$SrTiO_3$ devices. FF is the filling factor. I_0 is the leakage current when bias is 0 V in dark.

P (O_2) (mTorr)	V_{bi} (V)	I_0 (A)	V_{OC} (V)	J_{SC} (mA cm^{-2})	FF (%)	PCE (%)
200	—	$2.0 * 10^{-6}$	0	0	0	0
50	—	$2.1 * 10^{-6}$	0.02	1.84	20.00	0.005
20	—	$2.5 * 10^{-7}$	0.04	3.45	28.26	0.026
2	1.56	$4.4 * 10^{-8}$	0.24	4.20	29.95	0.201
0.5	1.02	$2.6 * 10^{-9}$	0.28	3.64	30.44	0.207
0.2	0.96	$2.4 * 10^{-10}$	0.26	2.26	31.88	0.125
0.05	0.88	$8.2 * 10^{-10}$	0.18	1.02	34.36	0.042
0.02	0.71	$2.7 * 10^{-8}$	0.01	0.095	0	0

Note that all the results are obtained from Au/$NdNiO_3$/Nb-$SrTiO_3$ heterojunctions where the thickness of $NdNiO_3$ is fixed at 45 nm. As it has been found that the maximum PCE

appears when $P(O_2)$ is 0.5 mTorr, thickness dependence of PV performances is investigated as in Figure 5.3. Similar thickness dependences were reported for other systems.[14-16] An critical thickness, which corresponds to the thickness of depletion layer, is used to explain the phenomenon. In the case of $NdNiO_3$/Nb-$SrTiO_3$, the critical thickness is ~30 nm as indicated in Figure 5.3b. If the thickness is less than 30 nm, V_{OC} decreases due to smaller depletion region and weakening of the built-in electric field. While it is larger than 30 nm, further increase in film thickness increases the recombination of photo-generated carriers. If the contribution of more absorption from thicker films cannot compensate for the loss due to recombination, J_{SC} and V_{OC} decrease.[17]

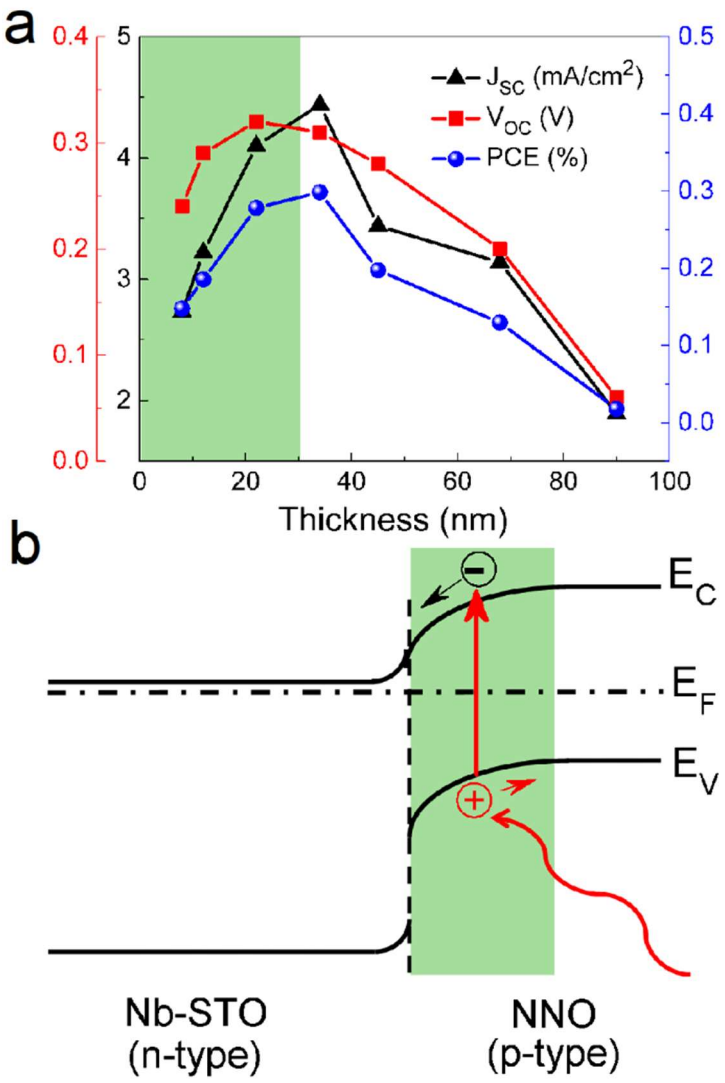

Figure 5.3 (a) Thickness dependence of the photovoltaic performance of Au/$NdNiO_3$/Nb-$SrTiO_3$ heterojunctions. P(O_2) is fixed at 0.5 mTorr. (b) Schematic energy diagram across the interface in the $NdNiO_3$/Nb- $SrTiO_3$ heterojunctions.

5.2.4 PV performance of $RNiO_3$/ Nb-$SrTiO_3$ heterostructures

For bulk $RNiO_3$ crystals, as the ionic radius of the rare-earth element gets smaller from Nd to Sm, Gd and Lu, the corresponding Ni-O-Ni bond angle increases.[18] Ni-O-Ni bond angles are closely related to the electronic structures of $RNiO_3$. When the Ni-O-Ni bond angles decreases, so does the bandwidth, which induces a charge-transfer gap between the O 2p and Ni 3d states. While for rare earth elements with large ionic radius, the overlapping between O 2p and Ni 3d states leads to a smaller or even negative charge-transfer energy (Δ), making the corresponding $RNiO_3$ semi-metals. This is consistent with the fact that when the rare-earth element changes from Nd, Sm and Gd, the T_{MI} increases.[19] So, rare-earth elements and oxygen pressure both can be used to tune the electronic phases of $RNiO_3$.

Therefore, apart from the $NdNiO_3$/Nb-$SrTiO_3$ heterojunctions, $SmNiO_3$, $GdNiO_3$ and $LuNiO_3$ are also prepared on Nb-$SrTiO_3$ substrates. The device structure is shown in Figure 5.4a. To compared the performance, the P(O_2) and thickness are fixed to 300 mTorr and 30 nm respectively for all $RNiO_3$ thin films. As discussed above, the linear fitting of $1/C^2$ versus voltage is used to get the V_{bi}. As the rare earth element changes from Sm to Lu, V_{bi} increases significantly from ~0.8 to 2.7 V. Note that the fitting for $NdNiO_3$ is not successful because there is no diode behavior for $NdNiO_3$/Nb-$SrTiO_3$ junction, as seen in Figure 5.4c. As rare earth element changes from Sm to Lu, the rectifying characteristic of the *J-V* curves is improved, and all these heterojunctions show PV effect.

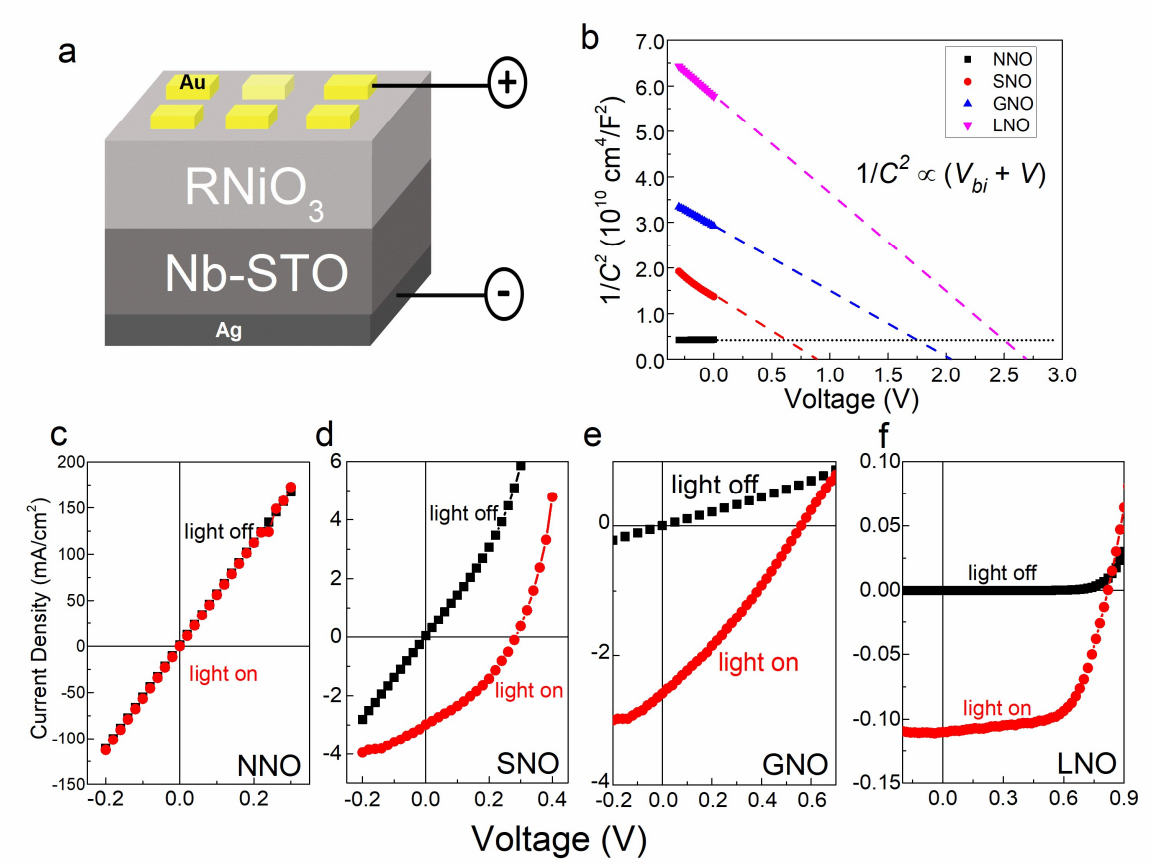

Figure 5.4 (a) Schematic device structure of the Au/$RNiO_3$/Nb-$SrTiO_3$ heterojunctions. (b) Plots of $1/C^2$ versus voltage of the $RNiO_3$/Nb-$SrTiO_3$ heterojunctions, where the 30 nm $RNiO_3$ layer is prepared under 300 mTorr $P(O_2)$. (c)-(f) *J-V* curves of $NdNiO_3$, $SmNiO_3$, $GdNiO_3$ and $LuNiO_3$ heterojunctions measured with light on and off. NNO, SNO, GNO and LNO denote $NdNiO_3$, $SmNiO_3$, $GdNiO_3$ and $LuNiO_3$.

The PV performances of devices in Figure 5.4, as well as devices with $RNiO_3$ layers prepared under different $P(O_2)$ are summarized in Figure 5.5. When $P(O_2)$ is fixed, V_{OC} increases with decreasing rare-earth ion size from Nd to Lu. While for the same rare earth element, the trend of V_{OC} varies. The maximum V_{OC} obtained increases from ~0.2 V for $NdNiO_3$ prepared under 0.5 mTorr to ~0.8 V for $LuNiO_3$ prepared under 600 mTorr as shown in Figure 5.5a. Although the V_{OC} is large, the J_{SC} decreases significantly as the rare-earth element changes to Gd and Lu, likely because the large bandgaps reduce the light absorption. The PCEs of these devices are summarized in Figure 5.5c. The balance between V_{OC} and J_{SC} leads to a maximum PCE of around 0.26 % for $SmNiO_3$/Nb-$SrTiO_3$

junction with $SmNiO_3$ layer prepared under 20 mTorr. The red area indicated by black dot line indicates that Nd or Sm should be chosen for maximum PCE of $RNiO_3$/Nb-$SrTiO_3$ heterojunctions and the corresponding $P(O_2)$ should be between 1 and 100 mTorr.

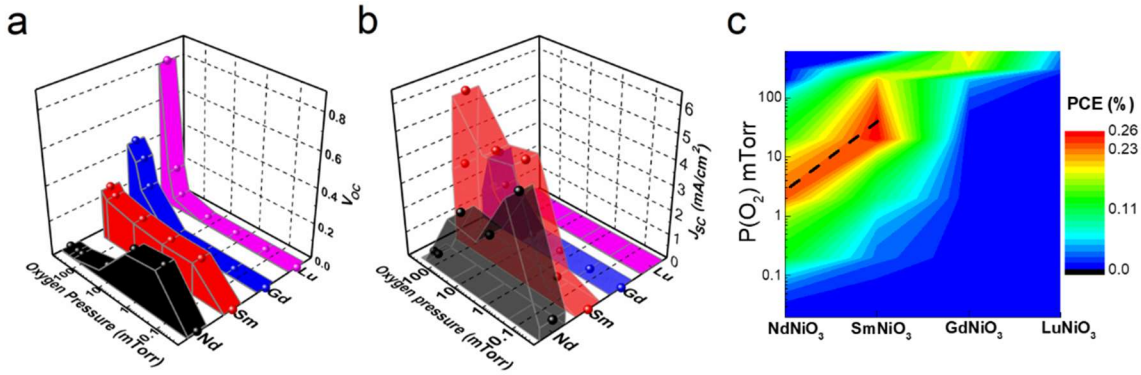

Figure 5.5 Oxygen pressure dependence of (a) V_{OC} and (b) J_{SC} for different $RNiO_3$/Nb-$SrTiO_3$ heterojunctions. (c) The calculated PCEs of different $RNiO_3$/Nb-$SrTiO_3$ heterojunctions with $RNiO_3$ of the same thickness (30 nm) prepared under different pressures.

To further improve the PCE, a p-i-n structure is prepared, where i represents an ultrathin insulating $SrTiO_3$ layer. With this layer, the rectifying characteristic is much improved as shown in Figure 5.6a. Under illumination, the V_{OC} and J_{SC} increase simultaneously by about twice, resulting in the increase of PCE from 0.20 % to 1.10 %. This is due to the enlarged depletion layer, which helps to reduce the recombination of photo-generated carriers.[20-22]

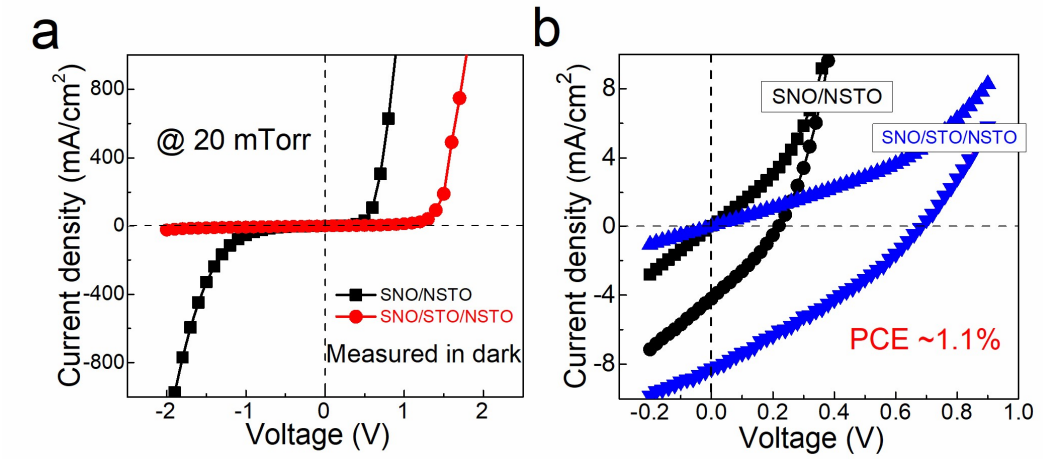

Figure 5.6 (a) *J-V* characteristics of $SmNiO_3$ (30 nm)/Nb-$SrTiO_3$ and $SmNiO_3$/$SrTiO_3$ (5 nm)/ Nb-$SrTiO_3$ heterojunctions with $RNiO_3$ layer prepared under 20 mTorr when light is off. (b) *J-V* curves of $SmNiO_3$ (30 nm)/Nb-$SrTiO_3$ and $SmNiO_3$/$SrTiO_3$ (5 nm)/Nb-$SrTiO_3$ heterojunctions measured in dark and under illumination. SNO, STO, NSTO denote $SmNiO_3$, $SrTiO_3$ and Nb-$SrTiO_3$.

5.3 Conclusions

In summary, a systematic study was conducted on the PV performances of $RNiO_3$/Nb-$SrTiO_3$ heterojunctions. The optical bandgaps of $RNiO_3$ prepared under different $P(O_2)$ are investigated. Both oxygen vacancy and rare earth element have been used to tune the band structure of $RNiO_3$, which leads to improved rectifying behavior of the $RNiO_3$/Nb-$SrTiO_3$ heterojunction. To furthermore increase the depletion layer width for better photocarrier seperation, an ultra-thin insulation $SrTiO_3$ layer is introduced to form the p-i-n structure, which results in an ultimate PCE of 1.1 %. The work presented in this chapter opens new possibility for the application of band engineered $RNiO_3$ films for solar energy harvesting. One can envision a tandem cell with several $RNiO_3$ light absorbing layers of different bandgaps to further enhance the light absorbing and improve the PCE. $RNiO_3$ has much better stability and less toxicity as compared with the hybrid perovskites.

References

[1] V. Devabhaktuni, M. Alam, S. S. S. R. Depuru, R. C. Green II, D. Nims, and C. Near. *Renew. Sust. Ener. Rev.* **2013**, 19, 555-564.

[2] A. Kojima, K. Teshima, Y. Shirai, and T. Miyasaka. *J. Am. Chem. Soc.* 2009, 131, 6050-6051.

[3] M. Grätzel. *Nat. Mater.* **2014**, 13, 838.

[4] M. A. Green, A. Ho-Baillie, and H. J. Snaith. *Nat. Photonics* **2014**, 8, 134.

[5] S. D. Stranks and H. J. Snaith. *Nat. Nanotechnol.* **2015**, 10, 391.

[6] Y. Zhou, L. You, S. Wang, Z. Ku, H. Fan, D. Schmidt, A. Rusydi, L. Chang, L. Wang, P. Ren and J. L. Wang. *Nat. Commun.* **2016**, 7, 11193.

[7] G. Xing, N. Mathews, S. Sun, S. S. Lim, Y. M. Lam, M. Grätzel, S. Mhaisalkar, and T. C. Sum. *Science* **2013**, 342, 344-347.

[8] C. Wehrenfennig, G. E. Eperon, M. B. Johnston, H. J. Snaith, and L. M. Herz. *Adv. Mater.* **2014**, 26, 1584-1589.

[9] S. D. Stranks, G. E. Eperon, G. Grancini, C. Menelaou, M. J. Alcocer, T. Leijtens, L. M. Herz, A. Petrozza, and H. J. Snaith. *Science* **2013**, 342, 341-344.

[10] C. S. Ponseca Jr, T. J. Savenije, M. Abdellah, K. Zheng, A. Yartsev, T. r. Pascher, T. Harlang, P. Chabera, T. Pullerits, and A. Stepanov. *J. Am. Chem. Soc.* **2014**, 136, 5189-5192.

[11] R. Nechache, C. Harnagea, S. Li, L. Cardenas, W. Huang, J. Chakrabartty, and F. Rosei. *Nat. Photonics* **2015**, 9, 61.

[12] J. Tauc. *Mater. Res. Bull.* **1968**, 3, 37-46.

[13] D. A. Neamen. *Semiconductor Physics and Devices: basic principles.* **2003**, McGraw-Hill Companies.

[14] C. Wang, K. J. Jin, R. Q. Zhao, H. B. Lu, H. Z. Guo, C. Ge, M. He, C. Wang, and G. Z. Yang. *Appl. Phys. Lett.* **2011**, 98, 181101.

[15] T. Kirchartz, T. Agostinelli, M. Campoy-Quiles, W. Gong, and J. Nelson. *J. Phys. Chem. Lett*. **2012**, 3, 3470-3475.

[16] T. Kirchartz, J. Bisquert, I. Mora-Sero, and G. Garcia-Belmonte. *Phys. Chem. Chem. Phys.* **2015**, 17, 4007-4014.

[17] L. Wang, Y. L. Jin, K. J. Jin, C. Wang, H. B. Lu, C. Wang, C. Ge, X. Y. Chen, E. J. Guo, and G. Z. Yang. *Europhys. Lett.* **2011**, 96, 17008.

[18] Y. Jia. *J. Solid State Chem.* **1991**, 95, 184-187.

[19] J. Varignon, M. N. Grisolia, J. Íñiguez, A. Barthélémy, and M. Bibes. *npj Quantum Mater.* **2017**, 2, 21.

[20] W. J. Zhou, K. J. Jin, H. Z. Guo, X. He, M. He, X. L. Xu, H. B. Lu, and G. Z. Yang. *Appl. Phys. Lett.* **2015**, 106, 131109.

[21] T. Choi, L. Jiang, S. Lee, T. Egami, and H. N. Lee. *New J. Phys.* **2012**, 14, 093056.

[22] T. Muramatsu, Y. Muraoka, and Z. Hiroi. *Solid State Commun.* **2004**, 132, 351-354.

Chapter 6

Self-powered Ultra-Sensitive Photodetector Based on Nickelates Heterojunctions

In this chapter, a novel self-powered photodetector based on $GdNiO_3$/Nb-$SrTiO_3$ heterojunction is introduced. These self-powered photodetectors show high sensitivity toward a wide spectrum of light between 600 and 365 nm. Under the illumination of 365 nm-ultraviolet light at 50 $\mu W/cm^2$, such specially designed photodetector shows a responsivity of 0.23 A/W at 0 V bias, and the maximum photo-dark ratio reaches close to 10^3. The work presented here demonstrates the potential of using $RNiO_3$ in optoelectronics.

6.1 Introduction

In Chapter 5, it has been shown that, by means of changing the rare earth element or adjusting the oxygen pressure ($P(O_2)$) during deposition, one can tune the bandgaps of $RNiO_3$ so that they are suitable for solar energy harvesting. A PCE of 1.1% is achieved using an Au/$SmNiO_3$/$SrTiO_3$(5 nm)/Nb-$SrTiO_3$ heterostructure. However, limited by the heterostructure, the thickness of the absorber layer is only ~40 nm, which is much thinner than the light absorbing layer in typical solar cells. For example, the absorber layer is usually around 500 nm in the recently developed organic-inorganic hybrid perovskite solar cells.[1] However, increasing the thickness of $RNiO_3$ layer has adverse effect on the PCE because of increased recombination of photo-carriers as their diffusion length in $RNiO_3$ is limited. Further study should be focused on increasing the carrier diffusion length in these materials.

Apart from PV devices, the bandgap tuning of $RNiO_3$ also makes them ideal candidates for photodetectors (PDs). Such devices covert optical signals to electrical signals and are essential components in many fields such as communications, environmental monitoring, optoelectronic circuits, and intelligent buildings.[2-6] There are many commercialized PDs, most of which are made from conventional semiconductors such as GaN, Si and InGaAs. They can be used to detect ultraviolet (UV), visible, and near-infrared light, respectively. For practical applications, it is desirable for PDs to be able to detect photons within a wide spectrum. Much efforts have been devoted to finding the proper materials[7-13], including the recently developed hybrid perovskites.[12] However, these organic-inorganic hybrid perovskites are not stable in ambient condition and easily desovled in water, which leads to serious environmental concerns. From this point of view, perovskite oxides are more suitable candidates because of their high stability. Furthermore, we can tune the bandgaps of $RNiO_3$ for optimized performance as PDs.

For conventional PDs, an external bias is usually needed to separate the photo-generated carriers and the photo-response can be adjusted by changing the bias. In Chapter 5, it has been demonstrated that $RNiO_3$ thin films can absorb light and generate electricity when

they are combined with Nb-$SrTiO_3$ substrates. With the built-in electric field at the $RNiO_3$/Nb-$SrTiO_3$ interface serving as the driving force to separate electron-hole pairs, No external bias would be needed if we use such heterostructures as PDs. One can even tune the bandgap of $RNiO_3$ by controlling the $P(O_2)$ to optimize its performance for different light wavelength.

In this chapter, self-powered PDs based on $GdNiO_3$/Nb-$SrTiO_3$ heterojunctions are presented. $GdNiO_3$ is chosen because its relatively large bandgap is suitable for UV detection, though lights with longer wavelengths are also used in this study. By adjusting the $P(O_2)$ during film deposition, the bandgaps of $GdNiO_3$ thin films are tuned. Such PDs can work under ambient condition and the responsivity can reach as high as 0.23 A/W without any external bias. It shows a broadband response, sensitive to light ranging from 365 to 650 nm. A photo-dark ratio larger than 10^2 can be achieved under 365 nm UV light illumination with power density of only 50 $\mu W/cm^2$. Moreover, the device performance is stable even after 6 months.

6.2 Results and Discussion

6.2.1 Sample preparation and structure characterizations

$GdNiO_3$ thin films were deposited on (001)-oriented single-crystal $SrTiO_3$ and 0.7 wt% Nb-$SrTiO_3$ substrates by PLD. The substrate temperature was kept at 675 ºC. The $P(O_2)$ during deposition was varied between 300 and 0.2 mTorr as needed. After deposition, the $P(O_2)$ was kept unchanged until the temperature was decreased to room temperature. A set of $GdNiO_3$/Nb-$SrTiO_3$ heterojunctions were fabricated by varying the $P(O_2)$. Au electrodes were deposited by PLD onto the surface of $GdNiO_3$ thin films. The thickness and size of Au electrodes are 10 nm and 400×400 μm^2. To evaluate the performance of the PDs, a pA meter/direct current (DC) voltage source (Hewlett Package 4140B) was used on a low noise probe station. An UV (365 nm) light-emitting diode (LED) with adjustable power density from 0.05 to 0.6 mW/cm^2 was used as the light source. Monochromatic laser diodes with different wavelengths between 460 and 980 nm and

optical power density of 10 mW/cm^2 were also used.

HR-XRD patterns of $GdNiO_3$ thin films on (001) oriented $SrTiO_3$ substrates are shown in Figure 6.1. Only diffraction peaks from the substrates and $GdNiO_3$ films are observed, indicating that the $GdNiO_3$ layers are free of impurities. The (002) diffraction peak of the film shifts towards smaller angles with decreasing $P(O_2)$. The calculated *c*-axis lattice constants of $GdNiO_3$ films are 3.84, 3.87, 3.92, 3.97, and 4.01 Å for samples prepared under 300, 100, 20, 2, 0.2 mTorr, respectively. This can be attributed to the effect of the oxygen vacancies. In order to satisfy the charge neutrality within each unit cell, Ni ions vary from Ni^{3+} to low valence state (Ni^{2+}) due to the existence of oxygen vacancies, thus leading to a larger Ni ionic radius and a larger lattice constant.[14-17] Similar phenomena of enlarged lattice constants have also been observed in $NdNiO_3$ as discussed in Chapter 4.

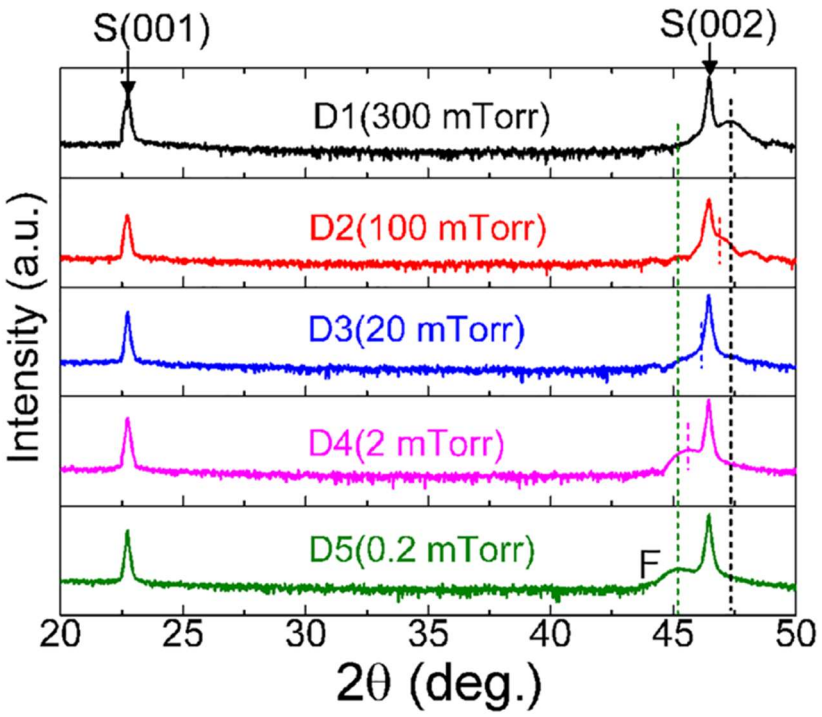

Figure 6.1 Room-temperature HR-XRD patterns of $GdNiO_3$ thin films grown on (001) oriented $SrTiO_3$ substrates. 'S' denotes the diffraction peaks of the substrates. 'F' denotes the diffraction peaks of $GdNiO_3$ films. D1 to D5 denote $GdNiO_3$ thin films deposited under 300, 100, 20, 2, and 0.2 mTorr, respectively. The (002) diffraction peak of the $GdNiO_3$ film shifts towards

smaller diffraction angles with decreasing $P(O_2)$.

6.2.2 Absorption spectrum characterization

Figure 6.2 presents the photon energy dependence of the absorption coefficient α of samples prepared under different $P(O_2)$. The corresponding Tauc plots and the linear fittings are shown in Figure 6.2b. From the intercept of linear fittings of Tauc plots, optical bandgap of $GdNiO_3$ prepared under 300 mTorr is 2.1 eV, while for samples prepared under lower $P(O_2)$, larger optical bandgaps are observed.

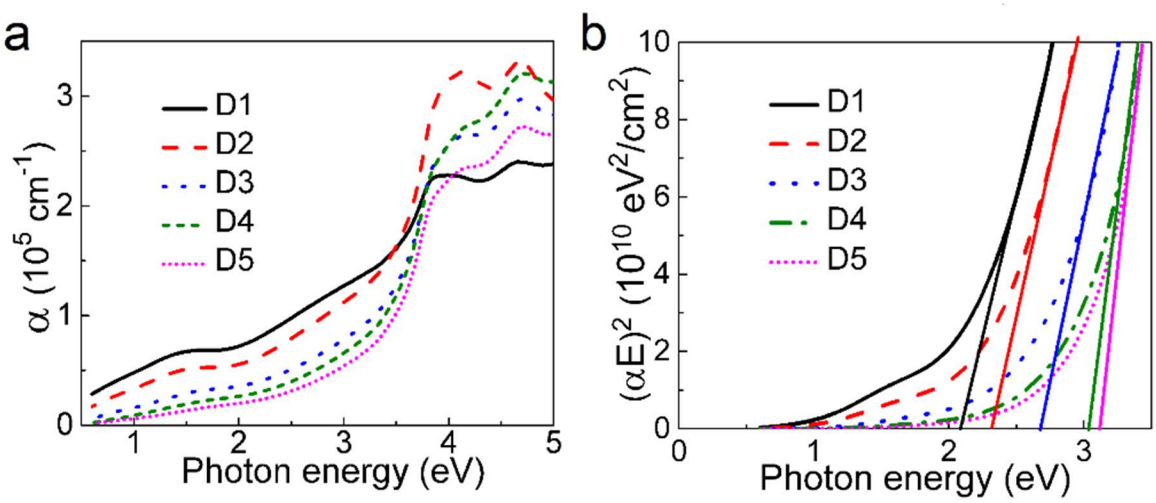

Figure 6.2 (a) Absorption coefficient of $GdNiO_3$ thin films extracted from spectroscopic ellipsometry measurements. D1 to D5 denote $GdNiO_3$ thin films deposited under 300, 100, 20, 2, and 0.2 mTorr respectively. (b) Tauc plots calculated from (a) and linear fittings of the absorption spectra. The interceptions of linear fittings with the x-axis reveal the optical bandgaps. As the $P(O_2)$ decreases, bandgap increases.

XAS measurements were conducted to investigate the valence state of Ni ions. The results are presented in Figure 6.3. The Ni L_3 portion of the spectra are mainly composed of a sharp peak around 853 eV and a broad satellite peak near 854 eV, labeled as A and B, respectively. The clear split of these two peaks in L_3 edge indicates that the samples are insulating.[18, 19] The intensity ratio between the L_3 and L_2 peaks in the Ni L_{32} edge

provide an estimation of Ni valence.[20] The ratio of L_3/L_2 increases with decreasing $P(O_2)$ as shown in Figure 6.3a, suggesting lower Ni valence in the $GdNiO_3$ films deposited under lower $P(O_2)$, consistent with the electron-doping effect from oxygen vacancies.[21] For cuprates, a local singlet state near Fermi level (E_F) were formed due to the O 2p - Cu 3d hybridization which has been named Zhang-Rice Singlet.[22] Compared with the Cu *L* edge of cuprates,[23-25] the peak B may be related to the ligand hole due to the hybridization between Ni 3d and O 2p orbitals. To confirm this, the O *K* edge absorption spectroscopy was performed (Figure 6.3b). The O *K* edge spectra are in good agreement with that in other reports.[26, 27] The intensity of the pre-peak near 529 eV (labeled by a red arrow) is a measure of the covalency in the case of nickelates.[28] It shows similar trend as the intensity of peak B in Ni L_3 edge XAS spectra, indicating that Ni 3d - O 2p hybridization decreases with decreasing $P(O_2)$. Moreover, the decreasing intensity of the pre-peak in the O *K* edge suggests the existence of larger amount of oxygen vacancies in $GdNiO_3$ films deposited under lower $P(O_2)$, consistent with the change of lattice constant.

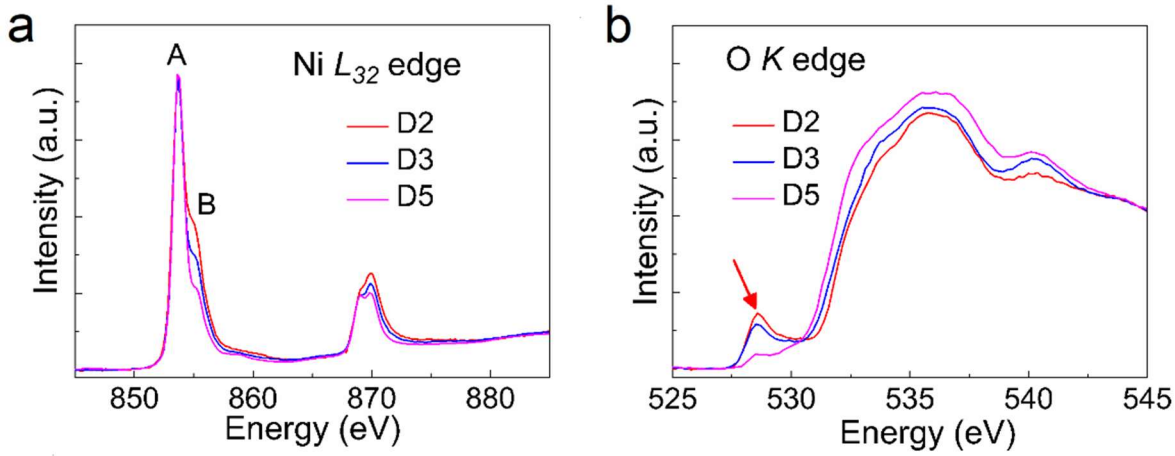

Figure 6.3 Ni L_{32} edge (a) and O *K* edge (b) spectra of three representative samples extracted from XAS measurements. To clearly show the peak splitting and the gradual intensity change, only the results of samples prepared under 100 (D2), 20 (D3), 0.2 (D5) mTorr are plotted. A and B in the L_3 portion of the spectra label the peak around 853 eV and a broad satellite peak near 854 eV, respectively. The intensity ratio between L_3 and L_2 peaks increases when $P(O_2)$ decreases. The red arrow in (b) labels the pre-peak near 529 eV of O *K* edge spectra, which measures covalency between Ni and O. The intensity of the pre-peak decreases when $P(O_2)$ decreases,

indicating reduced hybridization.

The bandgap values are extracted from the ellipsometry results. If combined with the results from XPS, the E_V and E_F can be derived. Therefore, the complete band diagrams can be drafted as shown in Figure 6.4. For Nb-$SrTiO_3$ substrates, the E_F locates above the conduction band bottom (E_C~4.0 eV) due to the high doping concentration of 0.7 wt.%. The E_F of $GdNiO_3$ shifts up with decreasing $P(O_2)$, which is consistent with oxygen vacancies being donor dopants, suggesting that the built-in electric field at the $GdNiO_3$/Nb-$SrTiO_3$ interface decreases with decreasing $P(O_2)$.

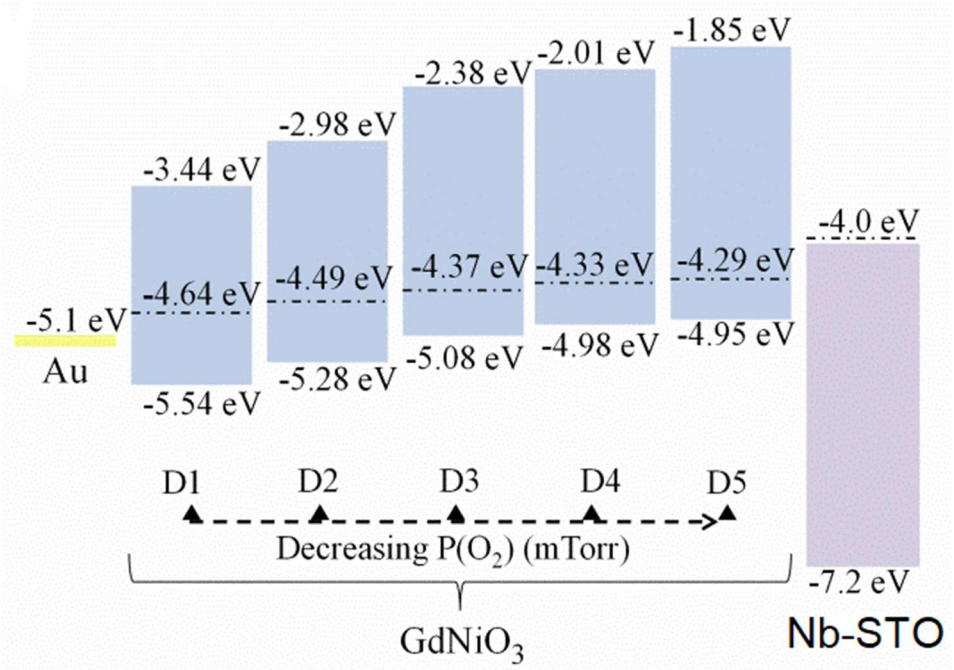

Figure 6.4 Energy levels and work functions across the Au/$GdNiO_3$/Nb-$SrTiO_3$ heterojunctions. The dashed lines denote the E_F. The top of valence band (E_V) is extracted from UPS results. The bottom of conduction band (E_C) is calculated by using the bandgap values and E_V.

6.2.3 Performances of $GdNiO_3$/Nb-$SrTiO_3$ heterojunctions as photodetectors

Figure 6.5a shows schematically the self-powered PDs based on the $GdNiO_3$/Nb-$SrTiO_3$

heterojunctions. Semitransparent Au is used as top electrodes. The contact between Au and $GdNiO_3$ is Ohmic. The built-in electric field at the $GdNiO_3$/Nb-$SrTiO_3$ interface provides the driving force for efficient separation of photo-generated carriers. Therefore, such PDs are self-powered and doesn't require external power sources.

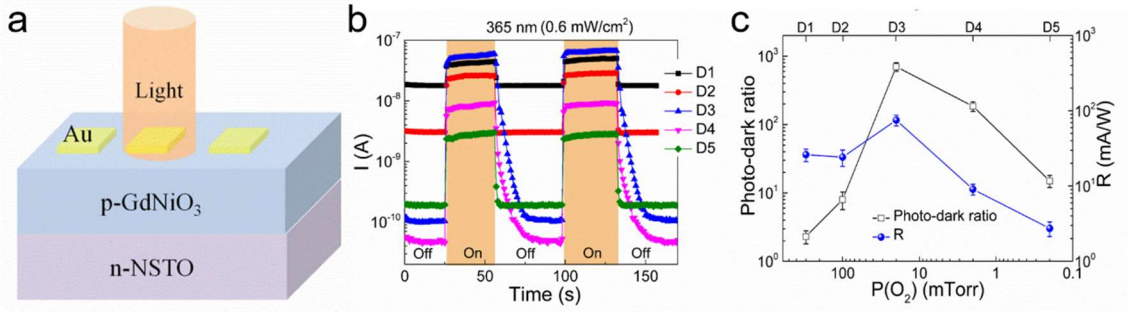

Figure 6.5 (a) Schematic diagram of the PDs based on Au/$GdNiO_3$/Nb-$SrTiO_3$ heterojunctions. (b) Responses of the Au/$GdNiO_3$/Nb-$SrTiO_3$ PDs with light on and off. The illumination is supplied by a 365 nm-UV light with power density of 0.6 mW/cm^2. (c) Photo-dark ratio and responsivity versus P(O_2) extracted from (b). D1 to D5 denote $GdNiO_3$ thin films deposited under 300, 100, 20, 2, and 0.2 mTorr respectively. All devices have Au top electrodes with area of 400×400 μm^2.

The photo-responses of these PDs with $GdNiO_3$ prepared under different P(O_2) are shown in Figure 6.5b. Under illumination, the photocurrents increase for all samples and return to the low value after the UV light is turned off. Photo-dark ratio is a key parameter for PDs, which is defined as I_{PH}/I_{OFF}, where I_{PH} represents the current generated under illumination and I_{PH} equals to I_{ON} subtracted by I_{OFF}. I_{ON} and I_{OFF} represent the current when light is on and off, respectively. Another important parameter pf PD performance is responsivity (R), which is defined as

$$R = \frac{I_{PH}}{P_{IN} \times S},$$

where P_{IN} is the power density of light and S is the device area. photo-dark ratio and R are affected by P(O_2) as shown in Figure 6.5c and Table 6.1.

Table 6.1 Performances of the photodetectors based on $GdNiO_3$/Nb-$SrTiO_3$ heterojunctions. The illumination is UV light with wavelength and power density of 365nm and 0.6 mW/cm^2. D1 to D5 denote $GdNiO_3$ thin films deposited under 300, 100, 20, 2, and 0.2 mTorr, respectively.

Device	I_{OFF} [nA]	I_{ON} [nA]	Photo-dark ratio /	R [mA/W]	Bandgaps eV
D1	18.50	49.2	2.7	3.1	2.1
D2	3.140	28.8	9.2	2.7	2.3
D3	0.099	71.2	719.2	74.2	2.7
D4	0.051	9.37	183.7	9.7	3.0
D5	0.187	2.92	15.6	2.8	3.1

As shown in Table 6.1, sample prepared under P(O_2) of 20 mTorr (D3) works the best and the photo-dark ratio reaches ~720. The responsivity is ~74 mA/W. Note that the photon energy of the 365 nm-UV light is enough to excite electrons from valence band to conduction band for all samples. Because the largest bandgap (3 eV) for sample prepared under 0.2 mTorr corresponds to a light wavelength of 413.28 nm, which is larger than the wavelength of the UV light used. Therefore, the best performance for D3 (20 mTorr) samples must be due to the built-in electric field and low recombination.

Based on the results under illumination of 365 nm-UV light, subsequent analysis was extended to photo-response of sample prepared under 20 mTorr towards lights with different wavelengths. Figure 6.6a shows the photo-response measured using different light sources with wavelength between 365 and 980 nm. The input power density is fixed at 10 mW/cm^2 except the 365 nm UV light because of the equipment limitation (light intensity of 0.6 mW/cm^2). The I_{ON} is negligible under illumination with light of 808 and 980 nm. The photo-response starts to appear when the wavelength decreases to 650 nm and gradually increases. The responsivity of the PD towards light with different wavelengths follows the absorption spectrum, as presented in Figure 6.6b.

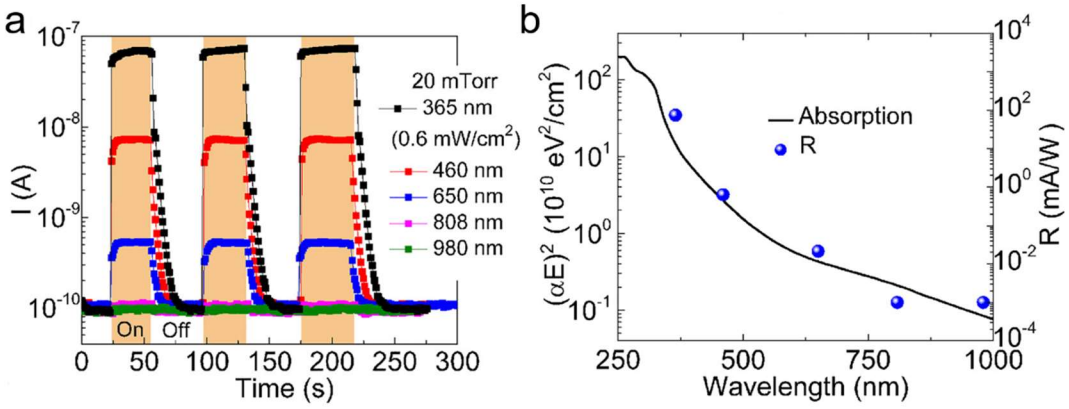

Figure 6.6 (a) Photo-response of $GdNiO_3$/Nb-$SrTiO_3$ heterojunctions with $GdNiO_3$ layer prepared under 20 mTorr. The light power density is fixed at 10 mW/cm^2 except for 365 nm UV light because of the equipment limitation (light intensity of 0.6 mW/cm^2). (b)The responsivity as a function of wavelength and the corresponding Tauc plots. The Tauc plots are extracted from the absorption spectra as presented in Figure 6.2. Here, R denotes responsivity.

The light intensity dependence of the photo-response under 365 nm illumination is shown in Figure 6.7a. An approximately linear relationship between P_{IN} and I_{PH} can be observed because higher light intensity brings more photons, resulting in more photon-generated carries. However, responsivity decreases with increasing light intensity as shown in Figure 6.7b. This may be due to the carrier trapping saturation and a reduction in the recombination barrier.[29] The best performing Au/$GdNiO_3$(20 mTorr)/Nb-$SrTiO_3$ PD shows a responsivity of ~0.23 A/W under illumination of 365 nm-UV light at 50 μW/cm^2. It is comparable to or even better than the UV PDs made of conventional semiconductors such as GaN (~ 0.01 A/W) or ZnO (~0.3 A/W).[30-32] Compared with other PDs based on novel semiconductor materials such as MoS_2,[33, 34] long-time stability of the $GdNiO_3$-based PDs is an advantage. The photo-response of these PDs are monitored for 6 months and both I_{PH} and responsivity are quite stable without any decay. (Figure 6.7c) Moreover, to confirm the performance is repeatable, random devices are chosen and the I_{PH} is always within the range of 10-20 nA, suggesting good reproducibility of the PD devices.

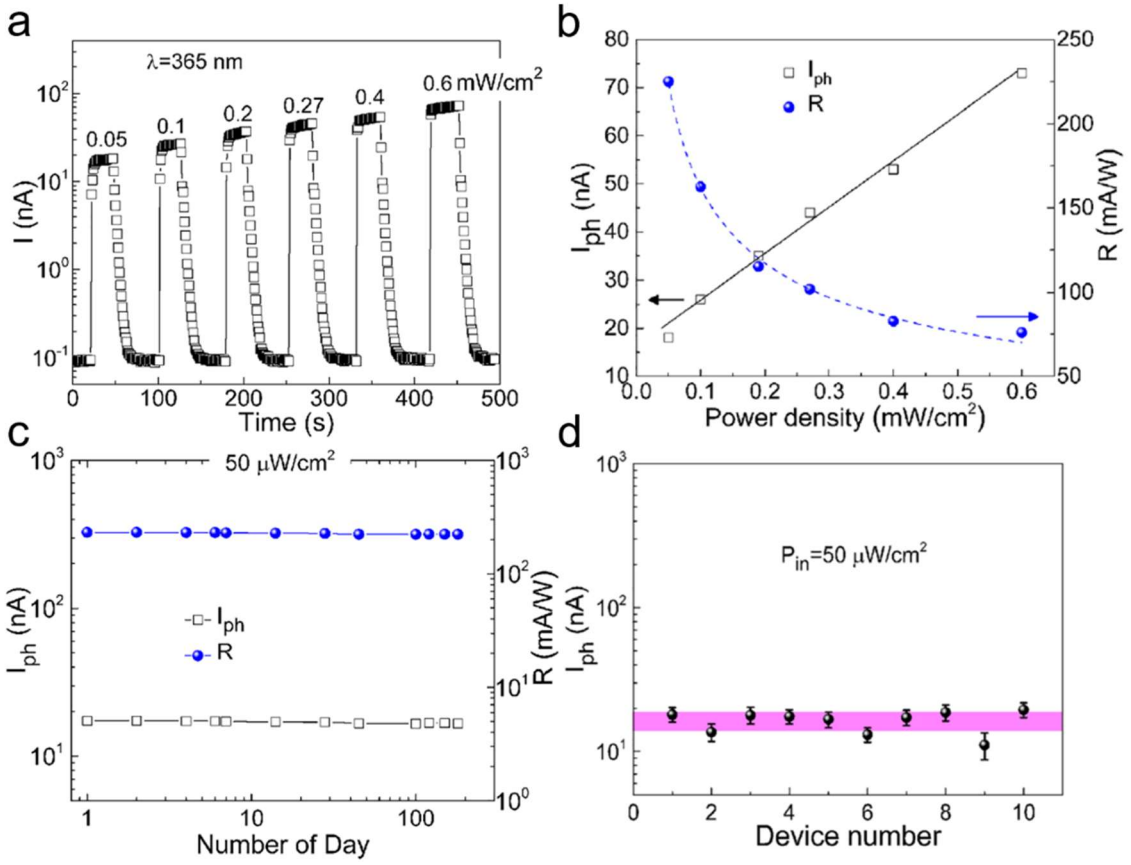

Figure 6.7 (a) Photo-response of the Au/$GdNiO_3$(20 mTorr)/Nb-$SrTiO_3$ heterojunction as a function of time. The illumination is supplied by a 365 nm-UV light source. The 'I' represent I_{ON}. (b) I_{PH} and responsivity calculated from (a), where $I_{PH} = I_{ON} - I_{OFF}$. (c) Device stability in air at room temperature. The illumination is supplied by a 365 nm-UV light source at 50 μW/cm^2. (d) Device reproducibility under illumination of 365 nm-UV light at 50 μW/cm^2.

6.3 Conclusions

In summary, the band structure of $GdNiO_3$ thin films has been engineered by controlling the oxygen vacancy. Absorption spectra analysis confirms the reduction of Ni^{3+} to Ni^{2+} and the complete energy diagrams have been obtained.

A novel self-powered PD based on $GdNiO_3$/Nb-$SrTiO_3$ heterojunction is introduced. These devices show high sensitivity toward a wide spectrum of light from 600 to 365 nm. Under UV light of 365 nm at 50 μW/cm^2, the PD shows a responsivity of 0.23 A/W

without any external bias, and the photo-dark ratio reaches ~ 10^3 when the light intensity is 0.6 mW/cm^2. The high photo-response originates from the low dark current (~10^{-10} A) and the built-in electric field formed at the interface.

References

[1] J. H. Heo, S. H. Im, J. H. Noh, T. N. Mandal, C. S. Lim, J. A. Chang, Y. H. Lee, H. J. Kim, A. Sarkar, and M. K. Nazeeruddin. *Nat. Photonics* **2013**, 7, 486.

[2] H. Zimmermann. *Integrated silicon optoelectronics* **2000**, Springer.

[3] F. Liu, H. Shimotani, H. Shang, T. Kanagasekaran, V. Zolyomi, N. Drummond, V. I. Fal'ko, and K. Tanigaki. *ACS nano* **2014**, 8, 752-760.

[4] S. M. Hatch, J. Briscoe, and S. Dunn. *Adv. Mater.* **2013**, 25, 867-871.

[5] F. Xia, T. Mueller, Y. M. Lin, A. Valdes-Garcia, and P. Avouris. *Nat. Nanotechnol.* **2009**, 4, 839-843.

[6] S. Assefa, F. Xia, and Y. A. Vlasov. *Nature* **2010**, 464, 80-84.

[7] Y. Yoneda and I. Hanawa. **2004**, Patent *US6831265B2*.

[8] M. S. Arnold, J. D. Zimmerman, C. K. Renshaw, X. Xu, R. R. Lunt, C. M. Austin, and S. R. Forrest. *Nano Lett.* **2009**, 9, 3354-3358.

[9] R. Dong, C. Bi, Q. Dong, F. Guo, Y. Yuan, Y. Fang, Z. Xiao, and J. Huang. *Adv. Opt. Mater.* **2014**, 2, 549-554.

[10] X. Hu, X. Zhang, L. Liang, J. Bao, S. Li, W. Yang, and Y. Xie. *Adv. Funct. Mater.* **2014**, 24, 7373-7380.

[11] J. Yoo, S. Jeong, S. Kim, and J. H. Je. *Adv. Mater.* **2015**, 27, 1712-1717.

[12] Y. Lee, J. Kwon, E. Hwang, C. H. Ra, W. J. Yoo, J. H. Ahn, J. H. Park, and J. H. Cho. *Adv. Mater.* **2015**, 27, 41-46.

[13] F. Koppens, T. Mueller, P. Avouris, A. Ferrari, M. Vitiello, and M. Polini. *Nat. Nanotechnol.* **2014**, 9, 780-793.

[14] L. Wang, S. Dash, L. Chang, L. You, Y. Feng, X. He, K. J. Jin, Y. Zhou, H. G. Ong, P. Ren and J. L. Wang. *ACS Appl. Mater. & Interfaces* **2016**, 8, 9769-9776.

[15] A. Shapovalov, Y. M. Boguslavskij, A. Ruban, G. Gridneva, V. Melnikov, and N. Pshentsova. *Supercond. Sci. Technol.* **1992**, 5, 283.

[16] C. Wang, B. Cheng, S. Wang, H. Lu, Y. Zhou, Z. Chen, and G. Yang. *Thin Solid Films* **2005**, 485, 82-89.

[17] Z. T. Xu, K. J. Jin, L. Gu, Y. L. Jin, C. Ge, C. Wang, H. Z. Guo, H. B. Lu, R. Q. Zhao, and G. Z. Yang. *Small* **2012**, 8, 1279-1284.

[18] C. Piamonteze, F. De Groot, H. Tolentino, A. Ramos, N. Massa, J. Alonso, and M. Martínez-Lope. *Phys. Rev. B* **2005**, 71, 020406.

[19] M. Medarde, C. Dallera, M. Grioni, B. Delley, F. Vernay, J. Mesot, M. Sikora, J. Alonso, and M. Martínez-Lope. *Phys. Rev. B* **2009**, 80, 245105.

[20] S. Muto, Y. Sasano, K. Tatsumi, T. Sasaki, K. Horibuchi, Y. Takeuchi, and Y. Ukyo. *J. Electrochem. Soc.* **2009**, 156, A371-A377.

[21] H. Y. Hwang. *Nat. Mater.* **2005**, 4, 803.

[22] F. Zhang and T. Rice. *Phys. Rev. B* **1988**, 37, 3759.

[23] C. Chen, L. Tjeng, J. Kwo, H. Kao, P. Rudolf, F. Sette, and R. Fleming. *Phys. Rev. Lett.* **1992**, 68, 2543.

[24] D. Hawthorn, K. Shen, J. Geck, D. Peets, H. Wadati, J. Okamoto, S.W. Huang, D. Huang, H. J. Lin, and J. Denlinger. *Phys. Rev. B* **2011**, 84, 075125.

[25] X. Yin, S. Zeng, T. Das, G. Baskaran, T. C. Asmara, I. Santoso, X. Yu, C. Diao, P. Yang, and M. B. Breese. *Phys. Rev. Lett.* **2016**, 116, 197002.

[26] M. Abbate, G. Zampieri, F. Prado, A. Caneiro, J. Gonzalez-Calbet, and M. Vallet-Regi. *Phys. Rev. B* **2002**, 65, 155101.

[27] J. Suntivich, W. T. Hong, Y.-L. Lee, J. M. Rondinelli, W. Yang, J. B. Goodenough, B. Dabrowski, J. W. Freeland, and Y. Shao-Horn. *J. Phys. Chem. C* **2014**, 118, 1856-1863.

[28] M. L. Medarde. *J. Phys. Condens. Matter* **1997**, 9, 1679.

[29] X. Xie, S. Y. Kwok, Z. Lu, Y. Liu, Y. Cao, L. Luo, J. A. Zapien, I. Bello, C. S. Lee, and S. T. Lee. *Nanoscale* **2012**, 4, 2914-2919.

[30] H. Ohta, M. Hirano, K. Nakahara, H. Maruta, T. Tanabe, M. Kamiya, T. Kamiya, and H. Hosono. *Appl. Phys. Lett.* **2003**, 83, 1029-1031.

[31] H. Zhu, C. Shan, B. Yao, B. Li, J. Zhang, D. Zhao, D. Shen, and X. Fan. *J. Phys. Chem. C* **2008**, 112, 20546-20548.

[32] H. Zhang, X. Dai, N. Guan, A. Messanvi, V. Neplokh, V. Piazza, M. Vallo, C. Bougerol, F. O. H. Julien, and A. Babichev. *ACS Appl. Mater. Interfaces* **2016**, 8, 26198-26206.

[33] X. Wang, P. Wang, J. Wang, W. Hu, X. Zhou, N. Guo, H. Huang, S. Sun, H. Shen, and T. Lin. *Adv. Mater.* **2015**, 27, 6575-6581.

[34] D. Kufer and G. Konstantatos. *Nano Lett.* **2015**, 15, 7307-7313.

Chapter 7

Giant Resistive Switching in Nickelates Heterostructures for Non-volatile Memory

In this chapter, giant resistive switching behavior observed in nickelates-based heterostructures is discussed. Migration of oxygen vacancies driven by an electric field modulates the band diagram across the $RNiO_3$/Nb-$SrTiO_3$ interface, which leads to the observed resistance change. Detailed transmission electron microscopy studies provide evidences for the proposed model. The large ON/OFF ratio, good data retention and fatigue performance of the devices demonstrate the potential of such heterostructures for non-volatile memory.

7.1 Introduction

It has been demonstrated that oxygen vacancies affect the band structure of $RNiO_3$ thin films, which in turn changes their electrical and optical properties. Various applications can be envisioned based on the band engineered $RNiO_3$ thin films as discussed in Chapters 4 and 5. It is also demonstrated in chapter 4 that post-deposition vacuum annealing introduces oxygen vacancies into the films, which involves the breaking of Ni-O bonds and migration of oxygen ions (oxygen vacancies). This is made possible by the relative small Ni-O bond energy,[1] and suggests the possibility of dynamically control the distribution of oxygen vacancies in $RNiO_3$ films by an electric field. Previous studies have shown that oxygen vacancies can effectively modify the interfacial barrier in perovskite heterostructures.[2-7] If this could be achieved in $RNiO_3$ based heterostructures, we should expect resistive switching behavior that may be used for non-volatile memory.

In this chapter, the study on the transport behavior of Pt/$GdNiO_3$/Nb-$SrTiO_3$ heterostructures is presented. A giant bipolar resistive switching behavior with ON/OFF ratio of about 10^5 is observed at room temperature. Furthermore, the effect is tunable by varying the oxygen content or changing the rare earth elements. These findings provide an important step forward toward the development of multifunctional electronic devices based on rare earth nickelates.

7.2 Results and Discussion

7.2.1 Sample preparation and structural characterizations

$GdNiO_3$ and other $RNiO_3$ thin films were grown on (001)-oriented $SrTiO_3$, and 0.7 wt% Nb-doped $SrTiO_3$ (Nb-$SrTiO_3$) substrates by PLD. The oxygen pressure ($P(O_2)$) during thin film deposition was varied. The substrate temperature was kept at 725 ºC during deposition. The thickness of $RNiO_3$ films was kept at ~10 nm to achieve effective migration of oxygen vacancies under an electric field. After deposition, the samples were

in situ annealed for 10 min and cooled down to room temperature.

Figure 7.1a shows the AFM topography images of $GdNiO_3$ films prepared under 100 (D1), 20 (D2), 2 (D3), 0.2 (D4) mTorr oxygen pressure. The roughness of all films is less than 0.3 nm. The (002) diffraction peak of the $GdNiO_3$ film gradually shifts to the lower angle, indicating that *c*-axis lattice constant increases with decreasing $P(O_2)$, as show in Figure 7.1b. The change of *c*-axis lattice constant results from oxygen vacancies induced reduction of Ni^{3+} to Ni^{2+}, which have been discussed in previous chapters.

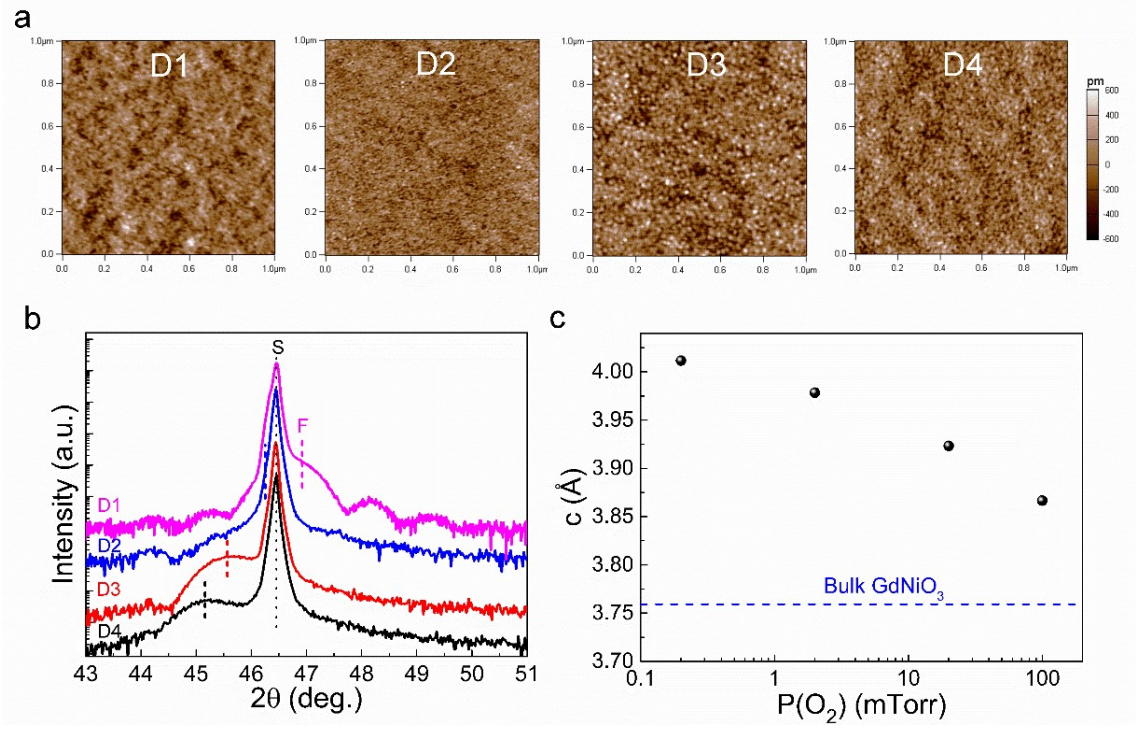

Figure 7.1 (a) AFM images of $GdNiO_3$ films prepared under 100 (D1), 20 (D2), 2 (D3), 0.2 (D4) mTorr oxygen pressure $P(O_2)$. (b) Room-temperature HR-XRD patterns around the (002) peaks. S and F represent peaks form substrates and $GdNiO_3$ films, respectively. (c) *c*-axis lattice constant as a function of $P(O_2)$ calculated from the HR-XRD patterns.

7.2.2 *I-V* characteristics and bipolar resistive switching

Figure 7.2a shows the current-voltage (*I-V*) characteristics of the Pt/$RNiO_3$/Nb-$SrTiO_3$ heterojunctions. The arrows represent the sequence of voltage sweeps. Sample prepared

under 100 mTorr (D1) $P(O_2)$ shows no resistive switching effect. When $P(O_2)$ decreases, resistive switching behavior starts to appear. Sample D4 (0.2 mTorr) shows an obvious "counter-clockwise" bipolar resistive switching behavior. The upper and lower branches of the *I-V* curves are defined as the low resistance state (LRS or ON) and high resistance state (HRS or OFF), respectively. Sample D4 (0.2 mTorr) switches from HRS (LRS) to LRS (HRS) when a forward (reverse) bias is applied to the top Pt electrode, and this is the so-called 'set' ('reset') process. The resistance versus voltage plots are presented in Figure 7.2b. It shows that the switching between HRS and LRS requires a threshold voltage of about 2 V. This is consistent with the hypothesis proposed in the introduction of this chapter.

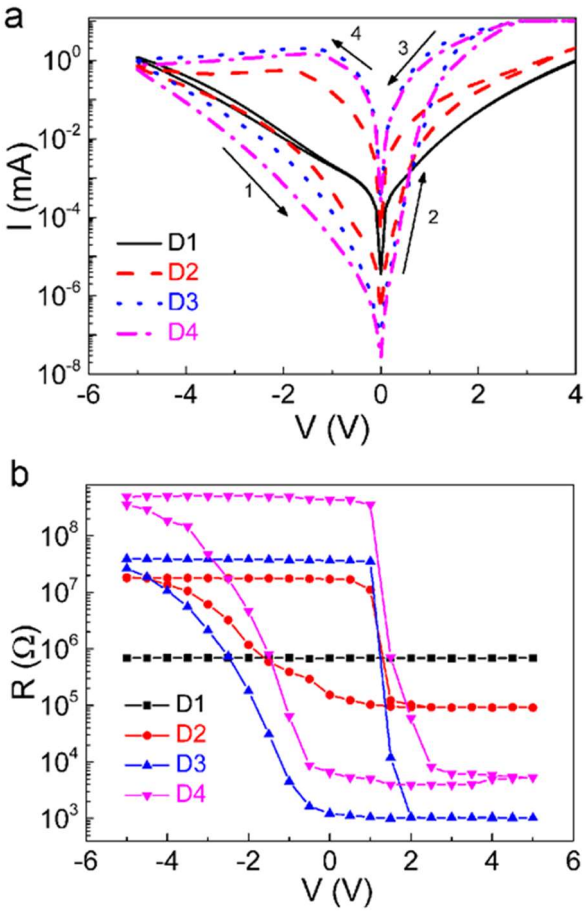

Figure 7.2 (a) *I-V* curves of $Pt/RNiO_3/Nb\text{-}SrTiO_3$ heterostructures (D1-D4) plotted on log scales. (b) Resistance of the corresponding samples (D1-D4) as a function of the applied voltage pulse. D1 to D4 denote samples prepared under 100, 20, 2 and 0.2 mTorr $P(O_2)$ respectively.

7.2.3 Resistive switching performance

According to the results presented in Figure 7.2a, sample D4 (0.2 mTorr) shows the largest ON/OFF ratio of about 10^5. Therefore, further characterizations of the resistive switching performance are conducted on Sample D4. Apart from the change in resistance, a change between high capacitance state (HCS) and low capacitance state (LCS) is also observed, indicating that the applied voltages modulate the interfacial barrier.[4, 6] One of the advantages of an interface controlled bipolar resistive switching device is that there is no need for an initial forming step and the resistance can be continuously tuned by the external bias, as shown in Figure 7.3a.

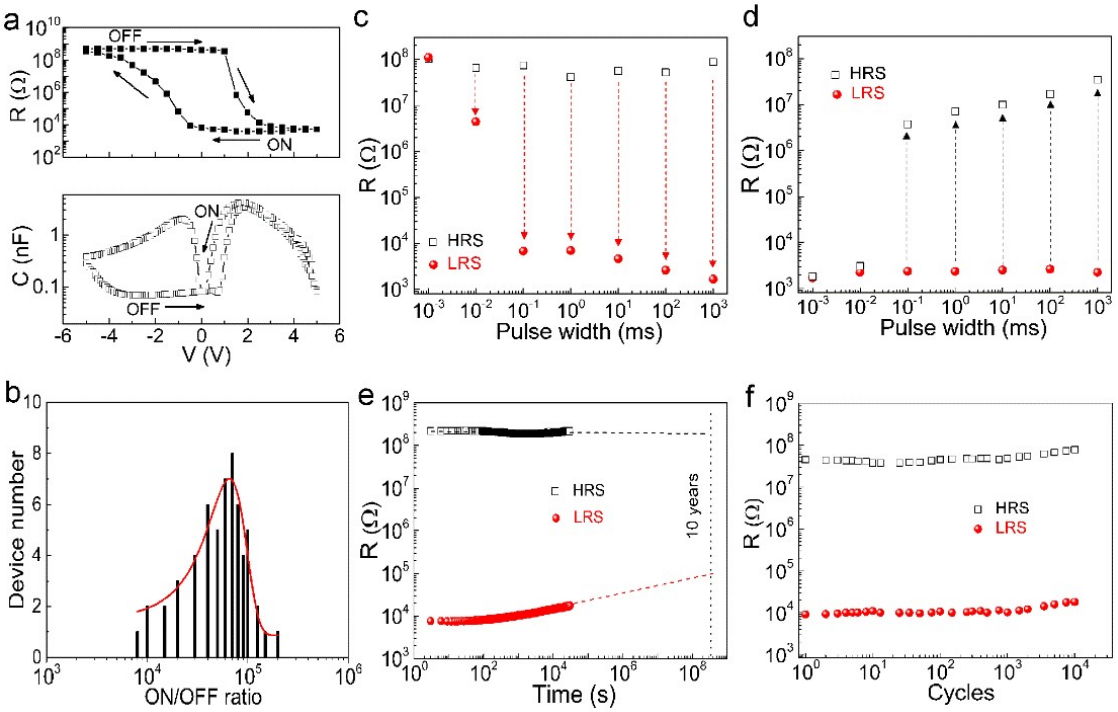

Figure 7.3 (a) Resistance and capacitance changes of sample Pt/$GdNiO_3$(0.2 mTorr)/Nb-$SrTiO_3$ (D4, 0.2 mTorr) under voltage sweeping. The *C-V* curve is extracted from impedance measurements with a 10 mV, 25 kHz AC signal imposed on a continuous DC bias. (b) The distribution of ON/OFF ratio among randomly selected devices. (c) Pulse width dependence of the resistive switching during the 'set' process. (d) Pulse width dependence of the resistive switching during the 'reset' process. Voltage pulses are 5 V. (e) Retention characteristic of the HRS and LRS recorded at -0.2 V after a forward and reverse bias sweep, respectively. (f) Fatigue

performance of the device.

To verify the reproducibility of the resistive switching behavior, randomly selected Pt/$GdNiO_3$(0.2 mTorr)/Nb-$SrTiO_3$ devices are tested. As shown in Figure 7.3b, the ON/OFF ratios fall within the range of 10^4-10^5, showing good uniformity. The pulse width dependence of 'set' and 'reset' process is measured as shown in Figure 7.3c and d. Before the measurements, the device is first set to HRS (LRS) by applying a voltage pulse of -5 V (+5 V) with duration of 1 s. Then, square voltage pulses from 1μs to 1 s are applied and the resistance of the device is recorded at -0.2 V. The results show that generally 'set' process is faster than 'reset'.

Figure 7.3e shows the retention characteristic of the device at a reading bias of -0.2 V. An ON/OFF ratio of ~ 10^3 can still be retained after ten years by extrapolating the retention data. The fatigue performance is tested by switching the device repeatedly using +5 and -5 V pulses with pulse width of 150 μs. The 'set' and 'reset' operations exhibit good endurance. No significant change in the ON/OFF is observed after more than 10^4 cycles.

7.2.4 Mechanisms of resistive switching

I-V curves of the sample prepared under 0.2 mTorr P(O_2) on linear scale are shown in Figure 7.4a. Clear resistive switching is observed with the forward (reverse) bias leading to LRS (HRS). The shape of the *I-V* curves is smooth without sudden changes, which excludes the possibility of filaments induced resistive switching behavior.[8] Generally, there are three possible conduction mechanisms to explain the transport behavior of a heterojunction: space charge limited conduction (SCLC), Schottky emission and Poole-Frenkel (*P-F*) emission. [9, 10] Fittings of the *I-V* curves using these three models are presented in Figure 7.4b.

For SCLC, the *I-V* curve follows the Child's law:[11]

$$J \propto \frac{8}{9}\varepsilon_r\varepsilon_0\mu\frac{E^2}{d},$$

where J is the current density, ε_r is the relative dielectric constant, ε_0 is the permittivity of free space, μ is the mobility of charge carriers, E is the electric field and d is the film thickness.

For Schottky emission, the *I-V* curve should follow:[12]

$$I \propto T^2 \exp[\frac{e\sqrt{(eV)/(4\pi\varepsilon_r\varepsilon_0 d)}}{k_B T}],$$

where e is the electron charge, k_B is the Boltzmann constant, T is the temperature.

For *P-F* emission, the *I-V* relationship is as following:[12]

$$\frac{I}{V} \propto \exp[\frac{e\sqrt{(eV)/(\pi\varepsilon_r\varepsilon_0)}}{r k_B T}],$$

where r is a factor between 1 and 2, depending on the exact position of the Fermi level.[13] *I-V* curves of the Pt/$GdNiO_3$(0.2 mTorr)/Nb-$SrTiO_3$ heterostructures are plotted in double-logarithmic scales in Figure 7.4b. The fittings are highlighted by color lines. It is clear that the transport behavior under LRS follows the SCLC mechanism.[11] The fitting of HRS, on the other hand, has to be divided into two regions. Schottky emission dominates under low electric field and *P-F* emission takes over under high electric field. These results are consistent with previous studies where migration of oxygen vacancies at the interface activates the resistive switching.[9, 14, 15]

A schematic diagram is shown in Figure 7.4c to explain the observed resistive switching behavior in $GdNiO_3$/Nb-$SrTiO_3$ heterostructures. During the 'set' process, positively charged oxygen vacancies migrate from the $GdNiO_{3-x}$ film into the Nb-$SrTiO_3$ substrate. As the concentration of oxygen vacancy is reduced, bandgaps of $GdNiO_{3-x}$ films will be decreased, and Fermi level shifted down. The potential barrier (V_{bi}) for electron or hole injection and depletion region width (W_d) at the interface will both be reduced, leading to the LRS. When a reverse bias pushes the oxygen vacancies back into the $GdNiO_{3-x}$ film, the potential barrier recovers, and the device returns to the HRS. Another evidence for the oxygen vacancy migration is that the LRS current decays with time following a power law ($I \sim t^{-\beta}$), as shown in Figure 7.4d. This is consistent with an oxygen vacancy diffusion model.[16, 17]

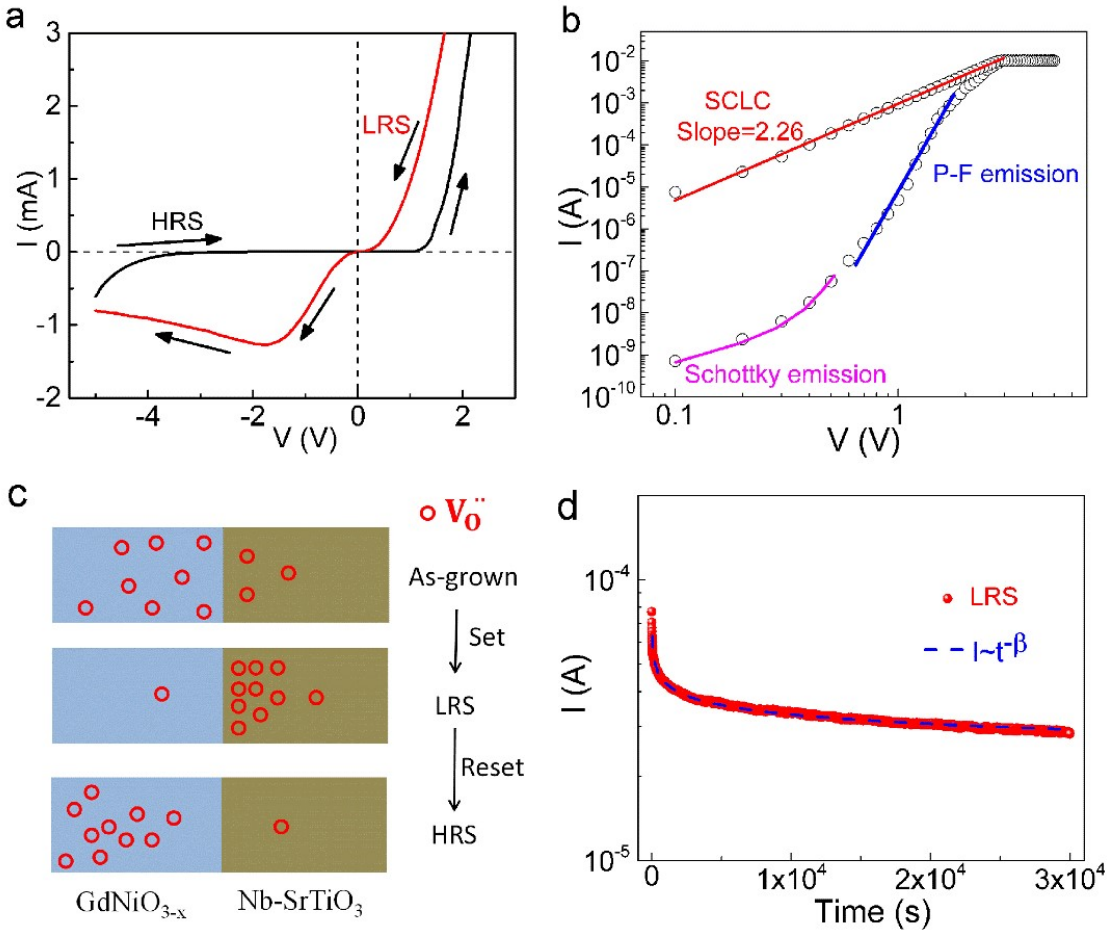

Figure 7.4 (a) Linear scale *I-V* curves of Pt/$GdNiO_3$(0.2 mTorr)/Nb-$SrTiO_3$ (D4) with voltage sweeping between -5 V to +5 V. (b) Fittings of the nonlinear *I-V* curves of the $GdNiO_3$/Nb-$SrTiO_3$ heterojunctions using difference models. (c) Migration of oxygen vacancies in $GdNiO_3$/Nb-$SrTiO_3$ heterojunctions under electric field. V_O`` denotes oxygen vacancy. (d) Time-dependence of the small-signal current of LRS. The blue dashed line is the power law fitting.

Direct evidence of oxygen vacancy migration can be obtained from TEM measurements. Compared with the as-grown state (Figure 7.5b), the high angle angular dark-field (HAADF) image of samples at LRS (Figure 7.5a) shows perfect crystallinity with less defects (i.e., oxygen vacancies) in the $GdNiO_{3-x}$ layer. Conversely, the HAADF image of sample at HRS (Figure 7.5b) shows much worse crystallinity with more defects in the $GdNiO_{3-x}$ layer. More evidences come from electron energy loss spectroscopy (EELS) measurements, which reveals the valence state of Ni. The measurements were performed

along the direction indicated by the arrows, and spectra were recorded every 5 Å. For both LRS and HRS, there are essentially no changes in either O *K* edge or Ni *L* edge EELS along the scanning paths. However, compared with LRS, the main peak (marked by the red arrow in Figure 7.5d) of O *K* edge at HRS shifts to the right slightly, implying lower Ni valence at HRS. The small pre-peak in the O *K* edge (labeled by a blue arrow in Figure 7.5e) spectrum almost disappears at HRS, suggesting the existence of large amount of oxygen vacancies.[3, 18] Moreover, the area ratio between L_3 and L_2 peaks in the Ni *L* edge spectrum provides an estimation of Ni valence state. Higher valence of cation gives rise to a smaller ratio of L_3/L_2 due to the lower occupancy of 3d-states.[19] The EELS spectra are normalized using the Ni *L* edge and the evolution of the L_3/L_2 ratio is monitored. As shown in Figure 7.5f, the L_3/L_2 area ratio at HRS is statistically higher than that at LRS, confirming that HRS possesses lower Ni valence. This is consistent with the O *K* edge analysis result. Therefore, it can be concluded that oxygen vacancies indeed migrate out of the $GdNiO_{3-x}$ layer at LRS and re-enter the $GdNiO_{3-x}$ layer at HRS, consistent with the model proposed in Figure 7.4c.

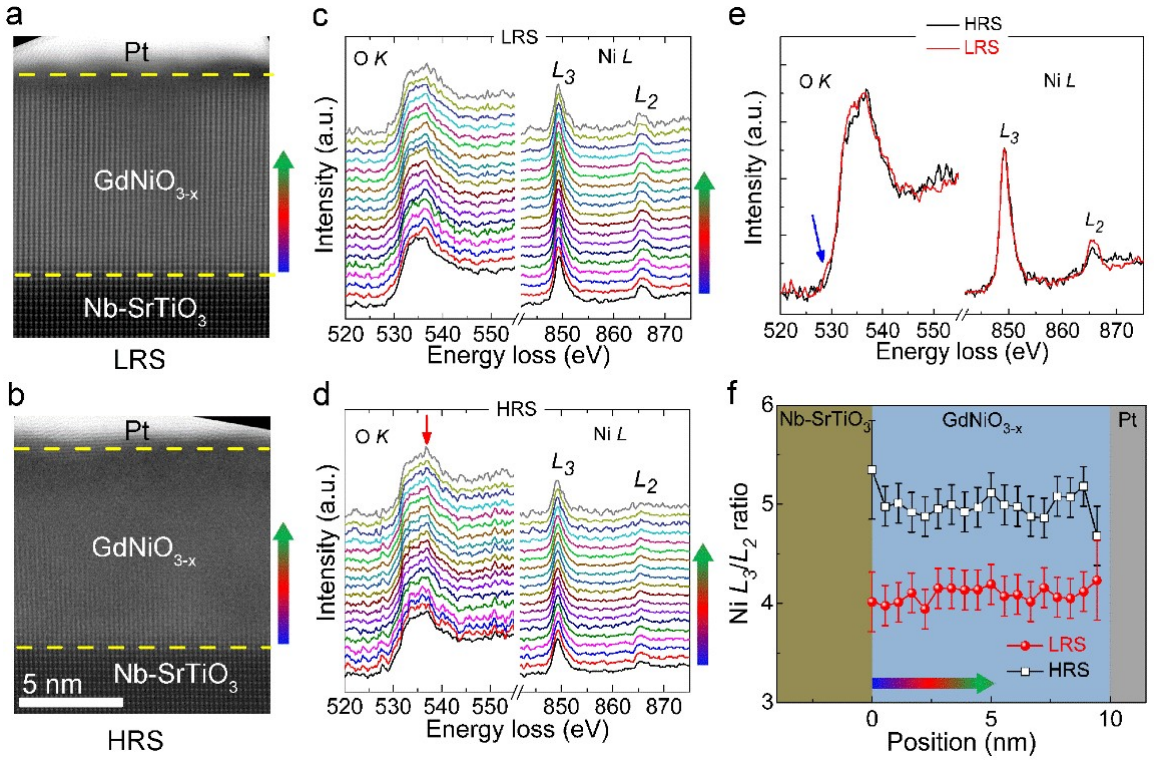

Figure 7.5 HAADF TEM images of Pt/$GdNiO_3$(0.2 mTorr)/Nb-$SrTiO_3$ (D4) at (a) LRS and

(b) HRS. (c, d) O *K* edge and Ni *L* edge EELS spectra along the scanning paths labeled with color arrows in (a) and (b). (e) Comparison between the O *K* edge and Ni *L* edge EELS spectra at HRS and LRS. The pre-peak of O K edge is indicated by a blue arrow. (f) Ni L_3/L_2 area ratio for HRS and LRS after the Ni *L* edge normalization. The error bars are based on the multiple peak area calculations and the line is to assist visualization. The color arrow in the figure indicates the scanning direction.

Since oxygen vacancy induced band engineering exists in all $RNiO_3$ films, the resistive switching behavior should also be universal to $RNiO_3$-based heterojunctions. When the rare-earth element changes from Sm, to Gd, Er, and Lu, the Ni-O-Ni bond angle decreases because the size of rare earth element decreases.[20] Thus, the bandwidth will be reduced, leading to the bandgap opening and higher metal-insulator transition temperature (T_{MI}). The interface barrier of $RNiO_3$/Nb-$SrTiO_3$ junctions may become larger and the resistive switching behavior more obvious. This is indeed confirmed by the results presented in Figure 7.6. Figure 7.6b shows the *I–V* curves of Pt/$RNiO_3$/Nb-$SrTiO_3$ devices. Larger ON/OFF ratios are observed when rare earth changes from Sm to Lu (Figure 7.6b and c). The maximum ON/OFF ratio appears in the $LuNiO_3$-based heterostructure, exceeding 10^6.

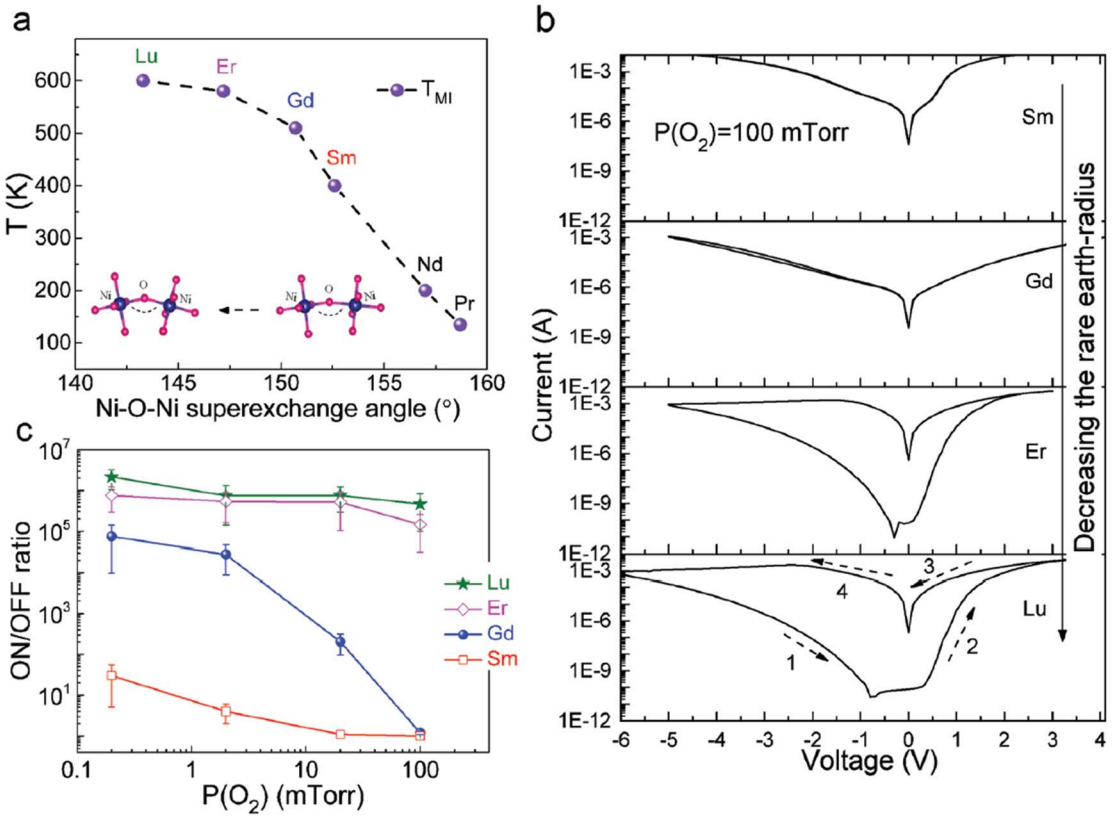

Figure 7.6 (a) T_{MI} as a function of the Ni-O-Ni bond angle. The inset shows the schematic diagram of change bond angles. (b) *I–V* curves of the Pt/$RNiO_3$/Nb-$SrTiO_3$ devices. All $RNiO_3$ films were prepared under 100 mTorr. (c) Dependence of the ON/OFF ratios on $P(O_2)$ and rare earth elements for Pt/$RNiO_3$ /Nb-$SrTiO_3$ heterostructures.

7.3 Conclusions

To summarize, giant resistive switching behavior is observed in nickelates-based heterostructures at room temperature. The relationship between the resistive switching behavior and migration of oxygen vacancies is established and TEM analysis provides direct evidences for the oxygen vacancy migration. Large ON/OFF ratio, good retention and fatigue performance suggest potential applications in non-volatile resistive memory. Overall, this work presented in this chapter provides an important step towards the development of multifunctional electronic devices based on nickelates.

Reference

[1] M. T. Curnan and J. R. Kitchin. *J. Phys. Chem. C* **2014**, 118, 28776-28790.

[2] L. Wang, S. Dash, L. Chang, L. You, Y. Feng, X. He, K. J. Jin, Y. Zhou, H. G. Ong, P. Ren and J. L. Wang. *ACS Appl. Mater. Interfaces* **2016**, 8, 9769-9776.

[3] L. Wang, L. Chang, X. Yin, L. You, J. L. Zhao, H. Guo, K. Jin, K. Ibrahim, J. Wang, and A. Rusydi. *Appl. Phys. Lett.* **2017**, 110, 043504.

[4] S. Wu, H. Peng, and T. Wu. *Appl. Phys. Lett.* **2011**, 98, 093503.

[5] Z. T. Xu, K. J. Jin, L. Gu, Y. L. Jin, C. Ge, C. Wang, H. Z. Guo, H. B. Lu, R. Q. Zhao, and G. Z. Yang. *Small* **2012**, 8, 1279-1284.

[6] Z. Yan and J. M. Liu. *Sci. Rep.* **2013**, 3.

[7] P. Sharma, S. Ryu, J. Burton, T. Paudel, C. Bark, Z. Huang, E. Tsymbal, G. Catalan, C. Eom, and A. Gruverman. *Nano Lett.* **2015**, 15, 3547-3551.

[8] J. J. Yang, I. H. Inoue, T. Mikolajick, and C. S. Hwang. *MRS Bull.* **2012**, 37, 131-137.

[9] H. Peng, G. Li, J. Ye, Z. Wei, Z. Zhang, D. Wang, G. Xing, and T. Wu. *Appl. Phys. Lett.* **2010**, 96, 192113.

[10] K. Zheng, J. Zhao, X. Sun, V. Vinh, K. S. Leck, R. Zhao, Y. Yeo, L. Law, and K. Teo. *Appl. Phys. Lett.* **2012**, 101, 143110.

[11] M. A. Lampert, *Phys. Rev.* **1956**, 103, 1648.

[12] K. C. Kao. *Dielectric phenomena in solids* **2004**, Academic press.

[13] J. Yeargan and H. Taylor. *J. Appl. Phys*. **1968**, 39, 5600-5604.

[14] T. Harada, I. Ohkubo, K. Tsubouchi, H. Kumigashira, T. Ohnishi, M. Lippmaa, Y. Matsumoto, H. Koinuma, and M. Oshima. *Appl. Phys. Lett.* **2008**, 92, 222113.

[15] J. Choi, J.-S. Kim, I. Hwang, S. Hong, S. Jeon, S.-O. Kang, B. Park, D. Kim, M. Lee, and S. Seo. *Appl. Phys. Lett.* **2009**, 95, 022109.

[16] E. Mikheev, B. D. Hoskins, D. B. Strukov, and S. Stemmer. *Nat. Commun.* **2014**, 5.

[17] A. A. Bessonov, M. N. Kirikova, D. I. Petukhov, M. Allen, T. Ryhänen, and M. J. Bailey. *Nat. Mater.* **2015**, 14, 199-204.

[18] J. Gazquez, W. Luo, M. P. Oxley, M. Prange, M. A. Torija, M. Sharma, C. Leighton, S. T. Pantelides, S. J. Pennycook, and M. Varela. *Nano Lett.* **2011**, 11, 973-976.

[19] Z. Wang, J. Yin, and Y. Jiang. *Micron* **2000**, 31, 571-580.

[20] G. Catalan. *Phase Transitions* **2008**, 81, 729-749.

Chapter 8

Conclusions and Future Work

In this chapter, the findings of this study are summarized. Conclusions and propose possible directions are drawn for future study. In a nutshell, the electronic phases of $RNiO_3$ thin films can be reversibly and continuously tuned by controlling oxygen vacancies in them. The band engineered films can be used for solar energy harvesting, photo-detection and non-volatile memory. This study improves our understanding on $RNiO_3$ thin films and open new possibilities for their applications in optoelectronics.

8.1 Conclusions

$RNiO_3$ shows rich electronic phases due to the strong interplay between lattice, orbital and spin.[1-8] Oxygen vacancy is intrinsic and plays an import role in the electronic and magnetic properties of strongly correlated systems.[9-15] In this work, I have studied the effects of oxygen vacancy on the band structure and electrical properties of $RNiO_3$, and explored potential applications of the band engineered $RNiO_3$ thin films in various optoelectronic devices.

First, both post-deposition vacuum annealing and adjusting oxygen pressure during deposition are used to introduce oxygen vacancies into $RNiO_3$ thin films. This is followed by detailed structural and electrical characterizations. Resistance change of as large as $\sim 10^6$ has been observed after introducing oxygen vacancies, and insulating phases with tunable bandgaps are obtained. Detailed XPS and UPS characterizations have been carried out, which reveal that the fraction of Ni^{2+} increases with the amount of oxygen vacancies. The larger Ni^{2+} ion increases the Ni-O bond length and narrows the bandwidth, inducing a bandgap between Ni 3d and O 2p. The process is reversible and continuously tunable.

Secondly, with their tunable bandgaps, it is expected that the oxygen vacancy engineered $RNiO_3$ thin films may find applications in various optoelectronic devices. As a demonstration, $RNiO_3$/Nb-$SrTiO_3$ heterojunctions are thus produced and their performances as photovoltaic cells investigated. By varying the oxygen vacancy content, rare-earth element and device structure, a power conversion efficiency of 1.1% has been achieved. The same heterostructures can also be used as self-powered ultra-sensitive photodetectors. Such photodetectors show high sensitivity toward a broad spectrum of light from 600 to 365 nm. They also show very good long-term stability.

Last but not least, the fact that oxygen vacancies can be introduced into $RNiO_3$ thin films via post-deposition vacuum annealing implies relatively weak Ni-O bonds. It is thus possible to dynamically control the amount and distribution of oxygen vacancies in

$RNiO_3$ thin films using an electric field. This is particularly interesting because oxygen vacancies affect the electronic phase of $RNiO_3$, so the transport property can be dynamically controlled. Indeed, large resistive switching is observed in various $RNiO_3$/Nb-$SrTiO_3$ heterojunctions. Detailed TEM analysis reveals that oxygen vacancy migration indeed occurs and modulates the interface energy barrier, leading to the observed phenomena. Further studies show excellent retention and fatigue performance of these devices and demonstrate their potential as non-volatile memories.

This work improves our understanding on $RNiO_3$ and opens new possibilities for their applications in various optoelectronic devices.

8.2 Future Work

8.2.1 Electrochromic properties of $RNiO_3$

It has been shown in Chapter 7 that the oxygen vacancies in $RNiO_3$/Nb-$SrTiO_3$ heterostructures can migrate under an electric field. The process is schematically shown again in Figure 8.1, and direct evidences are provided by TEM analysis.

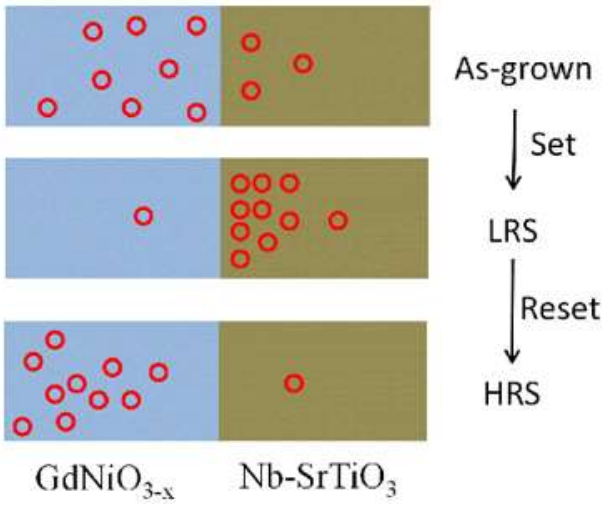

Figure 8.1 Oxygen vacancy migration in $RNiO_3$/Nb-$SrTiO_3$ heterojunctions.

During 'set' process, oxygen vacancies are driven into the substrate by the electric field

while the ‘reset’ process pushes the oxygen vacancies back into $RNiO_3$. Since oxygen vacancies affect the electronic phase of $RNiO_3$, so the ‘set’ process drives the $RNiO_3$ layer to the metallic state while the ‘reset’ process makes it more insulating. Accompanying the phase change with bandgap opened or changed. there should be a drastic change in the transparency of the sample. This is the so-called electrochromic behavior. It has been widely used in applications such as smart glass, smart mirrors and display devices. So, it would be interesting to investigate electrochromic devices based on $RNiO_3$.

8.2.2 Solid oxide fuel cells based on $RNiO_3$

It has been reported that $SmNiO_3$ can work as a solid electrolyte in a proton type solid oxide fuel cell.[16] In its initial state, $SmNiO_3$ shows both high ionic and electronic conductivities. However, electronic conductivity is weakened by spontaneous hydrogen incorporation during the cell operation, where protons localize the free electrons in $SmNiO_3$. On the other hand, the proton conductivity remains so that the potential difference between the anode and cathode can drive the protons across to conduct electricity. The process is schematically shown in Figure 8.2.

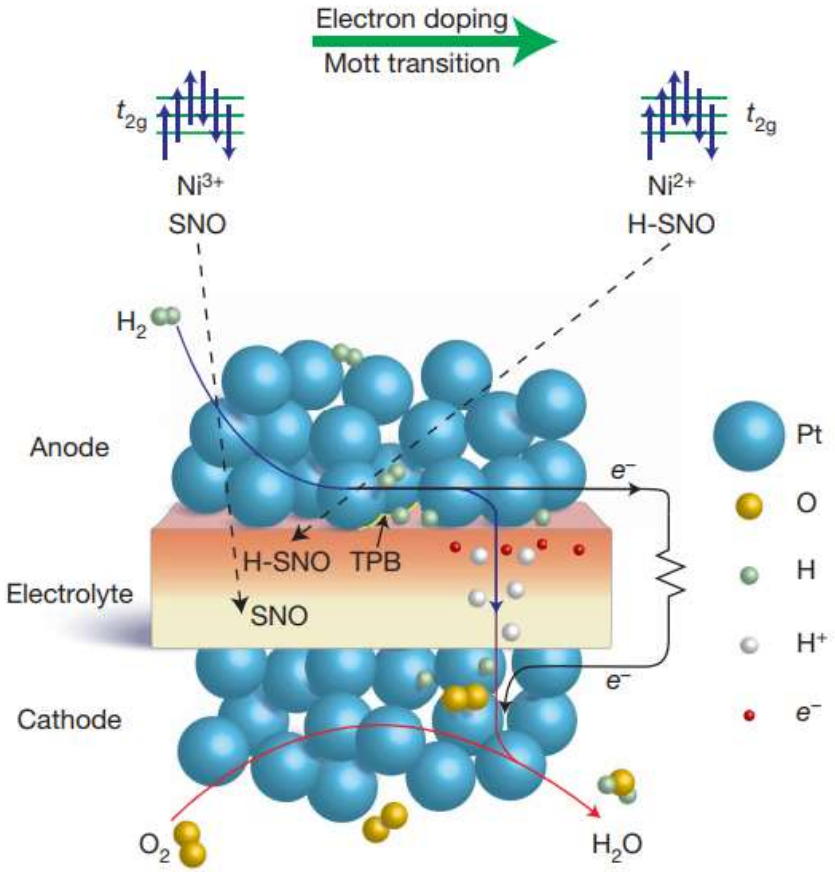

Figure 8.2 Schematic illustration of the operation mechanism of $SmNiO_3$-based solid oxide fuel cells. Reprinted with permission.[16] Copyright 2017, Nature Publishing Group.

However, such a solid oxide fuel cell only works with hydrogen fuel. If the fuel is changed to CH_4 or CO, a different solid electrolyte would be needed which allows oxygen ion transport instead of proton. $RNiO_3$ can still be useful in this case since the migration of oxygen ions has been demonstrated in this work. More importantly, under the operation condition of solid oxide fuel cells, the $RNiO_3$ layer will be insulating and the electronic conductivity will be significantly suppressed. This would be an interesting topic to explore.

Reference

[1] J. Varignon, M. N. Grisolia, J. Íñiguez, A. Barthélémy, and M. Bibes. *npj Quantum Mater.* **2017**, 2, 21.

[2] L. Zhang, X. Chen, H. J. Gardner, M. A. Koten, J. E. Shield, and X. Hong. *Appl. Phys. Lett.* **2015**, 107, 152906.

[3] L. Wang, S. Ju, L. You, Y. Qi, Y.-w. Guo, P. Ren, Y. Zhou, and J. Wang. *Sci. Rep.* **2015**, 5, 18707.

[4] M. Först, A. Caviglia, R. Scherwitzl, R. Mankowsky, P. Zubko, V. Khanna, H. Bromberger, S. Wilkins, Y. D. Chuang, and W. Lee. *Nat. Mater.* **2015**, 14, 883.

[5] J. Shi, Y. Zhou, and S. Ramanathan. *Nat. Commun.* **2014**, 5, 4860.

[6] R. Jaramillo, S. D. Ha, D. Silevitch, and S. Ramanathan. *Nat. Phys.* **2014**, 10, 304.

[7] S. Catalano, M. Gibert, V. Bisogni, O. Peil, F. He, R. Sutarto, M. Viret, P. Zubko, R. Scherwitzl, and A. Georges. *APL Mater.* **2014**, 2, 116110.

[8] P. H. Xiang, N. Zhong, C. G. Duan, X. Tang, Z. Hu, P. Yang, Z. Zhu, and J. Chu. *J. Appl. Phys.* **2013**, 114, 243713.

[9] H. Y. Hwang. *Nat. Mater.* **2005**, 4, 803.

[10] Y. M. Kim, J. He, M. D. Biegalski, H. Ambaye, V. Lauter, H. M. Christen, S. T. Pantelides, S. J. Pennycook, S. V. Kalinin, and A. Y. Borisevich. *Nat Mater.* **2012**, 11, 888.

[11] J. Jeong, N. Aetukuri, T. Graf, T. D. Schladt, M. G. Samant, and S. S. Parkin. *Science* **2013**, 339, 1402-1405.

[12] B. Wang, L. You, P. Ren, X. Yin, Y. Peng, B. Xia, L. Wang, X. Yu, S. M. Poh, and P. Yang. *Nat. Commun.* **2013**, 4, 2778.

[13] Z. T. Xu, K. J. Jin, L. Gu, Y. L. Jin, C. Ge, C. Wang, H. Z. Guo, H. B. Lu, R. Q. Zhao, and G. Z. Yang. *Small* **2012**, 8, 1279-1284.

[14] W. Li, R. Zhao, L. Wang, R. Tang, Y. Zhu, J. H. Lee, H. Cao, T. Cai, H. Guo, and C. Wang. *Sci. Rep.* **2013**, 3, 2618.

[15] R. Zhao, K. Jin, Z. Xu, H. Guo, L. Wang, C. Ge, H. Lu, and G. Yang. *Appl. Phys. Lett.* **2013**, 102, 122402.

[16] Y. Zhou, X. Guan, H. Zhou, K. Ramadoss, S. Adam, H. Liu, S. Lee, J. Shi, M. Tsuchiya, and D. D. Fong. *Nature* **2016**, 534, 231.

Publication List

[1] **L. Chang**, L. You, J. Wang. *Jpn. J. Appl. Phys.* 2018, 57, 0902A3.

[2] **L. Chang**, L. Wang, L. You, Y. Zhou, L. Fang, S. Wang, and J. Wang. *J. Phys. D Appl. Phys.* 2016, 49, 44LT02.

[3] L. Wang[1], **L. Chang**[1], X. Yin, L. You, J. Zhao, H. Guo, K. Jin, K. Ibrahim, J. Wang, A. Rusydi, and J. Wang. *Appl. Phys. Lett.* 2017, 110, 043504.

[4] L. Wang, K. A. Stoerzinger, **L. Chang** J. Zhao, Y. Li, C. Tang, X. Yin, M. E. Bowden, Z. Yang, H. Guo, L. You, R. Guo, J. Wang, K. Ibrahim, J. Chen, A. Rusydi, J. Wang, S. A. Chambers, and Y. Du. *Adv. Funct. Mater.* 2018, 1803712.

[5] L. Wang, Q. Zhang, **L. Chang**, L. You, X. He, K. Jin, L. Gu, H. Guo, Y. Feng, J. Wang, *Adv. Electron. Mater.* 2017, 1700321.

[6] L. Wang, **L. Chang**, X. Yin, A. Rusydi, L. You, Y. Zhou, L. Fang, J. Wang. *J. Phys. Condens*. Matter 2016, 29, 025002.

[7] W. Gao, **L. Chang**, H. Ma, L. You, J. Yin, J. Liu, Z. Liu, J. Wang and G. Yuan. *NPG Asia Mater.* 2015, 7, e189.

[8] L. Wang, H. Ma, **L. Chang**, C. Ma, G. Yuan, J. Wang, T. Wu. *Small* 2016, 13, 1602355.

[9] L. Wang, S. Dash, **L. Chang**, L. You, Y. Feng, X. He, K. Jin, Y. Zhou, H. Guan Ong, P. Ren, S. Wang, L. Chen, and J. Wang. *ACS Appl. Mater. & Interfaces* 2016, 8, 9769-9776.

[10] Y. Zhou, L. You, S. Wang, Z. Ku, H. Fan, Da. Schmidt, A. Rusydi, **L. Chang**, L. Wang, P. Ren, L. Chen, G. Yuan, L. Chen and J. Wang, *Nat. Commun*. 2016, 7, 11193.